UCSF

UC San Francisco Electronic Theses and Dissertations

Title

Pharmacology in the context of pathogenic and non pathogenic bacteria

Permalink

https://escholarship.org/uc/item/6zv91014

Author

Goh Jia Ni, Janice

Publication Date

2023

Peer reviewed|Thesis/dissertation

eScholarship.org Powered by the California Digital Library
University of California

Pharmacology in the context of pathogenic and non pathogenic bacteria

by
Janice Jia Ni Goh

DISSERTATION
Submitted in partial satisfaction of the requirements for degree of
DOCTOR OF PHILOSOPHY

in

Pharmaceutical Sciences and Pharmacogenomics

in the

GRADUATE DIVISION
of the
UNIVERSITY OF CALIFORNIA, SAN FRANCISCO

Approved:

DocuSigned by:
Deanna Kroetz ______________________ Deanna Kroetz
0611A116B51E4AA...
Chair

DocuSigned by:
Leslie Benet ______________________ Leslie Benet
[illegible]457...

DocuSigned by:
Rada Savic ______________________ Rada Savic
7EC091D1336044E...

____

____
Committee Members

Dedication

To God and to my family

Acknowledgments

It takes a village to raise a PhD student. The whole process of this PhD has been full of ups and downs. It was only because of the support of the many people around me that I was able to bend but not break.

First and foremost, to my advisor Professor Rada Savic, thank you so much for giving me a second chance at continuing my PhD when few people believed in me. Despite your busy schedule, you have given me much career advice and encouraged me each step of the way even through hard and uncertain times like when I was hospitalized and depressed. Thank you for encouraging me to try academia again when I had previously given up on it and for giving your support in my job applications.

To my thesis committee chair Professor Deanna Kroetz, thank you for always making time to mentor me and checking in on me throughout my whole PhD even though I wasn’t your student. I am truly thankful to have been guided by you from the first day I started at UCSF till graduation.

To Professor Leslie Benet, thank you for all your insights and advice throughout my PhD. It has been an amazing honor to be able to be advised and learn from one of the giants in the field of Pharmacokinetics.

Much of this work could not have been done without the rest of the amazing Savic lab translational team, both past and present. To Dr Jackie Ernest, Dr Rob C. van Wijk, Dr Qianwen (Chores) Wang, Dr Nan Zhang and Dr Natasha Strydom, thank you for laying the foundation of much of the EBA work, refining it, and guiding me through the project. I appreciate both the technical guidance and friendship offered over the years. To Anu, Dr Annamarie Bustion, Hoang, Connie and Dr Linda Chaba, thank you for being amazing and supportive team members too. Thank you too to Drs Belen Perez Solans, Pieter van Brantegem and Vincent Chang for your advice and support too.

I am grateful too to the many collaborators that have made my project possible. Thank you to Drs Veronique Dartois, Jansy Sarathy, Bree Aldrige and the rest of the TBDA for providing me with critical information for my in vitro to in vivo project.

Thank you too to Professors Elizabeth Johnson, Brian Shoichet, Molly Shoichet and Eric Chan for all your advice on finding a CYP3A4 microbial inhibitor. Thank you to Dr Moriah Sandy for help with analytical chemistry.

To my Turnbaugh lab friends, Drs Than Kyaw, Paola Soto Perez, (soon to be Drs) Lindsey Pieper and Veronica Escalante, thank you for being my go-to support system, for comforting me when I cried and for all our grad student lunches and dinners.

To my academic road biking crew, Dr Cecilia Noecker, Dr Kathy Lam, Dr Benjamin Guthrie, Micah, Alex, Covy and Chloe, thank you for the friendships and all the epic bike rides. I also deeply appreciate all the science discussions and guidance on microbiome work. Dr Cecilia Noecker, thank you for talking through and guiding me through all my wet lab work and microbiome analyses. To Kathy and Alex, thank you for taking care of me when I was hospitalized and for the friendship, food and cats.

Thank you to my PSPG class for all your support and fun times.

Thank you to the Agency for Science, Technology And Research (A*STAR) for funding my PhD. Thank you, Dr Swaine Chen, and Dr Loo Lit Hsin for being my Singaporean scientific mentors. Thank you to Dr Doreen Tan, Ms Koh Seow Ken and Ms Isabelle Teo for giving me the opportunity to practice as a pharmacist in Singapore giving me insight into what actual patient care looks like.

Through my time in San Francisco, I have been very blessed to have an extensive network of people who have supported me even through I came to the city not knowing a single person.

Thank you to Intervarsity GFM Pacific for providing all the spiritual mentorship, events, and fellowship. Thank you to Dr Timothy Tseng for helping me with campus ministry and for talking through problems with me when I was changing thesis labs. Thank you too to Doug Lee for stepping up as the UCSF campus staff to support and help us as a campus ministry. I will always be grateful for the DCM crew too, especially to (soon to be Drs) Nathan Wei, Katie Antilla, Katie Ferrick and Dr Kristel Tjandra for spearheading and leading our weekly DCM complicated but fun discussions.

To my UCSF Christian Fellowship co labourers, Anthony, Christina, Morgan, Ethan, Victoria, Sarah, Kate, Aria, Alex, Marcus, Charis, Elizabeth, and Hannah, thank you for helping to make my campus life so much more fun and letting me learn from the other UCSF schools too.

Thank you to Grand Master Dong Ki Shin and Mrs Shin for not only letting me pursue Taekwondo as my hobby outside of PhD life, but also for taking care of me like a daughter. Thank you too to all my fellow TKD classmates and friends for all your advice and friendship.

Thank you to my Singaporean dinner group too for being my go-to community for food, fun and puns. Thank you to Singapore Connect and the Singapore Global Network for making many of these connections, friendships, and events possible. Thank you to my fellow UCSF Singaporeans for being my other food and support community.

Last but not least, thank you to my family for believing in me and releasing me halfway across the world to pursue a PhD. Thank you for taking the time to call me every week and taking care of Meow. I hope I have done you proud.

All glory to God, through whom we can understand created order and find joy in discovering the beauty that is science.

Contributions

Several chapters in this dissertation have been previously published. In all cases, they have been edited and may not fully represent their published form. Author affiliations can be found in the original publication.

Chapter 1 Translational predictions of phase 2a first-in-patient efficacy studies for antituberculosis drugs is a team effort under review by the European Respiratory journal. Co-first authors by alphabetical order are Jacqueline P. Ernest, Rob Christiaan van Wijk, Natasha Strydom, Nan Zhang, Qianwen Wang, and me. Other authors are Amelia Dietchman and Eric Nuermberger. Rada Savic is the senior corresponding author.

Chapter 2 Novel in vitro TB assays and their utility in predicting drug efficacy and dose is a manuscript in preparation. Other authors include Veronique Dartois and Eric Nuermberger. Rada Savic is the senior corresponding author.

Chapter 3 The human and mouse gut microbiomes modulate host hepatic CYP3A4 enzyme activity is a manuscript in preparation. Other authors include Cecilia Noecker and Ben Guthrie. Peter Turnbaugh is a senior author.

Epigraph

I said to myself, “Look, I have increased in wisdom more than anyone who has ruled over Jerusalem before me; I have experienced much of wisdom and knowledge.” Then I applied myself to the understanding of wisdom, and also of madness and folly, but I learned that this, too, is a chasing after the wind.

For with much wisdom comes much sorrow;
the more knowledge, the more grief…
At the same time…
He has made everything beautiful in its time. He has also set eternity in the human heart; yet no one can fathom what God has done from beginning to end.

Ecclesiastes – (words in italics added by me)

Pharmacology in the context of pathogenic and non-pathogenic bacteria

Janice Jia Ni Goh

Abstract

Since the invention of the microscope and the discovery of microorganisms, mankind has had a huge fascination with microbes – those that live inside us and around us. Despite not being seen by the naked eye, microbes can profoundly affect us in good ways e.g. gut microbes modulating host immunity, bad ways e.g. bacterial infections and curious ways e.g. how the gut microbiome can alter how we process drugs. To tackle such a broad range of issues, this thesis is thus split into two parts. Part 1 will focus on the use of PK-PD models in the context of drug development for infectious airborne microbiome mycobacterium tuberculosis (Mtb). Part 2 takes a different turn into the inside of the human body and will explore how the gut microbiome affects drug disposition.

Part 1: A translational PK-PD toolkit using preclinical in vitro and in vivo data to inform clinical outcomes

Tuberculosis (TB) is once again the leading cause of death among infectious diseases as of 2022. This happens despite known cures, due to the long and complex 6 month regimen with good adherence required for TB treatment. There is thus a pressing need for new drugs and drug treatments that will shorten TB treatment. While multiple new drugs have been developed, and thus many new possibilities for novel drug regimens, drug development is expensive and only a fraction of these drugs and drug regimens can be used for testing. Using a translational PK-PD tool kit, we aim to make use of preclinical in vitro and in vivo data which is much less resource intensive, to predict and prioritize regimens prior to resource-intensive clinical trials.

Part 2: How the microbiome influences drug disposition

Drug clearance is highly dependent on CYP abundance and activity. However, significant interindividual variation in major liver enzyme CYP3A of up to 30- to 40-fold variation exists. Genetic polymorphisms alone cannot account for this variation. Recent evidence suggests the gut microbiome can modulate CYP expression and activity. Here, we aim to elucidate the functional consequences and mechanisms of the gut microbiome's modulation of CYP3A4 activity.

Table of contents

Chapter 1 Translational predictions of phase 2a first-in-patient efficacy studies for antituberculosis drugs........ *1*

Abstract........ 1

Introduction........ 2

Methods........ 4

Results........ 9

Discussion........ 24

Acknowledgments........ 30

References........ 31

Supplemental Methods........ 37

Supplemental Results........ 42

References........ 57

Chapter 2 An in vitro tool kit to predict in vivo monotherapy efficacy for tuberculosis........ *63*

Abstract........ 63

Introduction........ 65

Methods........ 67

Results........ 73

Discussion........ 93

Conclusion........ 95

References........ 96

Supplementary figures........ 97

Chapter 3 The human and mouse gut microbiomes modulate host hepatic CYP3A4 enzyme activity ***101***

Abstract 101

Introduction 102

Materials 106

Methods 113

Results 130

Discussion 160

Caveats 164

Future directions 165

Conclusion 167

References 168

Supplementary materials 177

Contributions 183

Final discussion ***184***

List of Figures

Figure 1.1 The translational pharmacology approach to predicting early bactericidal activity in patients....5

Figure 1.2 A rich dataset of mouse and human PK and PD data for ten first- and second-line TB drugs was compiled for model building. 9

Figure 1.3 Translational (mouse to human) PKPD model predicts clinical EBA trial results well. 21

Figure 1.4 Model-based prediction of daily change in log10 CFU/mL correlates well with clinically observed daily change in log10 CFU/mL for ten TB drugs at multiple dose levels of monotherapy between Day 0 to 2 (top) and Day 2 to 14 (bottom). 23

Figure 2.1 A three step translational platform to find the most predictive in vitro assays for translation into in vivo outcomes in mice....67

Figure 2.2 A total of 33 in vitro assays were compiled for 10 TB drugs 73

Figure 2.3 Feature selection criteria for in vitro assays prior to multivariate and multinomial regression to predict in vivo EC50 77

Figure 2.4 Feature perturbation to find minimum number of features to make reliable predictions 81

Figure 2.5 New TB drugs used as validation with selected in vitro assays could also be predicted with reliable accuracy 86

Figure 2.6 Using predicted in vivo EC50, we could approximate mouse CFU drop over time with drug treatment across different mouse infection models. 89

Figure 2.7 Clinical EBA prediction using in vivo exposure response relationships from in vitro data 91

Figure 3.1 Gut microbial colonization with both mouse and human microbiomes impacts drug metabolism pathways in the liver. 130

Figure 3.2 Gut microbial colonization with both mouse and human microbiomes induce Cyp3a11 expression but does not increase hepatic clearance of the Cyp3a11 substrate midazolam..... 134

Figure 3.3 Mouse cecal and human stool water inhibit CYP3A4 in HepaRG cells at concentrations that are non-toxic to cells. 138

Figure 3.4 The Cyp3a11 inhibitor has colloidal properties and can rapidly cause inhibition in both microsomal and intact cell systems. 142

Figure 3.5 Sphingolipids present in stool water extracts can inhibit CYP3A4 activity in HepaRG cells. 151

Figure 3.6 Gut microbiome modifies microsome membrane fluidity and function.................... 154

Figure 3.7 Unique human stool samples modulate midazolam metabolism in HepaRG cells. . 159

List of Tables

Table 1.1 Parameter estimates of final PK models for ten TB drugs in mouse studies 12

Table 1.2 Parameter estimates of final PKPD models for ten TB drugs in mouse studies 16

Table 2.1 Suggested in vitro assays for in vivo EC50 predictions based on 10 drugs................82

Table 3.1 Reagents used 106

Chapter 1 Translational predictions of phase 2a first-in-patient efficacy studies for antituberculosis drugs

Abstract

Background: Phase 2a trials in tuberculosis typically use early bactericidal activity (EBA), the decline in sputum colony forming units (CFU) over 14 days, as the primary endpoint for testing the efficacy of drugs as monotherapy. However, the cost of phase 2a trials can range from 7 to 19.6 million dollars on average, while more than 30% of drugs fail to progress to phase 3. Better utilizing preclinical data to predict and prioritize the most likely drugs to succeed will thus help accelerate drug development and reduce costs. We aim to predict clinical EBA using preclinical in vivo pharmacokinetic-pharmacodynamic (PKPD) data and a model-based translational pharmacology approach.

Methods and Findings: First, mouse PK, PD and clinical PK models were compiled. Second, mouse PKPD models were built to derive an exposure response relationship. Third, translational prediction of clinical EBA studies was performed using mouse PKPD relationships and informed by clinical PK models and species-specific protein binding**.** Presence or absence of clinical efficacy was accurately predicted from the mouse model. Predicted daily decreases of CFU in the first 2 days of treatment and between day 2 and day 14 were consistent with clinical observations.

Conclusion: This platform provides an innovative solution to inform or even replace phase 2a EBA trials, to bridge the gap between mouse efficacy studies and phase 2b and phase 3 trials, and to substantially accelerate drug development.

Introduction

Mycobacterium tuberculosis remains one of the deadliest infectious agents globally. Tuberculosis (TB) drug discovery and development activity has increased emphasis on shorter, more universal regimens to treat all TB cases independent of resistance status[1]. However, with an increasing number of new drugs and limited resources for clinical trials, further innovation of drug development is imperative to identify effective drugs and regimens more efficiently and with higher confidence[1]. A phase 2a early bactericidal activity (EBA) study is typically the first clinical evaluation of novel anti-TB drug efficacy with the primary purpose of detecting the presence and magnitude of EBA and informing possible dose-response relationships[2]. However, the cost of phase 2a trials can range from 7 to 19.6 million dollars on average, while more than 30% of drugs fail to progress to phase 3[3]. This highlights the challenges inherent in translating results in preclinical models such as in vivo mouse models or in vitro hollow-fiber systems, into successful clinical endpoints and outcomes. FDA guidance for industry on drug development for pulmonary TB states appropriate animal models can serve as an important bridge between the identification of in vitro antimycobacterial effects of an investigational drug and the initiation of clinical trials[4]. However, traditional translation of findings from preclinical *in vivo* models, by pharmacokinetic modeling and allometric scaling to identify the dosing regimen in humans that best matches the efficacious drug exposure in animals, is insufficient as it only covers exposure, but not response. Mechanistic mouse-to-human pharmacokinetic-pharmacodynamic (PKPD) models that describe the bacterial kill and PKPD relationships are better at predicting clinical results, including the results of late-stage trials[5]. Therefore, our objective was to establish a relevant and robust model-based translational platform that can reliably link preclinical to clinical drug development and predict early efficacy trials for anti-TB drugs across different compound classes (Figure 1.1). We compiled a comprehensive preclinical and clinical database of PK, PD, and baseline bacterial growth data for ten drugs. The drugs used to develop and validate our proposed platform consisted of a bacteriostatic antibiotic, namely ethambutol (EMB); five bactericidal antibiotics, namely isoniazid (INH), delamanid (DLM), pretomanid (PMD), linezolid (LZD), and moxifloxacin (MXF); and four sterilizing antibiotics namely rifampin (RIF), rifapentine (RPT), pyrazinamide (PZA), and bedaquiline (BDQ), The translational platform in the present study intends to increase the accuracy of preclinical to clinical translation by enabling quantitative prediction of clinical studies from preclinical outputs and serves as a foundation for model-informed TB drug discovery and development.

Methods

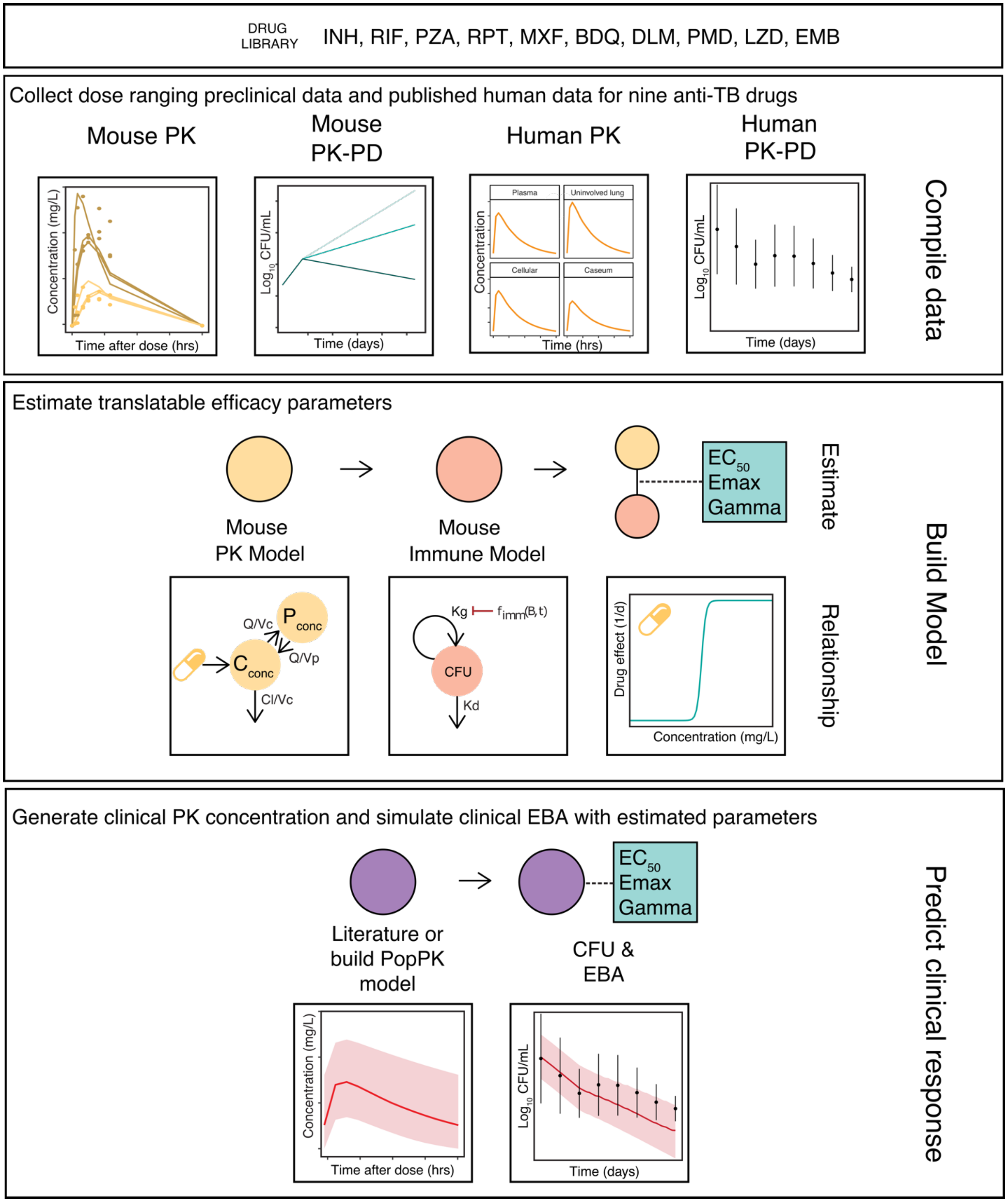
DRUG LIBRARY
INH, RIF, PZA, RPT, MXF, BDQ, DLM, PMD, LZD, EMB
Collect dose ranging preclinical data and published human data for nine anti-TB drugs
Mouse PK
Mouse PK-PD
Human PK
Human PK-PD
Concentration (mg/L)
Time after dose (hrs)
Log_{10} CFU/mL
Time (days)
Plasma
Uninvolved lung
Cellular
Caseum
Concentration
Time (hrs)
Log_{10} CFU/mL
Time (days)
Compile data
Estimate translatable efficacy parameters
Mouse PK Model
Mouse Immune Model
EC_{50}
Emax
Gamma
Estimate
Q/Vc
P_{conc}
C_{conc}
Q/Vp
Cl/Vc
Kg
$f_{imm}(B,t)$
CFU
Kd
Drug effect (1/d)
Concentration (mg/L)
Relationship
Build Model
Generate clinical PK concentration and simulate clinical EBA with estimated parameters
Literature or build PopPK model
EC_{50}
Emax
Gamma
CFU & EBA
Concentration (mg/L)
Time after dose (hrs)
Log_{10} CFU/mL
Time (days)
Predict clinical response

Figure 1.1 The translational pharmacology approach to predicting early bactericidal activity in patients.

Components necessary for translation include mouse PKPD and clinical PK (actual or scaled). The estimated relationship between drug concentration and bacterial kill is assumed to be portable after correction for protein binding and integrated with clinical PK. Using baseline bacterial burden from previous EBA trials as initial conditions, the early bactericidal activity is simulated with the translational model.

Drug dataset for model building and validation

To build our model and evaluate its predictive accuracy for clinical EBA, ten first- and second-line anti-TB drugs (BDQ, DLM, EMB, INH, LZD, MXF, PMD, PZA, RIF, RPT) were selected for which mouse PK, mouse PD, human population PK models and human clinical EBA data were available.

Data required to assess preclinical drug efficacy

A large database of PK and PD data in mice for 10 TB drugs with clinical EBA data was collected (Figure 1.2, Table S1.1). Most experiments were performed at Johns Hopkins University (JHU), with the exception of DLM for which PK data came both from JHU as well as from literature for one dose level[6], EMB for which PK data came from literature[7], and LZD that had data from the Tuberculosis Alliance (TBA). PK experiments in BALB/c mice were dose-ranging (2-10 dose levels), single or multiple oral dosing for up to 8 weeks, with 29-238 observations of plasma concentration per drug. PD experiments in BALB/c mice infected through aerosol delivery were dose-ranging (2-15 dose levels) with treatment durations of 21-70 days, and 55-252 observations of lung CFU counts per drug. Lung CFU counts were measured by plating lung homogenates at designated time points. In the case where DLM mouse PK data showed the unexpected trend of a double peak with a single oral dose (Figure 2a), we confirmed the trend with the data provider, JHU.

Mouse PKPD model development

An integrated mouse PKPD model involving a PK model to describe drug exposure, a bacterial dynamics model to account for the mouse immune system and a PD model describing the combined effect of bacterial dynamics and drug effect was developed for each drug. PK data were described using one- or two-compartment models with first order absorption with or without delay, and saturable elimination when necessary. The bacterial growth dynamics without treatment was described using our previously published baseline model (Eq. S1)[8]. The baseline model captures the decreased rate of growth over time and attributes the decline to time- and bacteria-dependent immune control over the infection. The drug effect, measured as the $\log_{10}$ CFU drop independent of the immune effect over time, was incorporated using a sigmoidal Emax relationship (Eq. S2). A delay effect (K_{delay}) was included to mouse PKPD models to establish an indirect relationship between plasma drug concentrations and drug effect at the site of action (Eq. S3 & S4). Detailed model development and model diagnostics can be found in the Supplemental materials.

Prediction of the clinical EBA

The PKPD relationship quantified in mice was used to predict the clinical EBA. Drug concentrations in humans were simulated based on clinical population pharmacokinetic models (Table S1.1) to drive the concentration-effect relationship in the clinical predictions. Where clinical population PK models were unavailable, allometric scaling from mouse PK was used[9]. Protein binding ratios between humans and mice ($f_{u\frac{humans}{mice}}$) were used to convert unbound plasma drug concentrations from human to mouse to translate the mouse PKPD relationships (Table S1.1)[10–16].

Clinical predictions for 10 drugs were simulated, with 14 unique studies at several dose levels were used for validation by graphically overlaying simulated EBA from preclinical models with observed EBA from clinical trials. Predictions were done by simulating CFU decline in 1000 virtual patients treated with the same dose as reported in the clinical EBA study. The baseline (Day 0) sputum values used were derived from the mean value for each arm reported in each study, and the variability in baseline bacterial burden between individuals used was the baseline variance among all clinical studies. The net growth and death of bacteria without treatment was assumed to be zero (Eq. S5). Predictions were reported as the mean and standard deviation of the predicted time course of CFU decline. For drugs where observed data were available, the data were overlayed for visual inspection. Finally, quantitative predictions of commonly reported parameters (change from baseline to Day 2 and from Day 2 to Day 14) were compared to the observed at various dose levels along a line of unity.

Software and statistical method

Preclinical and clinical PKPD modelling was performed in NONMEM (7.4.3) through Perl Speaks NONMEM (PsN) (4.8.1.). For LZD preclinical PK, Monolix (5.0.0) was used. Models were developed following numerical and graphical diagnostics, assessing drop in objective function value through the likelihood ratio test and parameter precision, as well as goodness-of-fit plots and visual predictive checks, respectively, in addition to pharmacological relevance. Data transformation and graphical output were performed in R (4.1.3) through the RStudio (2022.02.3) interface using the xpose4 and tidyverse packages.

Results

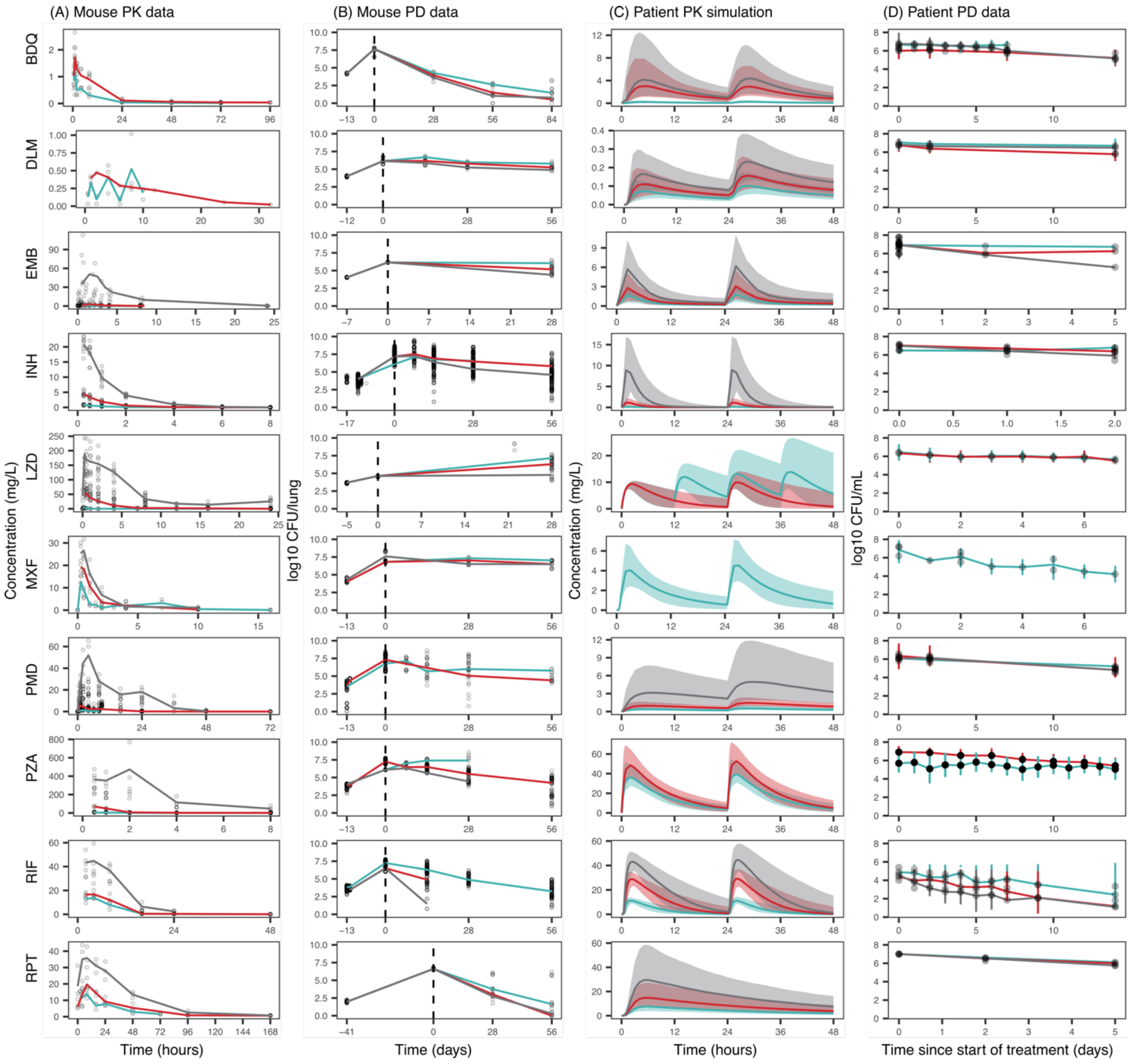

Figure 1.2 A rich dataset of mouse and human PK and PD data for ten first- and second-line TB drugs was compiled for model building.

Only minimum, median and maximum doses are represented as median lines when multiple doses were studied. Data points for all doses are plotted. Information on all doses is present in Table 1.

(A) Mouse pharmacokinetic (PK) data presented for the following doses: BDQ 12.5, 25 mg/kg; DLM 2.5, 3 mg/kg; EMB 10, 30, 1000 mg/kg; INH 1.56, 6.25, 25 mg/kg; LZD 5, 100, 500 mg/kg; MXF 100, 200, 400 mg/kg, PMD 6, 28.8, 486 mg/kg; PZA 7, 100, 900 mg/kg; RIF 10, 15, 40 mg/kg; RPT 5, 10, 20 mg/kg. All doses were given once daily unless otherwise stated.

(B) Mouse pharmacodynamic (PD) data presented for the following doses: BDQ 12.5, 25, 50 mg/kg; DLM 3, 10, 100 mg/kg; EMB 100, 400, 1600 mg/kg; INH 0.1, 6.25, 100 mg/kg; LZD 100, 300, 1000 mg/kg; MXF 25, 50, 100 mg/kg; PMD 6.25, 30, 600 mg/kg; PZA 3, 50, 900 mg/kg; RIF 2.5, 40, 640 mg/kg; RPT 5, 10, 20 mg/kg. All doses were given once daily, 5 days a week, unless otherwise stated.

(C) Human PK simulations from validated population PK models presented for the following doses: BDQ 25, 200, 400 mg; DLM 100, 200, 400 mg; EMB 15, 25, 50 mg/kg; INH 9, 75, 600 mg; LZD 600 mg once daily, 600 mg twice daily; MXF 400 mg; PMD 50, 200, 1200 mg; PZA 2000 mg; RIF 600, 1350, 1950 mg; RPT 300, 600, 1200 mg. All doses were given once daily, unless otherwise stated.

(D) Human Phase 2a early bactericidal activity study data presented for the following doses: BDQ 25, 200, 400 mg; DLM 100, 200, 400 mg; EMB 15, 25, 50 mg/kg; INH 9, 75, 600 mg; LZD 600 mg once daily, 600 mg twice daily; MXF 400 mg; PMD 50, 200, 1200 mg; PZA 200 mg; RIF 600, 1350, 1950 mg; RPT 300, 600, 900, 1200 mg. All doses were given once daily, unless otherwise stated.

Large preclinical and clinical PK and PD database of ten TB drugs

We collated a rich longitudinal dataset of mouse PK (plasma concentrations, 1220 data points) and PD data (lung CFU counts, 1550 data points), as well as human population PK models and human PD data (sputum CFU counts) (Table S1). PD experiments were done mostly in mouse infection models infected via aerosol with an inoculum size no less than 3.5 $\log_{10}$ CFU/ml and incubation periods of 13-17 days, prior to the start of treatment. Exceptions were EMB and LZD, which had incubation periods of 7 and 5 days, respectively, but had a similar inoculation size of larger than 3.5 $\log_{10}$ CFU/ml, and RPT which had an incubation period of 41 days but a lower inoculation size than 3.5 $\log_{10}$ CFU/ml.

Human PK data were simulated using published models from literature (Table S1.1 and Figure 1.2C). Human PD data with a total of 287 human sputum CFU datapoints originating from Phase 2a trials across 14 different studies ranging from 2 to 14 days were used to validate our Phase 2a EBA predictions.

Table 1.1 Parameter estimates of final PK models for ten TB drugs in mouse studies

Complete equations for PK models are found in equations S6-12. 1 compartment model indicates that distribution and elimination phases of the drug were almost instantaneous and can be described by a single central compartment. 2 compartment model indicates that distribution and elimination phases of the drug were distinct and can be described by a central compartment and a peripheral compartment.

Linear elimination indicates that elimination pathways were not saturated with higher doses for the tested dose range. Saturated elimination indicates elimination plateaus after a certain dose. This relationship can be described by a Michaelis Menten equation using K_m and $V_{max.}$

Ka = rate of absorption, CL = linear clearance, V_c = central compartment volume, V_p = peripheral compartment volume, Q = flow between central and peripheral compartments, K_m = concentration that produces half the maximum rate of elimination, V_{max} = maximum rate of elimination. F1 = relative bioavailability of drug to lowest dose, CL_{int} = intrinsic clearance describing saturated elimination, F= the extent of drug absorbed from oral dosing compartment into systemic compartment, F_{DIF}= the maximum difference in bioavailability from 100% (bound between 0% and 100%), FD_{50}= the dose achieving half maximal reduction in bioavailability, A_{LAG} = absorption lag time.

Drug	**Structural PK model**	**PK parameters (RSE)**	**Protein binding ratio (f_u, human/mouse)**
BDQ	2 compartment, linear elimination	K_a = 3.24 h^{-1} (15.1%) CL = 0.0243 L/h (5.9%) V_c = 0.24 L (11.4%) V_p = 0.822 L (29.3%) Q = 0.0127 L/h (11.5%)	1.0 [17]
DLM	1 compartment, linear elimination	K_a=0.446 h^{-1} (25%) CL = 0.0092 L/h (8%) V_c=0.0747 L (1%) $F_{3mg/kg}$=0.758 (5%)	1.0 [18]

Drug	Structural PK model	PK parameters (RSE)	Protein binding ratio (f_u, human/mouse)
EMB[7]	2 compartment. linear elimination	CL = 0.0512 L/h (5.9%) V_c = 0.0436 L (12.8%) V_p = 0.0982 L (7.6%) K_a = 0.869 h^{-1} (9.9%) Q = 0.0352 L/h (13.5%) F = 0.64 (6.7%) A_{LAG} = 0.0577 h (11.1)	1.0
INH	2 compartment, saturated elimination	CL_{INT}=31.5 mL/hr (8.1%) K_m =13.1 ug/mL (23.2%) K_a=7.89 1/hr (89.4%) V_c=18.6 mL (45.0%) Q =13.3 mL/hr (97.7%) 3 V_p =9.77 mL (66.4%)	1.455 [19,20]
LZD	2 compartment, saturated elimination	ka = 10 h^{-1}FIX CL_{INT}=0.0526 L/h V_c = 0.0178 L V_p =0.00836 L Q = 0.00175 L/h K_m = 8.03 mg/L	0.986 [13,21]

Drug	**Structural PK model**	**PK parameters (RSE)**	**Protein binding ratio (f_u, human/mouse)**
MXF	2 compartment, linear elimination	Ka=0.0723 h^{-1} (10%) Q=0.1269 L/h (20%) V_c = 0.09423 L (7%) V_p = 0.3504 L (25%) CL=0.119 L/h (12 %)	0.797 [22]
PMD	2 compartment, saturated elimination and bioavailability	ka = 2.94 h^{-1} (31%) CL_{INT}=0.0392 L/h (9%) V_c = 0.158 L (7%) V_p =0.00568 L (71%) Q = 0.00009 L/h (18%) K_m = 2.74 mg/L (24%) F_{DIF}=1 FIX FD50=363 mg/kg ***Y***=1 FIX	0.71 [19,23]

Drug	Structural PK model	PK parameters (RSE)	Protein binding ratio (f_u, human/mouse)
PZA	2 compartment, saturated elimination and bioavailability	CL_{INT}=14.4 ug/hr (12%) K_m=82.9 ug/mL (61%) K_a = 100 1/hr FIX Vc=13.3 mL (49%) Q=3.11 mL/hr (19%) Vp =10.9 mL (37%) $F1_{7\ mg/kg}$ = 1 FIX FD_{50} = 18.2 mg*kg^{-1} (23%) F_{DIF} = 0.574 (34%)	0.925 [24]
RIF	2 compartment, saturated elimination and bioavailability	V_{max}=15.2 ug/hr (6%) K_m=1.16 ug/mL (20%) K_a=0.272 1/hr (10%) V_1=3.39 mL (12%) Q=0.725 mL/hr (6%) V_2=27.4 mL (39%) $F1_{10\ mg/kg}$=1 FIX $F1_{15\ mg/kg}$=0.743 (0%) $F1_{20\ mg/kg}$=0.845 (1%) $F1_{40\ mg/kg}$ =0.493 (2%)	4.545 [20,25]

Drug	**Structural PK model**	**PK parameters (RSE)**	**Protein binding ratio (f_u, human/mouse)**
RPT	1 compartment, saturated elimination	ka = 0.894 h^{-1} (31%) V = 0.0139 L (6%) K_m = 75.8 ug/mL (31%) V_{max} = 0.0333 ug/hr (24%)	0.422 [26,27]

Table 1.2 Parameter estimates of final PKPD models for ten TB drugs in mouse studies

K_{delay}= the delay rate of the plasma concentration associated with drug effect, Emax= the maximal level of drug effect, EC50= the delayed concentration that results in half of the maximal drug effect, ***Y***= the steepness of the relationship between the delayed plasma concentration and drug effect. Equations are in equations S3-4.

Drug	**PK/PD Model**	**PK/PD Model Parameters**	**Mouse infection model Type**
BDQ	Direct Emax Function	Emax = 0.515 day^{-1} (1%) EC_{50} = 0.228 mg/L (5%)	Subacute
DLM	Delayed Emax Function	Emax = 0.248 day^{-1}(23%) EC_{50} = 1.02 mg/L (63%) K_{delay} = 91.4 day^{-1} (0.2%)	Subacute
EMB	Direct Emax Function	Emax = 0.527 day^{-1} (2%) EC_{50} = 0.150 mg/L (17%)	Acute
INH	Delayed Emax Function	Emax = 0.901 day^{-1} (7.5%) EC_{50} = 0.00404 mg/L (55%) K_{delay} = 7.51 day^{-1} (20%)	Subacute
LZD	Delayed Sigmoidal Function	Emax = 1 day^{-1} (FIX) EC_{50} = 2.77 mg/L (1%) ***Y*** = 0.21 (3%) K_{delay} = 6.75 day^{-1} (0%)	Acute
MXF	Delayed Emax Function	Emax = 0.553 day^{-1} (10%) EC_{50} = 0.0000586 mg/L (44%) = 0.0000708 day^{-1} (0.07%)	Subacute

Drug	**PK/PD Model**	**PK/PD Model Parameters**	**Mouse infection model Type**
PMD	Direct Sigmoidal Function	Emax = 0.429 day^{-1} (0.1%) EC_{50} = 3.46 mg/L (0.3%) ***Y*** = 0.375 (1%)	Subacute
PZA	Delayed Emax Function	Emax = 0.34 day^{-1} (10%) EC_{50} (AUC)= 13.6 mg*day/L (42%) K_{delay} = 0.797 day^{-1} (0.2%)	Subacute
RIF	Delayed Sigmoidal Function	Emax = 0.678 day^{-1} (16%) EC_{50} = 1.92 mg/L (39%) ***Y*** = 1.38 (24%) K_{delay} = 1.34 day^{-1} (79%)	Subacute
RPT	Direct Sigmoidal Function	Emax = 0.299 day^{-1} (1%) EC_{50} = 6.02 mg/L (0%) ***Y*** = 2.36 (7%)	Chronic

Preclinical PK and PKPD models adequately described mouse data

The final PK and PKPD model parameter estimates are shown in Table 1.1. A 2-compartment model with saturated clearance described via the Michaelis Menten equation best described the mouse plasma concentration data for INH, LZD, PMD, PZA and RIF. BDQ, EMB, and MXF were best described using 2-compartment models with linear elimination, RPT by a 1-compartment model with saturated elimination, and DLM by a 1-compartment model with linear elimination. Visual predictive checks of the final model for both mouse PK and PKPD data showed good fits (Figures S1.1 & S1.2). The exposure-response relationships for each drug in mouse infection models are summarized in Table 1 and Figure S3 and aligned with clinical knowledge of the efficacy of each drug.

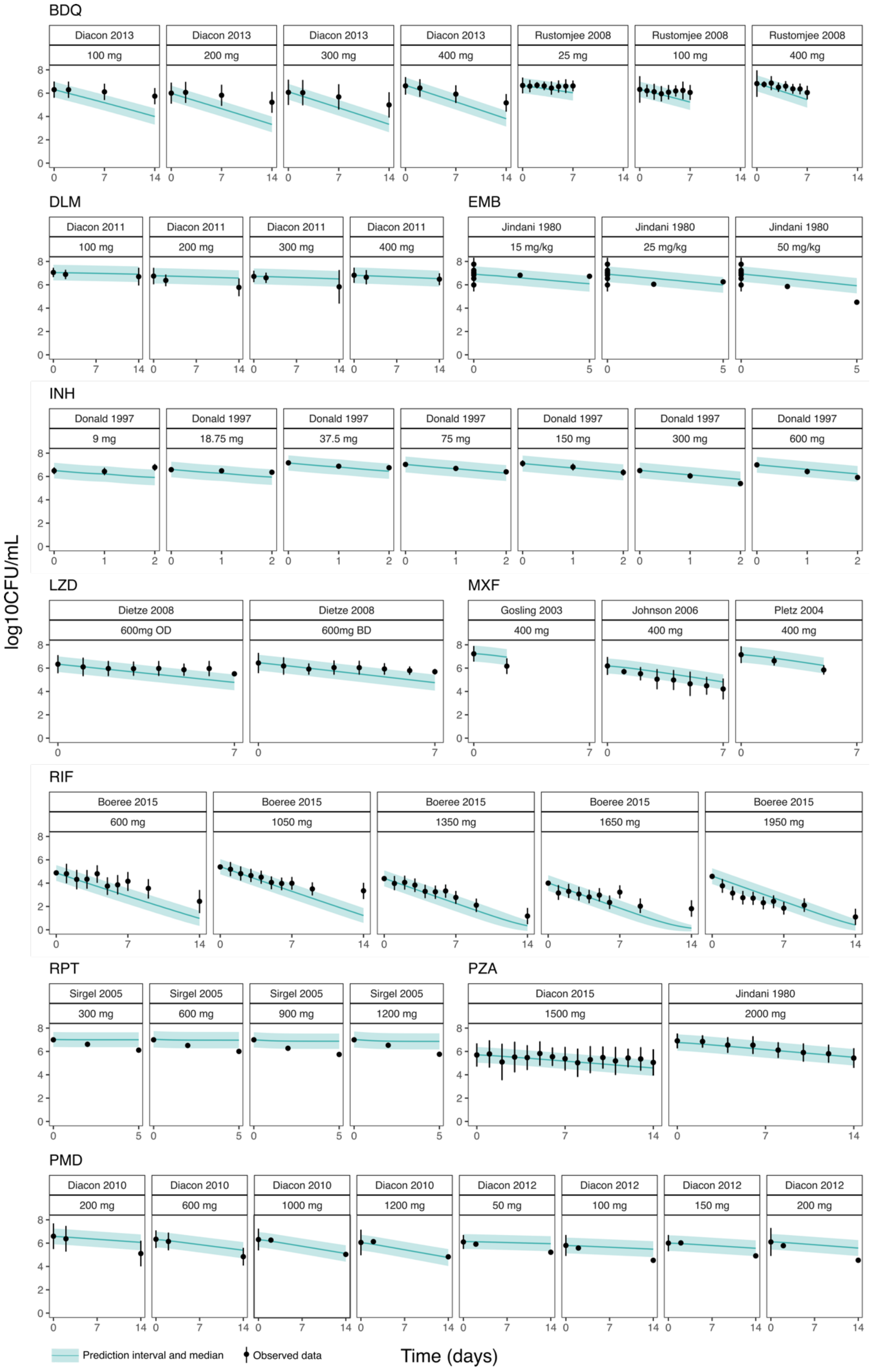
BDQ
Diacon 2013 100 mg
Diacon 2013 200 mg
Diacon 2013 300 mg
Diacon 2013 400 mg
Rustomjee 2008 25 mg
Rustomjee 2008 100 mg
Rustomjee 2008 400 mg
DLM
Diacon 2011 100 mg
Diacon 2011 200 mg
Diacon 2011 300 mg
Diacon 2011 400 mg
EMB
Jindani 1980 15 mg/kg
Jindani 1980 25 mg/kg
Jindani 1980 50 mg/kg
INH
Donald 1997 9 mg
Donald 1997 18.75 mg
Donald 1997 37.5 mg
Donald 1997 75 mg
Donald 1997 150 mg
Donald 1997 300 mg
Donald 1997 600 mg
LZD
Dietze 2008 600mg OD
Dietze 2008 600mg BD
MXF
Gosling 2003 400 mg
Johnson 2006 400 mg
Pletz 2004 400 mg
RIF
Boeree 2015 600 mg
Boeree 2015 1050 mg
Boeree 2015 1350 mg
Boeree 2015 1650 mg
Boeree 2015 1950 mg
RPT
Sirgel 2005 300 mg
Sirgel 2005 600 mg
Sirgel 2005 900 mg
Sirgel 2005 1200 mg
PZA
Diacon 2015 1500 mg
Jindani 1980 2000 mg
PMD
Diacon 2010 200 mg
Diacon 2010 600 mg
Diacon 2010 1000 mg
Diacon 2010 1200 mg
Diacon 2012 50 mg
Diacon 2012 100 mg
Diacon 2012 150 mg
Diacon 2012 200 mg
log10CFU/mL
0
2
4
6
8
0
1
2
5
7
14
Prediction interval and median
Observed data
Time (days)

Figure 1.3 Translational (mouse to human) PKPD model predicts clinical EBA trial results well.

Medians and 95% confidence intervals of 1000 simulations from the translational model overlap with observed EBA data from clinical trials[2,25,28–38].

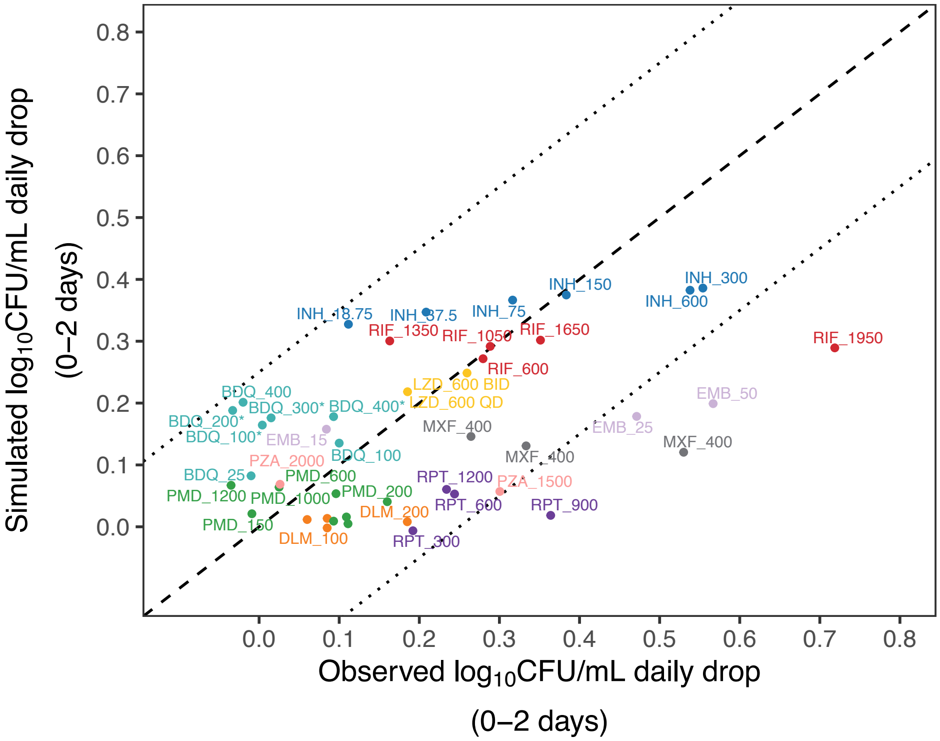
Simulated $\log_{10}$CFU/mL daily drop
(0–2 days)
0.8
0.7
0.6
0.5
0.4
0.3
0.2
0.1
0.0
INH_18.75
INH_37.5
INH_75
INH_150
INH_300
INH_600
RIF_1350
RIF_1050
RIF_1650
RIF_600
RIF_1950
LZD_600 BID
LZD_600 QD
BDQ_400
BDQ_300*
BDQ_400*
BDQ_200*
BDQ_100*
EMB_15
EMB_25
EMB_50
MXF_400
MXF_400
MXF_400
BDQ_100
PZA_2000
PZA_1500
BDQ_25
PMD_600
PMD_1200
PMD_1000
PMD_200
PMD_150
DLM_200
DLM_100
RPT_1200
RPT_600
RPT_900
RPT_300
0.0
0.1
0.2
0.3
0.4
0.5
0.6
0.7
0.8
Observed $\log_{10}$CFU/mL daily drop
(0–2 days)

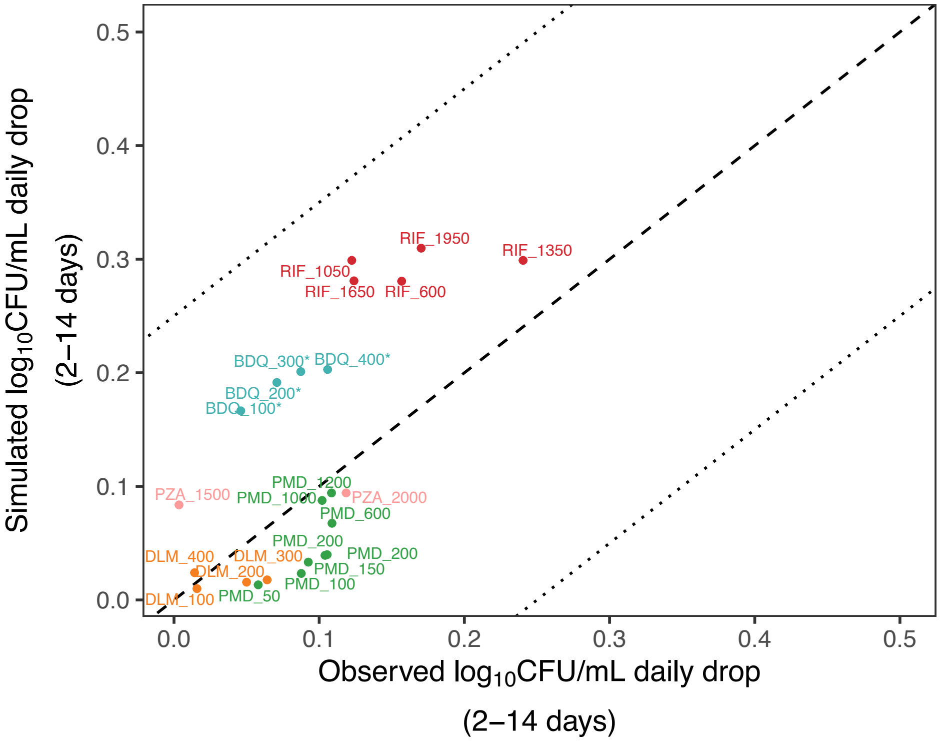
Simulated $\log_{10}$CFU/mL daily drop
(2–14 days)
0.5
0.4
0.3
0.2
0.1
0.0
RIF_1950
RIF_1350
RIF_1050
RIF_1650
RIF_600
BDQ_300*
BDQ_400*
BDQ_200*
BDQ_100*
PZA_1500
PMD_1200
PMD_1000
PZA_2000
PMD_600
PMD_200
DLM_400
DLM_300
PMD_200
DLM_200
PMD_150
PMD_100
DLM_100
PMD_50
0.0
0.1
0.2
0.3
0.4
0.5
Observed $\log_{10}$CFU/mL daily drop
(2–14 days)

Figure 1.4 Model-based prediction of daily change in log10 CFU/mL correlates well with clinically observed daily change in log10 CFU/mL for ten TB drugs at multiple dose levels of monotherapy between Day 0 to 2 (top) and Day 2 to 14 (bottom).

For some drugs, Day 14 data were not available. Line of unity (dashed line) ± 0.25 (dotted lines). BDQ = bedaquiline, DLM = delamanid, EMB = ethambutol, INH = isoniazid, LZD = linezolid, MXF = moxifloxacin, PMD = pretomanid, PZA = pyrazinamide, RIF = rifampin, RPT = rifapentine. *regimen contained a loading dose

Clinical EBA was well predicted by the translational platform

The translational platform predicted clinical EBA in TB patients receiving monotherapy with the ten drugs as shown in Figure 1.3. Our predictions overlapped well with the observed data across multiple doses and time points for most of the drugs. BDQ and LZD had slight over predictions at the later time, and RPT showed activity up to 5 days after a single dose, whereas our model predicted limited declines in CFU.

Agreement between predicted and observed quantitative change in CFU is shown in Figure 1.4 as a correlation plot for EBA at time intervals of 0-2 days and 2-14 days. Most predictions for 0-2 days fell within 0.25 $\log_{10}$ CFU/ml/day of the observed EBA as indicated by the line of unity and corresponding dotted lines. Predictions for 2-14 days were even closer to observed. Predictions were overall consistent with the observed data in the clinical EBA studies for all ten drugs, except for RPT where activity was underpredicted.

Discussion

We established a mouse-to-human translational platform by integrating a bacterial dynamics model, mouse PKPD relationships, clinical PK and species-specific drug plasma protein binding and validated the platform with clinical EBA data (Figure 1). The changes in sputum CFU counts over the first two days and from Day 2 to Day 14 in TB patients receiving monotherapy with each of ten TB drugs in 14 clinical EBA studies spanning more than four decades were successfully predicted (Figure 3 and 4). Compared to the participants enrolled in more recent EBA studies (2007 to 2015)[28–30,32,36,37,39] at the same site, the participants enrolled between 1992 and 2005[31,33–35,38] had more severe disease and therefore higher baseline CFU counts in their sputum samples (mean baseline: 6.9 $\log_{10}$ CFU per mL). However, the predictive accuracy of our model was robust despite this large variation in baseline bacterial burden. For example, RIF had a good overlap of predicted and observed EBA (Figure 3) despite the study being conducted in 2015 with the lowest median baseline of 4.58 $\log_{10}$ CFU per mL[26,28,29].

A key component to our model accuracy was the addition of the bacterial dynamics model. Mouse and human immune activation against TB infection differ significantly, therefore the underlying baseline of bacterial dynamics will differ. Subtracting the mouse immune effect on bacterial decline more accurately estimates the drug contribution to CFU decline. Without such consideration, the clinical CFU decline was overpredicted (Figure S4). Despite inherent differences between species in terms of drug PK, sampling (whole lung homogenate versus sputum), and infecting bacterial strain, the relationship between drug effect on bacteria and the concentration to achieve the effect appear, based on this analysis, to be portable between mice and patients. In addition, although the mouse strain used in the studies (BALB/c) models intracellular bacteria but not extracellular bacteria in caseous lesions[28,30,31], the PKPD relationships observed in this model, when derived in comparison to the baseline bacterial dynamics, appear to accurately reflect those observed in EBA studies. Other approaches or more information may be needed to fully account for drug exposures at the site of infection in cavities or other caseous lesions or any PK/PD relationships unique to those microenvironments.

Murine TB models are routinely and often exclusively used as *in vivo* efficacy models in preclinical TB drug development[39,41,42]. As the inoculum size and incubation period for bacterial infection in the lung prior to treatment can affect drug response[43], we standardized our inclusion criteria to experiments using the most common design with the incubation duration of 13-17 days and inoculum size to larger than 3.5 $\log_{10}$ CFU/ml. Incubation durations outside this range were considered only when data were otherwise not available, which was the case for EMB, LZD and RPT.

Clinical EBA studies are the only acceptable way to evaluate a drug as monotherapy in TB patients despite their limitations on predicting long-term efficacy. In addition to detecting the presence of an EBA response, the trial can inform on the dose-response curve (e.g., INH and RIF), which could be used in dose selection for future trials[44]. We have shown here that our translational platform can adequately predict these EBAs for different doses. With limited resources, this costly clinical study can be designed more efficiently or avoided altogether by using our approach to predict a reliable result regarding clinical dose-response effects, and to provide useful information about dose and/or drug candidate selection for further clinical development. This scenario is well exemplified by the nitroimidazole, PMD. PMD has a dose response at doses up to 192 mg/kg in mice which, following the conventional allometric scaling method, approximates 1500 mg in humans. However, such translation is problematic as the clinical observations from two human EBA trials demonstrated no dose response above 200 mg in human EBA. Using our translational platform, we found that the drug effect of PMD reaches plateau after 200 mg which is consistent with clinical observations (Figure S3). Therefore, our translational platform could serve as a powerful tool for, but not limited to, better dose selection for clinical trials design. By better informing dose selection, the translational modeling platform may reduce the time and effort spent in early clinical development, and therefore, accelerate progress to trials that are more informative of long-term outcomes.

Phase 2a trials also gather information on initial safety and tolerability of compounds of interest that our translational framework is not designed to predict. However, when anti-TB drug development progresses directly to regimen efficacy studies, these safety data can already be captured during Phase 1 healthy volunteer monotherapy studies, especially the multiple ascending dose (MAD) study which is a dose ranging study for up to 4 weeks. The trial population of healthy volunteers is different from the patient population, but safety signals are more pronounced in this healthy population that is more sensitive to adverse events and less burdened by other symptoms. Treatment of healthy volunteers with rifapentine for example resulted in safety signals, but has been proven safe in patients with tuberculosis[45]. Furthermore, we can also get guidance on the optimal efficacious dose versus the safety range using the dose response curve by overlaying both exposures (Figure S3). All our studied drugs have been previously approved and are used clinically. Having all clinical dose exposures lower than safety limits was thus unsurprising and reassuring. Such dose response curves as visualization would also be helpful for determining the dose of new TB drugs as it provides a measure of both efficacy and safety.

Of the clinical EBA studies included in our analysis, the RPT EBA trial was the only one in which EBA was assessed for multiple days after a single dose. Our human population PK model indicated RPT was mostly cleared from the body two days after a single dose, but the trial results indicated RPT was still exerting an effect on bacterial load between two and five days post-dose. It is possible that RPT has a post-antibiotic effect that was not sufficiently captured by the model.

The model overpredicted the EBA of BDQ. However, in the model, the active metabolite, BDQ-M2, was not considered. In mice, M2 is estimated to contribute approximately 50 percent of the drug effect. One possible reason for the overprediction are the parent-to-metabolite ratios between species that differ, where mice have higher M2-to-BDQ ratios than humans[46,47]. Future studies can account for these differences.

Our translational framework has been developed to predict clinical EBA in the typical adult patient population participating in EBA trials. Heterogeneity in the patient population is an important consideration in drug development and individualized medicine[48]. This is both from the perspective of representing patients in easy- or hard-to-treat phenotypes as we have observed in our clinical projects as a result from different risk factors (baseline bacterial burden, disease phenotype such as cavitation, gender, comorbidities or comedications), as well as from a diversity perspective to study pharmacology in underrepresented individuals[49]. Certain risk factors such as baseline bacterial burden are easily implementable in our clinical simulations, as well as for example the influence of comorbidities or comedications on the pharmacokinetics. However, preclinical (mouse) models are traditionally more homogeneous to reduce noise in the data and be more sensitive to detect pharmacological signals. At the same time, the EBA trials with relatively small sample sizes (<15 per arm) will also not reflect clinical heterogeneity, and risk factors other than those described above have limited relevance for the prediction of the EBA (e.g. cavitation). Similar considerations are applicable to the prediction of EBA in children. Throughout their development, infants and children show changes in their pharmacology that are well established and can be incorporated in our quantitative model-based framework. Pharmacodynamically, the bacterial dynamics and the disease phenotype differences can be modelled based on different animal disease models. Children with tuberculosis younger than 1 year have limited immunity which can be approximated through the immunocompromised athymic (nude) mouse model, while dose older than 1 year without lesion phenotypes can be approximated through the BALB/c mouse model. One limitation of these preclinical models is their reliance of bacterial load measurement, which is complicated in the pediatric population in the context of sputum collection. Alternative models are being developed that are part of future collaborative work in our group. Pharmacokinetically, the development of the metabolic pathways responsible for the elimination of anti-tuberculosis drugs can be incorporated through the use of maturation functions. As a result, pediatric dosing can be projected that will reach similar exposure as in adults given a chosen dose, based on the understanding of the maturation of the relevant elimination pathways and the adult pharmacokinetics.

Building on our translational framework, we aim to predict the efficacy of combination regimens of TB drugs in long-term TB clinical outcomes for phase 2b and 3 from preclinical mouse data. Being able to better understand the time to stable culture conversion and relapse 6 months post treatment will better help us prioritize sterilizing regimens. We hope to achieve this by including the characterization of PKPD relationships in combination regimens by accounting for PKPD drug-drug interactions, as well as characterizing lesion-specific PKPD relationships. Technically, the bacterial dynamic parameters of the translational tool will be re-evaluated and possibly updated through Bayesian methods based on untreated control data of ongoing experiments with novel anti-TB drugs, benefiting from a larger data collection while keeping the structure of the translational tool. Clinical TB disease (e.g., caseation necrosis and cavitation) will be represented in the translational platform to include infection and efficacy data in animal models of TB with more human-like necrotic lesions, such as C3HeB/FeJ mice and New Zealand white rabbits[50]. This will allow us to have a comprehensive platform that informs us not only of monotherapy EBA but also a combination drug regimens efficacy in providing a stable cure and prevention of long term unfavorable outcomes.

In summary, we established a foundation for translating the results from mouse efficacy models to clinical EBA studies through establishing quantitative relationships involving mouse PK and PD, as well as drug dose response *in vivo*. In the future, our platform will be expanded to include combination regimens and longer durations of treatment by accounting for PKPD drug-drug interactions, and necrotic lesion penetration. This innovative platform will accelerate TB drug development and serves as a good example of model-informed drug discovery and development.

Acknowledgments

We acknowledge TB Alliance for support and generously sharing the in-house data of anti-TB drugs linezolid and pretomanid. This work was supported by NIH Grant R01AI-111992.

Author contributions: The manuscript was written by Jacqueline P. Ernest (JE), Janice Jia Ni Goh (JG), Natasha Strydom(NS), Qianwen Wang(QW), Rob Christiaan van Wijk (RW), and Nan Zhang (NZ) and commented on by all authors. JE, JG, NS, QW, RW, and NZ contributed to data collection, model development, data and model management, and code review. Contributions to data collection and model development were as follows, JE: BDQ and RPT; JG: EMB; NS: LZD; QW: DLM, PMD, and MXF; NZ: PZA, RIF, and INH. JG and RW revised the manuscript, including generation of figures and tables. JE and RW carried out code review for all drugs. Amelia Dietchman worked on data collection, human PK model development, simulation, and preliminary model development. Eric Nuermberger provided preclinical data used in our current study, provided substantial scientific context, and edited the manuscript. Rada Savic supervised the whole research.

References

1. Nuermberger, E. L. Preclinical Efficacy Testing of New Drug Candidates. *Microbiol Spectr* **5**, (2017).
2. Jindani, A., Aber, V. R., Edwards, E. A. & Mitchison, D. A. The early bactericidal activity of drugs in patients with pulmonary tuberculosis. *Am. Rev. Respir. Dis.* **121**, 939–949 (1980).
3. Van Norman, G. A. Phase II Trials in Drug Development and Adaptive Trial Design. *JACC Basic Transl Sci* **4**, 428–437 (2019).
4. DRAFT GUIDANCE. Guidance for Industry. https://www.fda.gov/media/87194/download.
5. Danhof, M., de Lange, E. C. M., Della Pasqua, O. E., Ploeger, B. A. & Voskuyl, R. A. Mechanism-based pharmacokinetic-pharmacodynamic (PK-PD) modeling in translational drug research. *Trends Pharmacol. Sci.* **29**, 186–191 (2008).
6. Sasahara, K. *et al.* Pharmacokinetics and Metabolism of Delamanid, a Novel Anti-Tuberculosis Drug, in Animals and Humans: Importance of Albumin Metabolism In Vivo. *Drug Metab. Dispos.* **43**, 1267–1276 (2015).
7. Chen, C., Ortega, F., Alameda, L., Ferrer, S. & Simonsson, U. S. H. Population pharmacokinetics, optimised design and sample size determination for rifampicin, isoniazid, ethambutol and pyrazinamide in the mouse. *Eur. J. Pharm. Sci.* **93**, 319–333 (2016).
8. Zhang Nan *et al.* Mechanistic Modeling of Mycobacterium tuberculosis Infection in Murine Models for Drug and Vaccine Efficacy Studies. *Antimicrob. Agents Chemother.* **64**, e01727-19 (2020).
9. U.S. Department of Health and Human Services, Food and Drug Administration, Center for Drug Evaluation and Research (CDER). Guidance for Industry Estimating the Maximum Safe Starting Dose in Initial Clinical Trials for Therapeutics in Adult Healthy Volunteers. Preprint at https://www.fda.gov/media/72309/download (2005).

10. Svensson, E. M., Dosne, A.-G. & Karlsson, M. O. Population Pharmacokinetics of Bedaquiline and Metabolite M2 in Patients With Drug-Resistant Tuberculosis: The Effect of Time-Varying Weight and Albumin. *CPT Pharmacometrics Syst Pharmacol* **5**, 682–691 (2016).
11. Patterson, S. *et al.* The anti-tubercular drug delamanid as a potential oral treatment for visceral leishmaniasis. *Elife* **5**, (2016).
12. Alghamdi, W. A., Al-Shaer, M. H. & Peloquin, C. A. Protein Binding of First-Line Antituberculosis Drugs. *Antimicrob. Agents Chemother.* **62**, (2018).
13. Dryden, M. S. Linezolid pharmacokinetics and pharmacodynamics in clinical treatment. *J. Antimicrob. Chemother.* **66**, iv7–iv15 (2011).
14. Dorn, C. *et al.* Decreased protein binding of moxifloxacin in patients with sepsis? *GMS Infect Dis* **5**, Doc03 (2017).
15. Committee for Medicinal Products for Human Use (CHMP). Assessment report Pretomanid FGK International non-proprietary name: pretomanid. Preprint at https://www.ema.europa.eu/en/documents/assessment-report/pretomanid-fgk-epar-public-assessment-report_en.pdf (2020).
16. Egelund, E. F. *et al.* Protein binding of rifapentine and its 25-desacetyl metabolite in patients with pulmonary tuberculosis. *Antimicrob. Agents Chemother.* **58**, 4904–4910 (2014).
17. SIRTURO-pi.pdf.
18. Shimokawa, Y. *et al.* Metabolic Mechanism of Delamanid, a New Anti-Tuberculosis Drug, in Human Plasma. *Drug Metab. Dispos.* **43**, 1277–1283 (2015).
19. Jayaram, R. *et al.* Isoniazid pharmacokinetics-pharmacodynamics in an aerosol infection model of tuberculosis. *Antimicrob. Agents Chemother.* **48**, 2951–2957 (2004).

20. Woo, J. *et al.* In vitro protein binding characteristics of isoniazid, rifampicin, and pyrazinamide to whole plasma, albumin, and alpha-1-acid glycoprotein. *Clin. Biochem.* **29**, 175–177 (1996).
21. Lepak, A. J., Marchillo, K., Pichereau, S., Craig, W. A. & Andes, D. R. Comparative pharmacodynamics of the new oxazolidinone tedizolid phosphate and linezolid in a neutropenic murine Staphylococcus aureus pneumonia model. *Antimicrob. Agents Chemother.* **56**, 5916–5922 (2012).
22. Siefert, H. M. *et al.* Pharmacokinetics of the 8-methoxyquinolone, moxifloxacin: a comparison in humans and other mammalian species. *J. Antimicrob. Chemother.* **43 Suppl B**, 69–76 (1999).
23. Rakesh *et al.* Synthesis and evaluation of pretomanid (PA-824) oxazolidinone hybrids. *Bioorg. Med. Chem. Lett.* **26**, 388–391 (2016).
24. Stada Pharmaceuticals,Inc, Cranbury, NJ, 2004. Product Information: pyrazinamide oral tablets, pyrazinamide oral tablets. Preprint at https://www.micromedexsolutions.com/micromedex2/librarian/CS/E2AC9E/ND_PR/evidencexpert/ND_P/evidencexpert/DUPLICATIONSHIELDSYNC/C17097/ND_PG/evidencexpert/ND_B/evidencexpert/ND_AppProduct/evidencexpert/ND_T/evidencexpert/PFActionId/evidencexpert.DoIntegratedSearch?SearchTerm=pyrazinamide&UserSearchTerm=pyrazinamide&SearchFilter=filterNone&navitem=searchALL#cite5_dp.
25. de Steenwinkel, J. E. M. *et al.* Optimization of the rifampin dosage to improve the therapeutic efficacy in tuberculosis treatment using a murine model. *Am. J. Respir. Crit. Care Med.* **187**, 1127–1134 (2013).
26. sanofi-aventis U.S. (per manufacturer), Bridgewater, NJ, 2014. Product Information: PRIFTIN(R) oral tablets, rifapentine oral tablets. Preprint at https://www.micromedexsolutions.com/micromedex2/librarian/CS/A32D19/ND_PR/evidencexpert/ND_P/evidencexpert/DUPLICATIONSHIELDSYNC/0EBD73/ND_PG/evidencexpert/

ND_B/evidencexpert/ND_AppProduct/evidencexpert/ND_T/evidencexpert/PFActionId/evidencexpert.DoIntegratedSearch?SearchTerm=rifapentine&UserSearchTerm=rifapentine&SearchFilter=filterNone&navitem=searchALL#cite2_dp.

27. Assandri, A., Ratti, B. & Cristina, T. Pharmacokinetics of rifapentine, a new long lasting rifamycin, in the rat, the mouse and the rabbit. *J. Antibiot.* **37**, 1066–1075 (1984).
28. Diacon, A. H. *et al.* Randomized dose-ranging study of the 14-day early bactericidal activity of bedaquiline (TMC207) in patients with sputum microscopy smear-positive pulmonary tuberculosis. *Antimicrob. Agents Chemother.* **57**, 2199–2203 (2013).
29. Rustomjee, R. *et al.* Early bactericidal activity and pharmacokinetics of the diarylquinoline TMC207 in treatment of pulmonary tuberculosis. *Antimicrob. Agents Chemother.* **52**, 2831–2835 (2008).
30. Diacon, A. H. *et al.* Early bactericidal activity of delamanid (OPC-67683) in smear-positive pulmonary tuberculosis patients. *Int. J. Tuberc. Lung Dis.* **15**, 949–954 (2011).
31. Donald, P. R. *et al.* The early bactericidal activity of isoniazid related to its dose size in pulmonary tuberculosis. *Am. J. Respir. Crit. Care Med.* **156**, 895–900 (1997).
32. Dietze, R. *et al.* Early and extended early bactericidal activity of linezolid in pulmonary tuberculosis. *Am. J. Respir. Crit. Care Med.* **178**, 1180–1185 (2008).
33. Gosling, R. D. *et al.* The bactericidal activity of moxifloxacin in patients with pulmonary tuberculosis. *Am. J. Respir. Crit. Care Med.* **168**, 1342–1345 (2003).
34. Johnson, J. L. *et al.* Early and extended early bactericidal activity of levofloxacin, gatifloxacin and moxifloxacin in pulmonary tuberculosis. *Int. J. Tuberc. Lung Dis.* **10**, 605–612 (2006).
35. Pletz, M. W. R. *et al.* Early bactericidal activity of moxifloxacin in treatment of pulmonary tuberculosis: a prospective, randomized study. *Antimicrob. Agents Chemother.* **48**, 780–782 (2004).

36. Diacon, A. H. *et al.* Phase II dose-ranging trial of the early bactericidal activity of PA-824. *Antimicrob. Agents Chemother.* **56**, 3027–3031 (2012).

37. Diacon, A. H. *et al.* Bactericidal activity of pyrazinamide and clofazimine alone and in combinations with pretomanid and bedaquiline. *Am. J. Respir. Crit. Care Med.* **191**, 943–953 (2015).

38. Sirgel, F. A. *et al.* The early bactericidal activities of rifampin and rifapentine in pulmonary tuberculosis. *Am. J. Respir. Crit. Care Med.* **172**, 128–135 (2005).

39. Boeree, M. J. *et al.* A dose-ranging trial to optimize the dose of rifampin in the treatment of tuberculosis. *Am. J. Respir. Crit. Care Med.* **191**, 1058–1065 (2015).

40. Kramnik, I. & Beamer, G. Mouse models of human TB pathology: roles in the analysis of necrosis and the development of host-directed therapies. *Semin. Immunopathol.* **38**, 221–237 (2016).

41. Diacon, A. H. *et al.* Multidrug-resistant tuberculosis and culture conversion with bedaquiline. *N. Engl. J. Med.* **371**, 723–732 (2014).

42. Donald, P. R. & Diacon, A. H. The early bactericidal activity of anti-tuberculosis drugs: a literature review. *Tuberculosis* **88 Suppl 1**, S75-83 (2008).

43. Dooley, K. E. *et al.* Safety and pharmacokinetics of escalating daily doses of the antituberculosis drug rifapentine in healthy volunteers. *Clin. Pharmacol. Ther.* **91**, 881–888 (2012).

44. Ngwalero, P. *et al.* Relationship between Plasma and Intracellular Concentrations of Bedaquiline and Its M2 Metabolite in South African Patients with Rifampin-Resistant Tuberculosis. *Antimicrob. Agents Chemother.* **65**, e0239920 (2021).

45. Brown, K. *et al.* Diversity in Clinical Pharmacology: A Call to Action. *Clin. Pharmacol. Ther.* **113**, 483–485 (2023).

46. Imperial, M. Z. *et al.* A patient-level pooled analysis of treatment-shortening regimens for drug-susceptible pulmonary tuberculosis. *Nat. Med.* **24**, 1708–1715 (2018).

47. Imperial, M. Z., Phillips, P. P. J., Nahid, P. & Savic, R. M. Precision-Enhancing Risk Stratification Tools for Selecting Optimal Treatment Durations in Tuberculosis Clinical Trials. *Am. J. Respir. Crit. Care Med.* **204**, 1086–1096 (2021).
48. Ernest, J. P. *et al.* Development of New Tuberculosis Drugs: Translation to Regimen Composition for Drug-Sensitive and Multidrug-Resistant Tuberculosis. *Annu. Rev. Pharmacol. Toxicol.* **61**, 495–516 (2021).

Supplemental Methods

Study design

This translational platform is designed to understand the PK/PD relationships of TB drugs in murine TB model and extrapolate the findings to predict the clinical outcomes of phase 2a studies (Figure 1). Ten drugs were included: bedaquiline (BDQ), delamanid (DLM), ethambutol (EMB), isoniazid (INH), linezolid (LZD), moxifloxacin (MXF), pretomanid (PMD), pyrazinamide (PZA), rifampin (RIF), and rifapentine (RPT). A baseline model using the preclinical data in murine TB model was established previously to quantitate the inhibitory effect of the adaptive immune response on bacterial growth, and a net drug effect can therefore be quantified to establish the PK/PD relationships for the experimental regimens in mice. It was assumed at the free drug concentration level in blood, the PK/PD relationships of TB drugs are comparable between mice and humans. As such, with simulated PK concentrations in humans, the corresponding drug effect of TB drugs in humans can be predicted using the same PK/PD relationships as in mice, as well as the clinical outcome of TB monotherapy regimens in phase 2a trials.

Database

The sources for all data involved in the translational platform development are listed in **Table S1**. Preclinical plasma PK concentrations and lung CFU counts as PD data of BDQ, DLM, EMB, INH, LZD, MXF, PMD, PZA, RIF and RPT were collected from published and unpublished studies or digitized from published studies using Plot Digitizer (http://plotdigitizer.sourceforge.net/). Subacute infection data was used for all drugs except EMB, RPT and LZD for which data from the subacute infection model were not available. Clinical PK data were simulated using published human population PK models or models developed internally. CFU counts in sputum samples for the nine drugs were collected or digitized from published clinical studies.

Model development

All analyses were conducted using NONMEM (version 7.4) via Perl speaks NONMEM (PsN, 4.8.1), R (version 4.1.3) statistical program, and the xpose4 and tidyverse R packages were utilized for model diagnostics and data visualization. The first-order conditional estimation with interaction method (FOCE+I) was used. Mouse PK and PK/PD models were developed and selected based on graphical (goodness of fit plots), statistical (significant change in objective function value), and simulation-based diagnostics (visual predictive checks).

Mouse PK models for all drugs except EMB for which no PK data was available,were developed by fitting the plasma concentration data to one- or two-compartment structural models with first-order absorption and linear or nonlinear (Michaelis-Menten) clearance. Saturable bioavailability was also tested. Additive, proportional, and combination residual error models were tested to describe the error in the observed data (Figure S1). An EMB mouse PK model was utilized from literature to simulate EMB PK[7].

Mouse PK/PD models were developed by incorporating drug effects into a bacterial infection model that describes the infection of *M. tuberculosis* in BALB/c mice (Eq. S1 &Eq. S2). Parameters of the bacterial infection model were re-estimated based on the control data for each drug, to fit the untreated bacterial burden over time for their respective experiment and reliably quantify the drug efficacy separate from the natural infection dynamic (**Table S2**)[52–55]. The inhibitory effect of the adaptive immune response during the treatment period was investigated with certain assumptions. Plasma concentration was used as the independent variable to describe the treatment response for all mouse PD studies except that of PZA using cumulative AUC in acute and sub-acute infection model studies due to the time-varying PZA effect being dependent upon the pH of the microenvironment in the phagosomal compartment during the early treatment period which is, itself, a function of the time ($Conc_{PZA} \times \mathrm{d}t$).

PK/PD relationships for drug effect were optimized by fitting the log-transformed mouse PD data to linear, nonlinear, log-linear, E_{max} and sigmoidal functions. A delay effect was added to optimize the relationship between plasma exposures, time and treatment response (Eq. S3 & S4, Figure S2). An additive error model was used to describe residual error for the mouse PK/PD models. Visual predictive checks (VPCs) of 1000 simulations indicated that the observed data were consistently within the 95% prediction interval of the simulated plasma concentrations and bacterial numbers in the final PK and PK/PD models used for translation for each drug (Figure S2).

$$\frac{dB}{dt} = K_g \times B \times \left(1 - \frac{K_B \times B^{\gamma_B}}{B_{50}^{\gamma_B} + B^{\gamma_B}}\right) \times \left(1 - \frac{K_T \times t^{\gamma_T}}{T_{50}{}^{\gamma_T} + t^{\gamma_T}}\right) \quad - K_d \times B \qquad Eq.S1$$

$$\frac{dB}{dt} = K_g \times B \times \left(1 - \frac{K_B \times B^{\gamma_B}}{B_{50}^{\gamma_B} + B^{\gamma_B}}\right) \times \left(1 - \frac{K_T \times t^{\gamma_T}}{T_{50}{}^{\gamma_T} + t^{\gamma_T}}\right) \quad - K_d \times B - EFF \times B \qquad Eq.S2$$

B*: bacterial number*

t*: incubation time since inoculation*

K_g*: bacterial growth rate*

K_d*: bacterial natural death rate*

K_B*: bacterial number-dependent maximal adaptive immune effect*

B_{50}*: bacterial number that results in half of* K_B

γ_B*: steepness of bacterial number-dependent immune effect relationship*

K_T*: incubation time-dependent maximal adaptive immune effect*

T_{50}*: bacterial number that results half of* K_T

γ_T*: steepness of time-dependent immune effect relationship*

EFF: bacterial killing rate

$$\frac{dA_{\mathrm{delay}}}{dt} = K_{delay} \times \left(\frac{A_2}{V_1} - A_{\mathrm{delay}}\right) \qquad Eq.S3$$

A_{delay}*: the delayed concentration level associated with drug effect*

K_{delay}*: the delay rate of the plasma concentration associated with drug effect*

$$EFF = \frac{A_{delay}^{\gamma} \times E_{max}}{EC_{50}^{\gamma} + A_{delay}^{\gamma}} \qquad Eq.S4$$

E_{max}*: the maximal level of drug effect*

EC_{50}*: the delayed concentration that results in half of the maximal drug effect*

γ*: the steepness of the relationship between the delayed plasma concentration and drug effect*

Clinical PK models were implemented from either published models or developed in NONMEM based on either internal clinical data or extracted literature data (**Table S1.1)**. Single and multi-compartment PK models were tested for drugs modeled. Linear and nonlinear clearance, absorption and bioavailability were also tested when appropriate. Additive, proportional and combination residual error models were tested for the best fit.

Translational model development for EBA prediction

The outcome of clinical EBA studies was predicted by translating the mouse exposure-response relationships to TB patients. Either average patient covariates or no covariates were included for simulating human PK exposures for each drug. The outcomes of EBA studies were predicted by simulating the CFU counts in the sputum of TB patients based on the translatable PK/PD relationships identified in the mouse efficacy studies. Drug dose was as specified in the EBA publication, where weight-based dosing was multiplied by the median weight in the studied population and rounded based on available formulations. In the untreated control arm, typically minimal changes occur during the first two days of study (1-8). As such, the net CFU count change rate (K_{net}) during the first two days of study was considered to be 0 and the changes in CFU counts were only driven by the drug effect *(Eq. S5)*.

$$\frac{dB}{dt} = K_{net} \times B - EFF \times B \qquad Eq. S5$$

K_{net}: the net rate of change in bacterial number in the sputum of TB patients

EBA values were calculated as the daily change of CFU counts over specific days with treatment for ten drugs individually. A thousand simulations for predicting clinical studies were conducted for each drug.

Supplemental Results

Mouse PK and PK/PD Model Development

Mouse PK models of nine out of the ten TB drugs, including BDQ, DLM, INH, LZD, MXF, PMD, PZA, RIF and RPT, were developed using plasma concentration data individually, among which partial data for DLM were digitized from a published study (3 mg/kg)[6]. EMB PK was simulated using a published mouse PK model[7]. Either a one-compartment or two-compartment structural model with first-order absorption and linear or non-linear clearance was used to describe the mouse PK data for each drug (Supplementary Figure S1, Table 1) (*Eq. S*6-S11). Saturable bioavailability was incorporated for PMD and RIF PK models *(Eq. S*12).

First-order Absorption model:

$$\frac{dA_1}{dt} = -K_a \times A_1 \qquad Eq. S6$$

A_1 is the amount of drug in the gastrointestinal tract absorbed into the systemic circulation

K_a is the first-order absorption rate of the drug

t is the time after the dos

One-compartment PK model:

$$\frac{dA_2}{dt} = K_a \times A_1 - K_e \times A_2 \qquad Eq. S7$$

A_2 is the amount of drug in the central compartment

K_e is the elimination rate of the drug from the central compartment

Two-compartment PK model:

$$\frac{dA_2}{dt} = K_a \times A_1 - K_e \times A_2 - \frac{Q}{V_1} \times A_2 + \frac{Q}{V_2} \times A_3 \qquad Eq.\mathrm{S}8$$

$$\frac{dA_3}{dt} = \frac{Q}{V_1} \times A_2 - \frac{Q}{V_2} \times A_3 \qquad Eq.\mathrm{S}9$$

A_3 is the amount of drug in the peripheral compartment

Q is the intercompartmental clearance

V_1 is the volume of the central compartment

V_2 is the volume of the peripheral compartment

Linear clearance:

$$K_e = \frac{CL}{V_1} \qquad Eq.S10$$

CL is the clearance, which is defined as the volume of plasma completely cleared of a drug per unit time

Non-linear clearance:

$$K_e = \frac{K_m \times CL_{in}}{\left(K_m + \frac{A_2}{V_1}\right) \times V_1} \qquad Eq.S11$$

V_{max} is the maximal clearance, which is defined as the maximal volume of plasma completely cleared of a drug per unit time

K_m is the concentration of drug that results in half of the maximal clearance

CL_{in} is the ratio between Vmax and Km.

Saturable bioavailability:

$$F = 1 - \frac{F_{DIF} \times \left(Dose - Dose_{ref}\right)}{Dose - Dose_{ref} + FD_{50}} \qquad Eq.S12$$

F: the extent of drug absorbed from oral dosing compartment into systemic compartment

F_{DIF}*: the maximum difference in bioavailability from 100% (bound between 0% and 100%)*

$Dose_{ref}$*: the reference dose that has 100% bioavailability*

FD_{50}*: the dose achieving half maximal reduction in bioavailability*

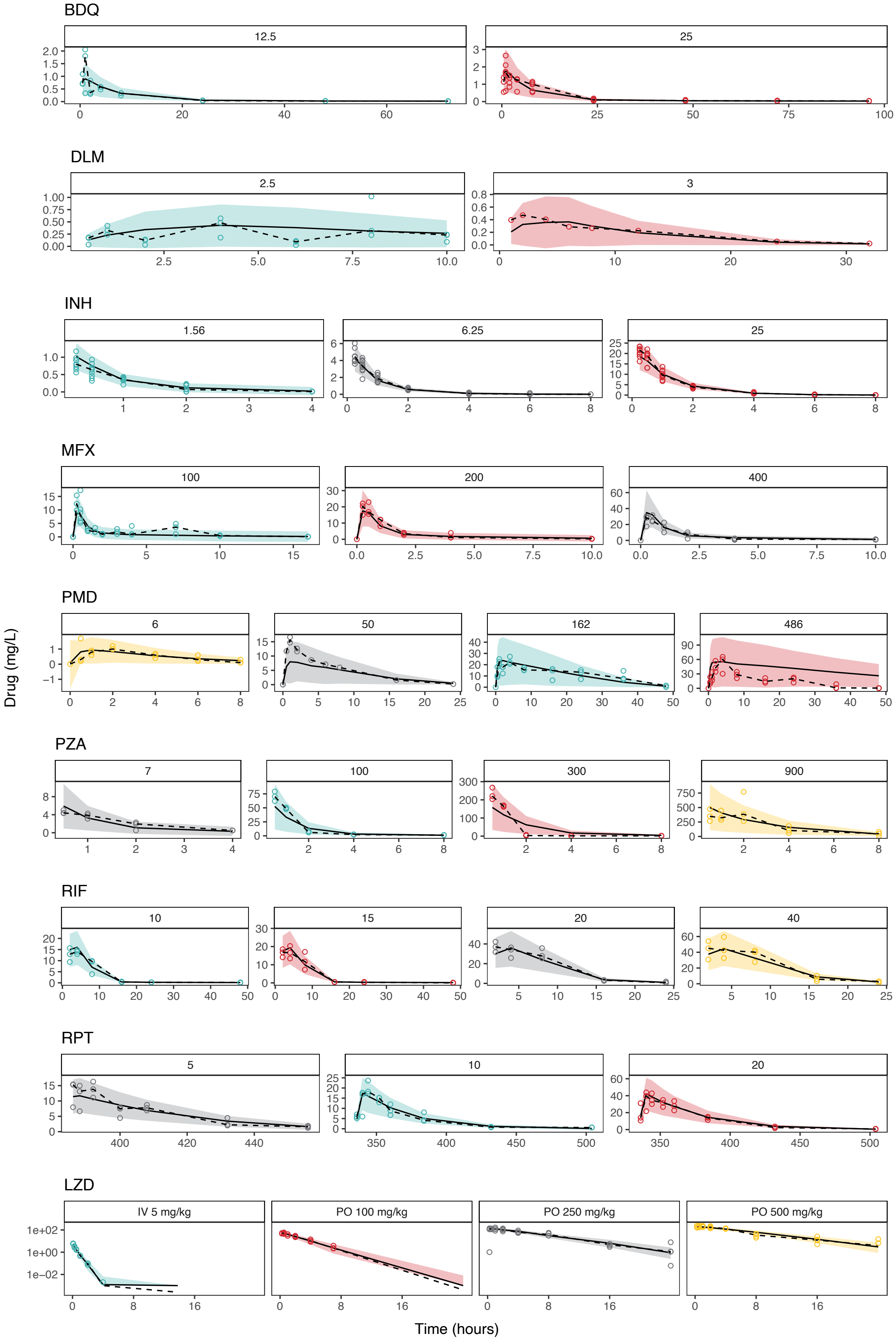

BDQ
12.5
25
DLM
2.5
3
INH
1.56
6.25
25
MFX
100
200
400
PMD
6
50
162
486
PZA
7
100
300
900
RIF
10
15
20
40
RPT
5
10
20
LZD
IV 5 mg/kg
PO 100 mg/kg
PO 250 mg/kg
PO 500 mg/kg
Drug (mg/L)
Time (hours)

SFigure 1.1 Visual predictive checks for final mouse PK models at representative doses. All doses are in mg/kg and orally administered unless otherwise state

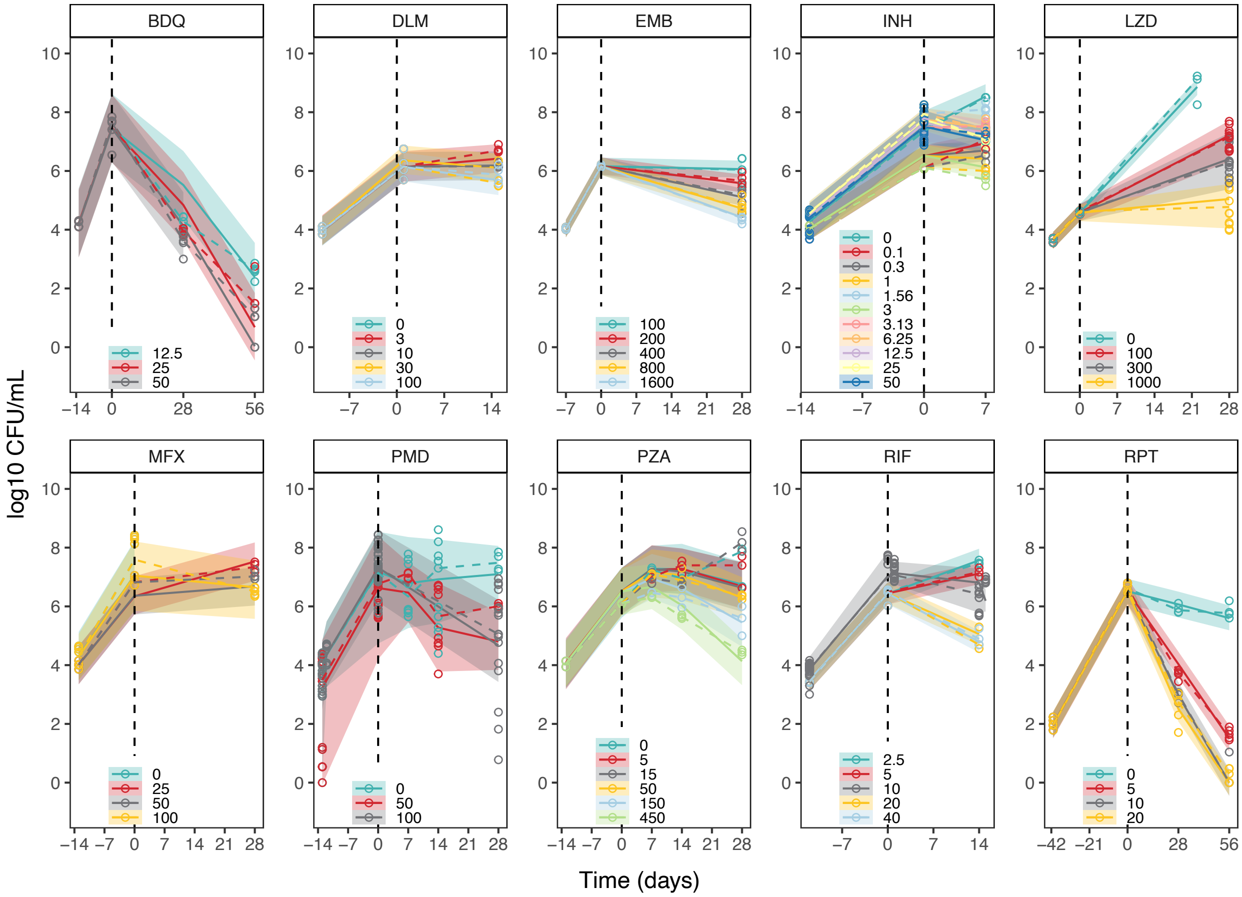

SFigure 1.2 Visual predictive checks for final mouse PD models at representative doses. All doses are in mg/kg and orally administered.

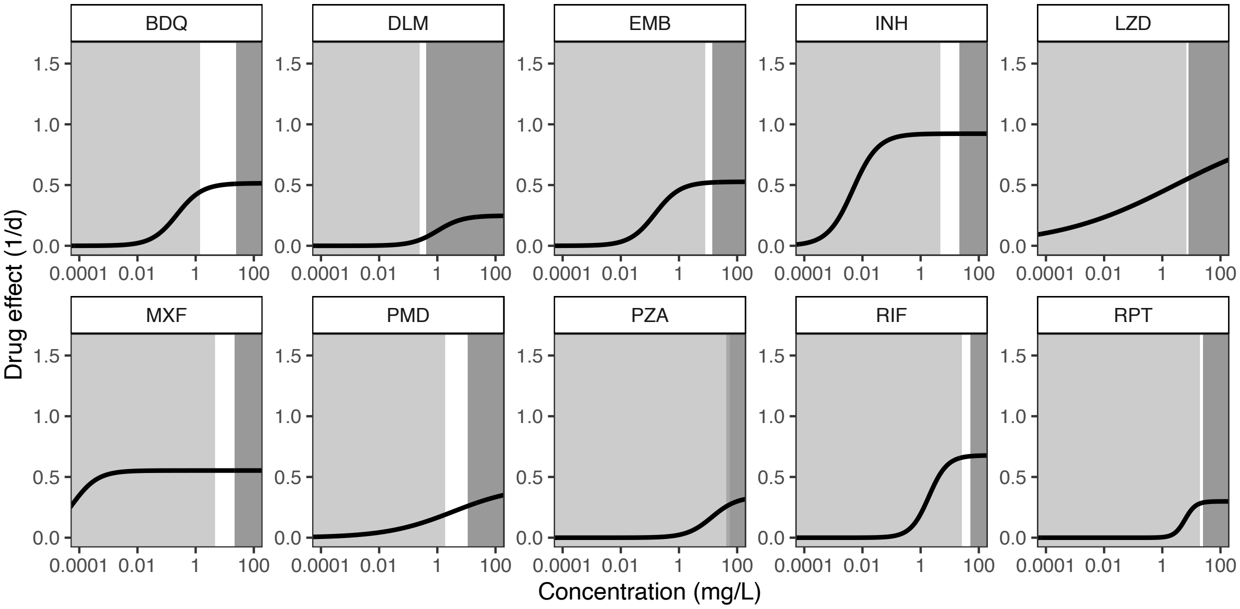

SFigure 1.3 Comparison between human PK concentrations reached at clinical dose

Upper limits of clinical dose levels were defined as concentrations up to the Cmax. Lower limits of safety ranges were defined as theCmax of the maximum tolerated dose tested in humans.

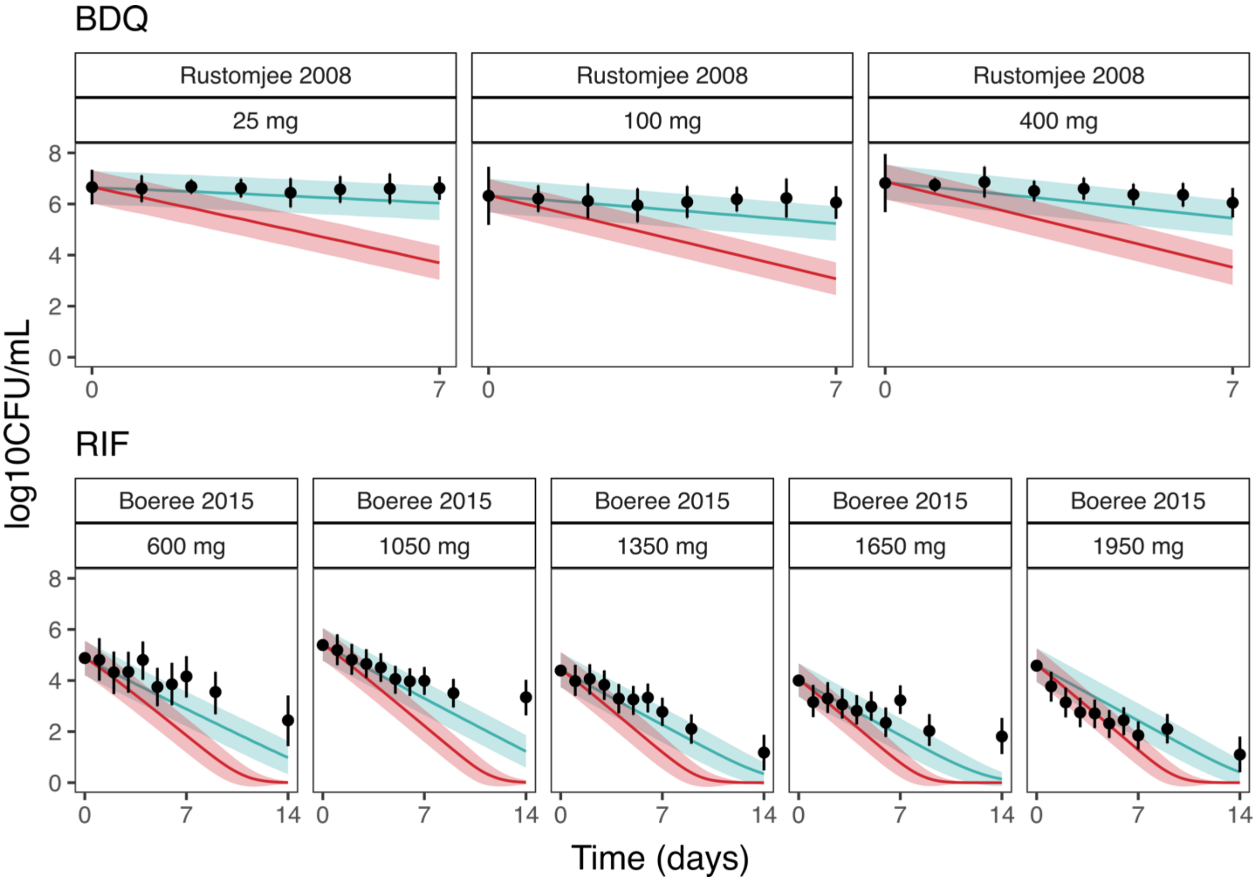

SFigure 1.4 The immune component of the model-based translational platform is essential for accurate prediction of early bactericidal activity.

Comparison of prediction of sputum CFU counts in TB patients during treatment with bedaquiline (BDQ) and rifampin (RIF) at multiple dose levels using PKPD relationships from mathematical models when immune effect (imm) is accounted for and not accounted for.

Table S 1.1 Mouse and human PK and PD database of ten TB drugs.

					Mouse PK					
PK data	BDQ	DLM	EMB	INH	LZD	MXF	PMD	PZA	RIF	RPT
Observations	90	29	186	153	238	74	215	100	66	69
Doses (mg/kg)	12.5, 25, single dose	2.5, 3 single dose	10, 16, 30, 100, 300, 1000 mg/kg	1.56, 6.25, 25, single dose	3*, 5*, 100, 250, 500 single dose	100, 200, 400 daily for 32 days	6, 9, 12,18, 28.8,50,54, 162, 486 single dose; 100 daily for 4 or 8 weeks	7, 22, 100, 300, 600, 900, single dose	10, 15, 20, 40, daily for 2 weeks	5, 10, 20, daily for 16 days
Data Source	JHU[51]	JHU[50,55] and published data[6]	Published data[7]	JHU[57]	JHU[50] & TBA	JHU[51]	JHU[52–55]	JHU[53]	JHU[54]	JHU[51]
Protein binding($f_{u,\ \text{Human/Mouse}}$)	1.0 [50,55]	1.0 [18]	1.0*	1.455 [19,20]	0.986 [13,21]	0.797 [22]	0.99 [23]	0.925 [24] (mouse data JHU unpublished)	4.545 [20,25]	0.422 [26,27]

*personal communication

Mouse PD

PD data	BDQ	DLM	EMB	INH	LZD	MXF	PMD	PZA	RIF	RPT
Animal	Mouse	Mouse	Mouse	Mouse	Mouse	Mouse	Mouse	Mouse	Mouse	Mouse
Observations	57	56	54	414	261	63	283	84	203	75
Doses (mg/kg)	12.5, 25, 50	3,10,30,100	100, 200, 400, 800, 1600	0.1, 0.3, 1, 1.56, 3, 3.13, 6.25, 10, 12.5, 25, 30, 50, 100	7.2, 10, 20, 21.4, 30, 40, 60, 72, 100, 200, 300, 335, 1000	25, 50, 100	50, 100	3, 5, 10, 15, 25, 30, 37.5, 50, 75, 100, 150, 300, 450, 600, 900	2.5, 5, 10, 20, 40, 80, 160, 320, 640	5, 10, 20
Treatment duration (days)	70	56	28	21-56	28	28-56	14-28	28-56	14-56	56
Data Source	JHU[64]	JHU[65] and published data[6]	JHU	JHU[67]	JHU[68] & TBA	JHU[69]	JHU[70]	JHU[71]	JHU[72]	JHU[73]

Human PK

Drugs	PK Structure Model	Doses	No. of Patients / Samples	References
BDQ	3-compartment model with transit absorption	400 mg p.o. daily for 14 days and 200 mg p.o. three times per week for 24 weeks	335 / 2,843	[10]
DLM	2- compartment with linear absorption and saturable bioavailability	100, 200, 300, 400 mg p.o. daily for 14 days	744 / 20,483	[73]
EMB	2- compartment with transit absorption and clearance	800, 1000, 1200, 1500 mg p.o. 5 days/week for ≥4 weeks	189 / 1,869	[74]
INH	2- compartment PK model with linear absorption and clearance	100, 225, 240, 300 and 400 mg p.o. daily, 5 days/week for 2 weeks; 200, 300 and 450 mg p.o.daily, 7 days/week for 1 week	235 / 2,352	[75,76]
LZD	2- compartment with non-linear clearance	300 mg, 600 mg or 1200 mg p.o. for 6 months	104 / 497	[77]
MXF	2- compartment with transit absorption and linear clearance	400 mg p.o. daily for 7 days	241 / 856	[78]

Drugs	PK Structure Model	Doses	No. of Patients / Samples	References
PMD	1- compartment model with transit absorption and dose-dependent absorption, bioavailability, and volume	200, 600, 1000, 1200 mg p.o. daily for 14 days	1,054 / 17,725	79–83
PZA	1- compartment PK model with first order absorption and clearance	1200, 1500 and 2000 mg p.o. daily, 5 days/week for 2 weeks; 1000, 1500 and 2000 mg p.o. daily 7 days/week for 2 months	227 / 3,092	84
RIF	1- compartment PK model (saturable bioavailability and elimination, transit absorption and auto-induction)	10, 20, 25, 30, 35, or 40 mg/kg p.o. daily over 2 weeks	83 / 913	85
RPT	1- compartment PK model (saturable bioavailability, transit absorption and auto-induction)	300, 450, 600, 750, 900, 1050, 1200, 1350, 1500, 1650, 1800 mg p.o. once weekly up to twice daily for up to four months	863 / 4,388	86

Human EBA studies

Drugs	Doses	Baseline ($\log_{10}$ CFU/mL)	References
BDQ	100, 200, 300 and 400 mg (with 200, 400, 500, 700 mg loading dose on first day and 100, 300, 400, 500 mg on second day, respectively)	6.302 (100 mg), 6.001 (200 mg), 6.071 (300 mg), 6.625 (400 mg)	28,29
	25, 100, 400 mg	6.66 (25 mg), 6.32 (100 mg), 6.82 (400 mg)	
DLM	100, 200, 300 and 400 mg	7.06 (100 mg), 6.75 (200 mg), 6.72 (300 mg), 6.82 (400 mg)	30
EMB	15, 25, and 50 mg/kg	6.92	2
INH	9, 18.75, 37.5, 75, 150, 300 and 600 mg	6.491 (9 mg), 6.585 (18.75 mg), 7.169 (37.5 mg), 7.031 (75 mg), 7.115 (150 mg), 6.504 (300 mg), 6.995 (600 mg)	31
LZD	600 mg QD, 600 mg BD	6.34 (600 mg QD), 6.44 (600 mg BD)	32
MXF	400 mg	6.19 (400 mg Johnson), 7.15 (400 mg Pletz), 7.23 (400 mg Gosling)	33–35
PMD	50, 100, 150, 200, 600, 1000, 1200 mg	6.1 (50 mg), 5.8 (100 mg), 6 (150 mg), 6.1 (200 mg Diacon 2012), 6.592 (200 mg Diacon 2010), 6.335 (600 mg), 6.309 (1000 mg), 6.057 (1200 mg)	36,67

Drugs	Doses	Baseline ($\log_{10}$ CFU/mL)	References
PZA	1500, 2000 mg	5.56 (1500mg), 6.910 (2000mg)	[2,37]
RIF	10, 20, 25, 30 and 35 mg/kg	4.88 (10 mg/kg), 4.00 (20 mg/kg), 5.39 (25 mg/kg), 4.58 (30 mg/kg), 4.39 (35 mg/kg)	[25]
RPT	300, 600, 900, 1200 mg	N/A	[38]

*intravenous dosing

Table S 1.2 Final parameters for the bacterial infection model46 for each drug based on the control data.

B_{50} = CFU counts to reach half of K_B, BDQ = bedaquiline, CFU = colony forming units, DLM = delamanid, EMB = ethambutol, INH = isoniazid, K_g = bacterial growth rate, K_d = bacterial death rate, KB = bacterial inhibitory CFU-dependent adaptive immune effect, K_T = bacterial inhibitory time-dependent adaptive immune effect, LZD = linezolid, MXF = moxifloxacin, PMD = pretomanid, PZA = pyrazinamide, RIF = rifampin, RPT = rifapentine, T_{50} = time to reach half of maximal time covariate, γ_B = steepness of the CFU-dependent adaptive immune effect curve, γ_T = steepness of the CFU-dependent adaptive immune effect curve.

Parameter	**BDQ**	**DLM**	**EMB**	**INH**	**LZD**	**MXF**	**PMD**	**PZA**	**RIF**	**RPT**
K_g (day^{-1}) (≤ 4 days)	0.509	0.370	1.11	0.512	0.845	0.461	0.423	0.512	0.512	0.509
K_g (day^{-1}) (> 4 days)	1.2	0.881 04	1.11	1.217	1.510	1.106	1.194	1.217	1.217	1.11
K_d (day^{-1})	0.41	0.41	0.41	0.41	0.41	0.41	0.41	0.41	0.41	0.41
K_B (%)	23.70	28.51	20.3	24.17	39	27.48	68.94	24.17	24.17	23.70
B_{50} ($\log_{10}$ CFU)	6.991	7.024	7.86	7.051	8.339	6.914	7.761	7.051	7.051	6.991
γ_B	2.328	1.232	0.203	2.194	2.9	1.788	0.206	2.194	2.194	2.328
K_T (%)	66.4	64.72	70.2	66.32	69.6	65.15	63.76	66.32	66.32	66.4
T_{50} (day)	19.31	19.73	17.4	19.33	17.5	19.60	18.82	19.33	19.33	19.31
γ_T	5.528	5.788	0.702	5.360	5.13	5.561	5.765	5.360	5.360	5.528

References

1. Chen, C., Ortega, F., Alameda, L., Ferrer, S. & Simonsson, U. S. H. Population pharmacokinetics, optimised design and sample size determination for rifampicin, isoniazid, ethambutol and pyrazinamide in the mouse. *Eur. J. Pharm. Sci.* **93**, 319–333 (2016).
2. Zhang, N. *et al.* Mechanistic Modeling of Mycobacterium tuberculosis Infection in Murine Models for Drug and Vaccine Efficacy Studies. *Antimicrob. Agents Chemother.* **64**, (2020).
3. Sasahara, K. *et al.* Pharmacokinetics and Metabolism of Delamanid, a Novel Anti-Tuberculosis Drug, in Animals and Humans: Importance of Albumin Metabolism In Vivo. *Drug Metab. Dispos.* **43**, 1267–1276 (2015).
4. Irwin, S. M. *et al.* Bedaquiline and Pyrazinamide Treatment Responses Are Affected by Pulmonary Lesion Heterogeneity in Mycobacterium tuberculosis Infected C3HeB/FeJ Mice. *ACS Infect Dis* **2**, 251–267 (2016).
5. Tasneen, R. *et al.* Contribution of the nitroimidazoles PA-824 and TBA-354 to the activity of novel regimens in murine models of tuberculosis. *Antimicrob. Agents Chemother.* **59**, 129–135 (2015).
6. Tyagi, S. *et al.* Bactericidal activity of the nitroimidazopyran PA-824 in a murine model of tuberculosis. *Antimicrob. Agents Chemother.* **49**, 2289–2293 (2005).
7. Bigelow, K. M. *et al.* Pharmacodynamic Correlates of Linezolid Activity and Toxicity in Murine Models of Tuberculosis. *J. Infect. Dis.* **223**, 1855–1864 (2021).
8. Yoshimatsu, T. *et al.* Bactericidal activity of increasing daily and weekly doses of moxifloxacin in murine tuberculosis. *Antimicrob. Agents Chemother.* **46**, 1875–1879 (2002).

9. Almeida, D. *et al.* Paradoxical effect of isoniazid on the activity of rifampin-pyrazinamide combination in a mouse model of tuberculosis. *Antimicrob. Agents Chemother.* **53**, 4178–4184 (2009).
10. Rosenthal, I. M. *et al.* Daily dosing of rifapentine cures tuberculosis in three months or less in the murine model. *PLoS Med.* **4**, e344 (2007).
11. Committee for Medicinal Products for Human Use (CHMP). *CHMP assessment report SIRTURO*. https://www.ema.europa.eu/en/documents/variation-report/sirturo-h-c-2614-ii-0033-g-epar-assessment-report_en.pdf (2019).
12. Shimokawa, Y. *et al.* Metabolic Mechanism of Delamanid, a New Anti-Tuberculosis Drug, in Human Plasma. *Drug Metab. Dispos.* **43**, 1277–1283 (2015).
13. Woo, J. *et al.* In vitro protein binding characteristics of isoniazid, rifampicin, and pyrazinamide to whole plasma, albumin, and alpha-1-acid glycoprotein. *Clin. Biochem.* **29**, 175–177 (1996).
14. Jayaram, R. *et al.* Isoniazid pharmacokinetics-pharmacodynamics in an aerosol infection model of tuberculosis. *Antimicrob. Agents Chemother.* **48**, 2951–2957 (2004).
15. Lepak, A. J., Marchillo, K., Pichereau, S., Craig, W. A. & Andes, D. R. Comparative pharmacodynamics of the new oxazolidinone tedizolid phosphate and linezolid in a neutropenic murine Staphylococcus aureus pneumonia model. *Antimicrob. Agents Chemother.* **56**, 5916–5922 (2012).
16. Dryden, M. S. Linezolid pharmacokinetics and pharmacodynamics in clinical treatment. *J. Antimicrob. Chemother.* **66**, iv7–iv15 (2011).
17. Siefert, H. M. *et al.* Pharmacokinetics of the 8-methoxyquinolone, moxifloxacin: a comparison in humans and other mammalian species. *J. Antimicrob. Chemother.* **43 Suppl B**, 69–76 (1999).
18. Rakesh *et al.* Synthesis and evaluation of pretomanid (PA-824) oxazolidinone hybrids. *Bioorg. Med. Chem. Lett.* **26**, 388–391 (2016).

19. Stada Pharmaceuticals,Inc, Cranbury, NJ, 2004. Product Information: pyrazinamide oral tablets, pyrazinamide oral tablets. Preprint at https://www.micromedexsolutions.com/micromedex2/librarian/CS/E2AC9E/ND_PR/evidencexpert/ND_P/evidencexpert/DUPLICATIONSHIELDSYNC/C17097/ND_PG/evidencexpert/ND_B/evidencexpert/ND_AppProduct/evidencexpert/ND_T/evidencexpert/PFActionId/evidencexpert.DoIntegratedSearch?SearchTerm=pyrazinamide&UserSearchTerm=pyrazinamide&SearchFilter=filterNone&navitem=searchALL#cite5_dp.

20. de Steenwinkel, J. E. M. *et al.* Optimization of the rifampin dosage to improve the therapeutic efficacy in tuberculosis treatment using a murine model. *Am. J. Respir. Crit. Care Med.* **187**, 1127–1134 (2013).

21. sanofi-aventis U.S. (per manufacturer), Bridgewater, NJ, 2014. Product Information: PRIFTIN(R) oral tablets, rifapentine oral tablets. Preprint at https://www.micromedexsolutions.com/micromedex2/librarian/CS/A32D19/ND_PR/evidencexpert/ND_P/evidencexpert/DUPLICATIONSHIELDSYNC/0EBD73/ND_PG/evidencexpert/ND_B/evidencexpert/ND_AppProduct/evidencexpert/ND_T/evidencexpert/PFActionId/evidencexpert.DoIntegratedSearch?SearchTerm=rifapentine&UserSearchTerm=rifapentine&SearchFilter=filterNone&navitem=searchALL#cite2_dp.

22. Assandri, A., Ratti, B. & Cristina, T. Pharmacokinetics of rifapentine, a new long lasting rifamycin, in the rat, the mouse and the rabbit. *J. Antibiot.* **37**, 1066–1075 (1984).

23. Svensson, E. M., Dosne, A.-G. & Karlsson, M. O. Population Pharmacokinetics of Bedaquiline and Metabolite M2 in Patients With Drug-Resistant Tuberculosis: The Effect of Time-Varying Weight and Albumin. *CPT Pharmacometrics Syst Pharmacol* **5**, 682–691 (2016).

24. Wang, X., Mallikaarjun, S. & Gibiansky, E. Population Pharmacokinetic Analysis of Delamanid in Patients with Pulmonary Multidrug-Resistant Tuberculosis. *Antimicrob. Agents Chemother.* **65**, (2020).

25. Jönsson, S. *et al.* Population pharmacokinetics of ethambutol in South African tuberculosis patients. *Antimicrob. Agents Chemother.* **55**, 4230–4237 (2011).
26. Wilkins, J. J. *et al.* Variability in the population pharmacokinetics of isoniazid in South African tuberculosis patients. *Br. J. Clin. Pharmacol.* **72**, 51–62 (2011).
27. Imperial, M. Z., Nedelman, J. R., Conradie, F. & Savic, R. M. Proposed Linezolid Dosing Strategies to Minimize Adverse Events for Treatment of Extensively Drug-Resistant Tuberculosis. *Clin. Infect. Dis.* **74**, 1736–1747 (2021).
28. Zvada, S. P. *et al.* Moxifloxacin population pharmacokinetics and model-based comparison of efficacy between moxifloxacin and ofloxacin in African patients. *Antimicrob. Agents Chemother.* **58**, 503–510 (2014).
29. Salinger David H., Subramoney Vishak, Everitt Daniel & Nedelman Jerry R. Population Pharmacokinetics of the Antituberculosis Agent Pretomanid. *Antimicrob. Agents Chemother.* **63**, e00907-19 (2019).
30. Wilkins, J. J. *et al.* Variability in the population pharmacokinetics of pyrazinamide in South African tuberculosis patients. *Eur. J. Clin. Pharmacol.* **62**, 727–735 (2006).
31. Svensson, R. J. *et al.* A Population Pharmacokinetic Model Incorporating Saturable Pharmacokinetics and Autoinduction for High Rifampicin Doses. *Clin. Pharmacol. Ther.* **103**, 674–683 (2018).
32. Hibma, J. E. *et al.* Rifapentine Population Pharmacokinetics and Dosing Recommendations for Latent Tuberculosis Infection. *Am. J. Respir. Crit. Care Med.* **202**, 866–877 (2020).
33. Diacon, A. H. *et al.* Randomized dose-ranging study of the 14-day early bactericidal activity of bedaquiline (TMC207) in patients with sputum microscopy smear-positive pulmonary tuberculosis. *Antimicrob. Agents Chemother.* **57**, 2199–2203 (2013).
34. Rustomjee, R. *et al.* Early bactericidal activity and pharmacokinetics of the diarylquinoline TMC207 in treatment of pulmonary tuberculosis. *Antimicrob. Agents Chemother.* **52**, 2831–2835 (2008).

35. Diacon, A. H. *et al.* Early bactericidal activity of delamanid (OPC-67683) in smear-positive pulmonary tuberculosis patients. *Int. J. Tuberc. Lung Dis.* **15**, 949–954 (2011).

36. Jindani, A., Aber, V. R., Edwards, E. A. & Mitchison, D. A. The early bactericidal activity of drugs in patients with pulmonary tuberculosis. *Am. Rev. Respir. Dis.* **121**, 939–949 (1980).

37. Donald, P. R. *et al.* The early bactericidal activity of isoniazid related to its dose size in pulmonary tuberculosis. *Am. J. Respir. Crit. Care Med.* **156**, 895–900 (1997).

38. Dietze, R. *et al.* Early and extended early bactericidal activity of linezolid in pulmonary tuberculosis. *Am. J. Respir. Crit. Care Med.* **178**, 1180–1185 (2008).

39. Gosling, R. D. *et al.* The bactericidal activity of moxifloxacin in patients with pulmonary tuberculosis. *Am. J. Respir. Crit. Care Med.* **168**, 1342–1345 (2003).

40. Johnson, J. L. *et al.* Early and extended early bactericidal activity of levofloxacin, gatifloxacin and moxifloxacin in pulmonary tuberculosis. *Int. J. Tuberc. Lung Dis.* **10**, 605–612 (2006).

41. Pletz, M. W. R. *et al.* Early bactericidal activity of moxifloxacin in treatment of pulmonary tuberculosis: a prospective, randomized study. *Antimicrob. Agents Chemother.* **48**, 780–782 (2004).

42. Diacon, A. H. *et al.* Early bactericidal activity and pharmacokinetics of PA-824 in smear-positive tuberculosis patients. *Antimicrob. Agents Chemother.* **54**, 3402–3407 (2010).

43. Diacon, A. H. *et al.* Phase II dose-ranging trial of the early bactericidal activity of PA-824. *Antimicrob. Agents Chemother.* **56**, 3027–3031 (2012).

44. Diacon, A. H. *et al.* Bactericidal activity of pyrazinamide and clofazimine alone and in combinations with pretomanid and bedaquiline. *Am. J. Respir. Crit. Care Med.* **191**, 943–953 (2015).

45. Sirgel, F. A. *et al.* The early bactericidal activities of rifampin and rifapentine in pulmonary tuberculosis. *Am. J. Respir. Crit. Care Med.* **172**, 128–135 (2005).

46. Zhang Nan *et al.* Mechanistic Modeling of Mycobacterium tuberculosis Infection in Murine Models for Drug and Vaccine Efficacy Studies. *Antimicrob. Agents Chemother.* **64**, e01727-19 (2020).

Chapter 2 An in vitro tool kit to predict in vivo monotherapy efficacy for tuberculosis

Abstract

Multiple in vitro assays mimicking different tuberculosis (TB) infection niches are used to test a new compound's drug efficacy. However, there is no consensus on which assays are most predictive of in vivo drug potency. Earlier, we have shown that in vivo EC_{50} is portable between mouse models and patients with TB after adjusting for protein binding and can be used to predict dose-response in early clinical trials. Our goal is to extend this translational platform and develop a further link between preclinical assay results with in vivo estimates of EC_{50} from mouse infection models.

Thirty-three unique in vitro assays were compiled from literature and collaborator data for ten 1st and 2nd line TB drugs. After, feature selection was based on data availability and feature correlation resulting in 15 informative in vitro assays.

To prevent overfitting of the models, in vivo EC_{50} was binned into four distinct bins (< 0.1, 0.1-1, 1-10 and 10-100 mg/L). A multinomial regression was then applied to all possible 1-15 assay combinations and the performance accuracy measured using leave-one-out cross-validation. Based on accuracy metrics, we concluded that 1-3 in vitro assays were sufficient for in vivo EC_{50} prediction, depending on the mouse infection model. This model was then validated by predicting the in vivo mouse EC_{50} of 6 new TB drugs with good accuracy. We then used the median of the binned EC_{50}s as an input into our mouse PK-PD models to simulate mouse CFU predictions. The majority of our in vitro informed PK-PD simulations overlap well with observed data for all sixteen

TB drugs and their dose ranges, demonstrating that our in vitro to in vivo prediction was informative of animal study outcomes.

Our recommendations on the in vitro assays to conduct prior to animal studies can help us to prioritize which drugs are the most likely to succeed clinically, as well as help inform us of the optimal dose range for animal testing, saving resources and accelerating development.

Introduction

Tuberculosis (TB) is back to being the top killer among infectious diseases in the world as of 2022[71]. A standard therapy consisting of a cocktail of four drugs exists[72], but the long treatment duration with the strict adherence required make it difficult for TB to be eradicated[73]. There is thus an urgent need for the development of new drugs that can shorten treatment duration. Many novel drugs have been developed in recent years. However, the process of clinical trials is often long and expensive. Thus, there is a need to better prioritize which drugs are the most likely to succeed clinically.

In vitro assays are typically used to test a new compound for activity even before animal studies are done. Traditionally, the minimum inhibitory concentration (MIC) is used to determine a drug's potency and efficacy against mycobacterium tuberculosis (Mtb)[74]. However, these assays are often carried out in a nutrient-rich media that promotes rapid bacteria growth and are not representative of the physiological conditions in which Mtb often grows in clinically. Over the course of treatment, Mtb growth slows, making it less susceptible to drug treatment[74]. MIC alone might thus be an overestimate of a drug's actual effect for TB cure. Numerous novel in vitro assays have since been developed to mimic this persister state better, through different methods such as depriving Mtb of key nutrients like oleic acid or oxygen, and even the addition of immune cells to simulate what happens in an actual infection[74]. However, there is no consensus on which assays are most predictive of in vivo drug potency and thus informative for furthering drug development.

Previously we have developed an integrated pharmacokinetic-pharmacodynamic (PK-PD) model with bacterial dynamics that allows us to estimate the in vivo potency (EC_{50}) of a drug in mice after accounting for the immune effect[75]. We then found that EC_{50} from mice was portable to humans and could be used to estimate clinical early bactericidal activity (EBA) outcomes in Phase 2a trials. Using in vivo EC_{50} from mice as a standard, we thus wanted to ask two questions:

1) Which in vitro assays, or combination of in vitro assays were the most useful in the prediction of in vivo EC_{50}?
2) Are these in vitro predictions of in vivo EC_{50} useful for the prediction of both in vivo preclinical animal efficacy and clinical efficacy?

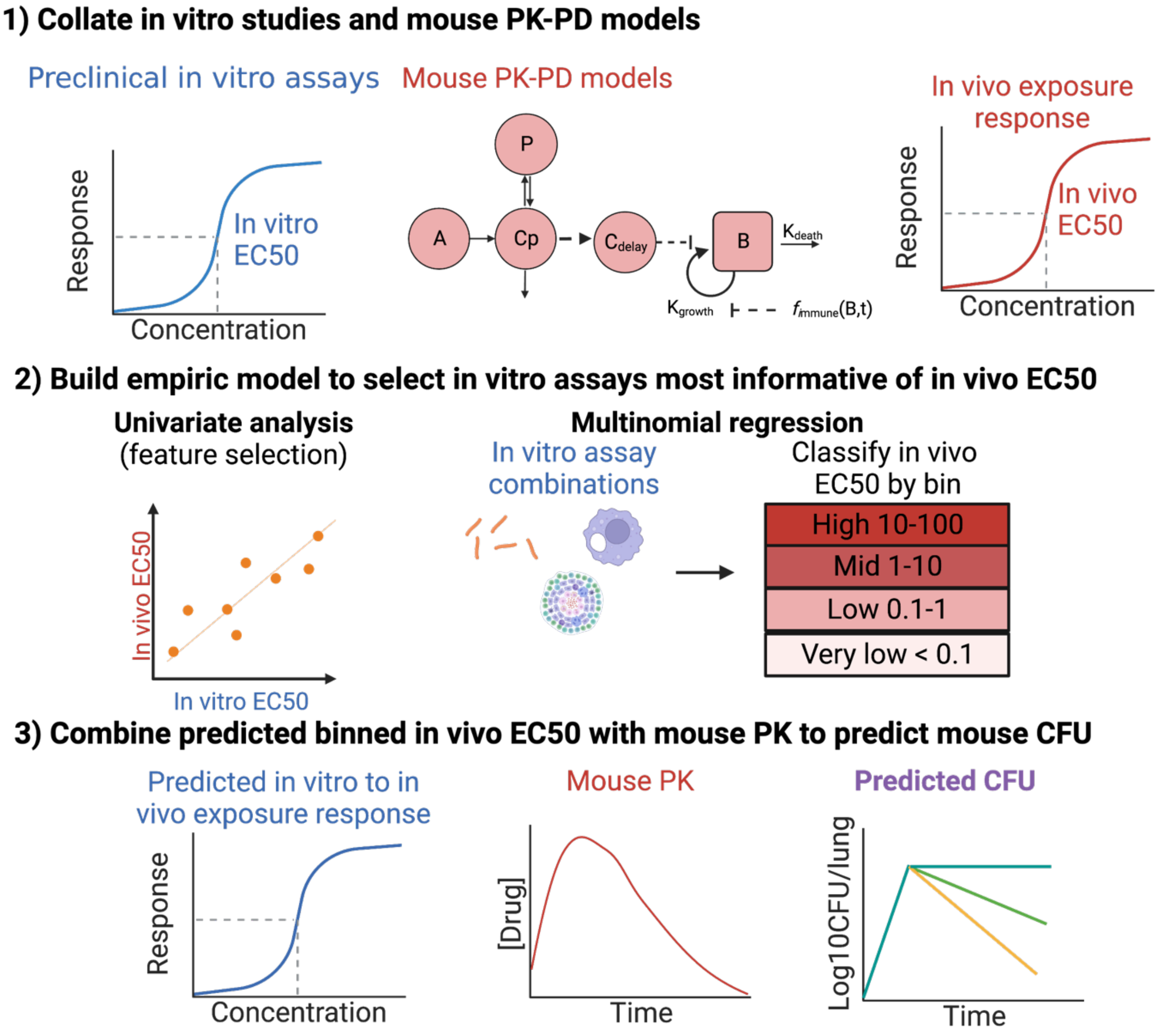
1) Collate in vitro studies and mouse PK-PD models
Preclinical in vitro assays
Mouse PK-PD models
In vivo exposure response
Response
In vitro EC50
Concentration
P
A
Cp
Cdelay
B
Kdeath
Kgrowth
fimmune(B,t)
Response
In vivo EC50
Concentration
2) Build empiric model to select in vitro assays most informative of in vivo EC50
Univariate analysis (feature selection)
In vivo EC50
In vitro EC50
Multinomial regression
In vitro assay combinations
Classify in vivo EC50 by bin
High 10-100
Mid 1-10
Low 0.1-1
Very low < 0.1
3) Combine predicted binned in vivo EC50 with mouse PK to predict mouse CFU
Predicted in vitro to in vivo exposure response
Response
Concentration
Mouse PK
[Drug]
Time
Predicted CFU
Log10CFU/lung
Time

Figure 2.1 A three step translational platform to find the most predictive in vitro assays for translation into in vivo outcomes in mice.

In vitro assay potencies were compared against in vivo EC_{50} from integrated mouse PK-PD models with bacterial dynamics to determine the best assay combination. The predicted in vivo EC_{50} from the multinomial regression model was then used to predict the mouse CFU profile.

Compiling a rich dataset of in vitro data

A total of ten drugs were chosen for the study. These drugs were bedaquiline (BDQ), delamanid (DLM), ethambutol (EMB), isoniazid (INH), moxifloxacin (MFX), linezolid (LZD), pretomanid (PMD), pyrazinamide (PZA), rifampicin (RIF) and rifapentine (RPT). Drugs were chosen based on the criteria that they had a corresponding integrated bacterial dynamics PK-PD model built, as well as a minimum of 5 in vitro assay results from feature selection prior to imputation for analysis.

In vitro assays and their reported drug potencies e.g. EC_{50} were compiled from both published literature, as well as from our collaborators. To ensure fair comparison across drug potencies, all drug concentrations were standardized to mg/L and different measure outcomes e.g. EC_{90}, EC_{80}, EC_{99} were converted to EC_{50} using the assumption that the Hill coefficient in a log-logistic dose-response curve was 1. This held true for most assays we tested where a full dose response curve was available (SFig 2.1). When the percent activity was not stated for MIC, we assumed it to be EC_{50}.

Building a translational mouse- human PK-PD dataset and model repository

Our mouse model repository was built on rich longitudinal data pooled from both in-house databases and literature, including observed or published mouse PK and PD data (lung CFU counts) and human PD data (sputum CFU counts), as well as simulated human PK data using published models as detailed in our previous publication[76,77]**.** In total, mouse PK and PD data were collected from 2,770 BALB/c mice. Multiple dose levels were investigated in both mouse PK and efficacy (PD) studies and human PK and EBA (PD) studies. All the drugs were administered orally in mouse and human PK and PD studies. Mouse plasma samples were collected after either a single dose or multiple doses of treatment, while human plasma samples were collected only after multiple dosing. Depending on the size of the infectious dose and the duration of incubation before treatment started, mouse efficacy studies were grouped as acute infection (inoculum size no less than 3.5 log10 CFU/ml and incubation period no more than 8 days), sub-acute infection (inoculum size no less than 3.5 log10 CFU/ml and incubation period between 10 and 17 days) and chronic infection studies (inoculum size less than 3.5 log10 CFU/ml and incubation period no less than 21 days). Mice were dosed five days per week and CFU counts were collected 3 days after the last dose for any given mouse. In human EBA studies, the treatment duration ranges between 1 day and 14 days. Integrated PK-PD models with bacterial dynamics were applied to the mice data to elucidate the in vivo exposure response using NONMEM 7.5.1 and Perl Speaks Nonmem (PsN) 5.3.0 . Detailed methods on the model building can be found in Ernest et al[78].

Exploratory analyses and machine learning to determine translatable assays

Computational analyses were done using R 4.1.3. Initial exploratory analyses were done using tidyverse, pheatmap, drc, nnet and cor R packages. Feature selection was carried out using the following criteria (Fig 2.2a).

1) In vitro assay must contain information for at least 3 drugs of interest
2) Between highly correlated assays, the most representative assay with the most pairwise correlations (> 6 edges in a network plot) would be chosen.

In vitro assays were first evaluated together using both multivariate and multinomial regression. Models to predict in vivo mouse EC_{50} were done individually for each mouse infection type as the in vivo EC50 trends changed between infection models for the same drug.

After, we carried out feature perturbation to test which in vitro assays were most informative, both multiple linear regression and multinomial linear regression were applied to the dataset to predict in vivo EC_{50} from in vitro EC50. All possible 1-15 combinations of in vitro assays were generated for evaluation of a good in vitro assay combination. Due to a small dataset, we did leave one out cross validation (LOOCV) instead of traditional 80:20 training:testing for machine learning. Our metrics for a good model were accuracy and R^2 for multiple linear regression, and accuracy, defined as the number of times the left out drug was predicted in the correct bin for multinomial linear regression. The bins for in vivo EC_{50} were decided based on the distribution of all in vivo EC50 values in the dataset. For drugs with missing assay values, the assay values were imputed as the median potency of all the other drugs.

Combining PK models from mice with in vitro-in vivo predicted exposure response

To find out how well our in vitro-in vivo (IVIV) predicted exposure-response was able to predict drug efficacy in mice, we combined that relationship with mouse PK models from our model repository. The Emax in each exposure-response curve was estimated as the median Emax of all ten drugs for each mouse infection model. Simulations of bacterial burden in mice (CFU) over time were done using both the raw EC50 values for selected in vitro assays as well as the median of the binned EC50 values as predicted by our multinomial regression algorithm. The PK-PD simulations were done using NONMEM 7.5.1 without parameter estimates. Variability was simulated using PK variability in the models and variability in CFU at day 0 in mice prior to treatment. The model predictions were evaluated using visual predictive checks (VPCs), by overlaying the median and 95% prediction interval of the model over observed results from mouse studies. A good model would have the prediction intervals overlapping well with the observed data.

Combining PK models from humans with in vitro-in vivo predicted exposure response

To predict clinical EBA, the predicted in vivo exposure-response relationship was combined with previously validated population PK models from literature to build a PK-PD model that was then used for simulation. Similarly, our models were evaluated using VPCs against observed clinical EBA data from 14 different studies for all 10 drugs.

Model validation using 6 new TB drugs

To further validate our model, we compiled a list of the best performing in vitro assays from our initial multinomial classification and reached out to various collaborators to help us test new compounds against these in vitro assays. We then input the in vitro assay EC_{50} values from our multinomial classifier trained using the original to predict the in vivo mouse EC_{50} for these new compounds. The new compounds were sutezolid (SUT), TBAJ587, TBAJ876, TBI223, MK7762 and BTZ043, all of which are drugs currently being developed for the treatment of TB. We retrained the model using all 16 drugs using an 80:20 training:testing split only if the initial model did not perform well.

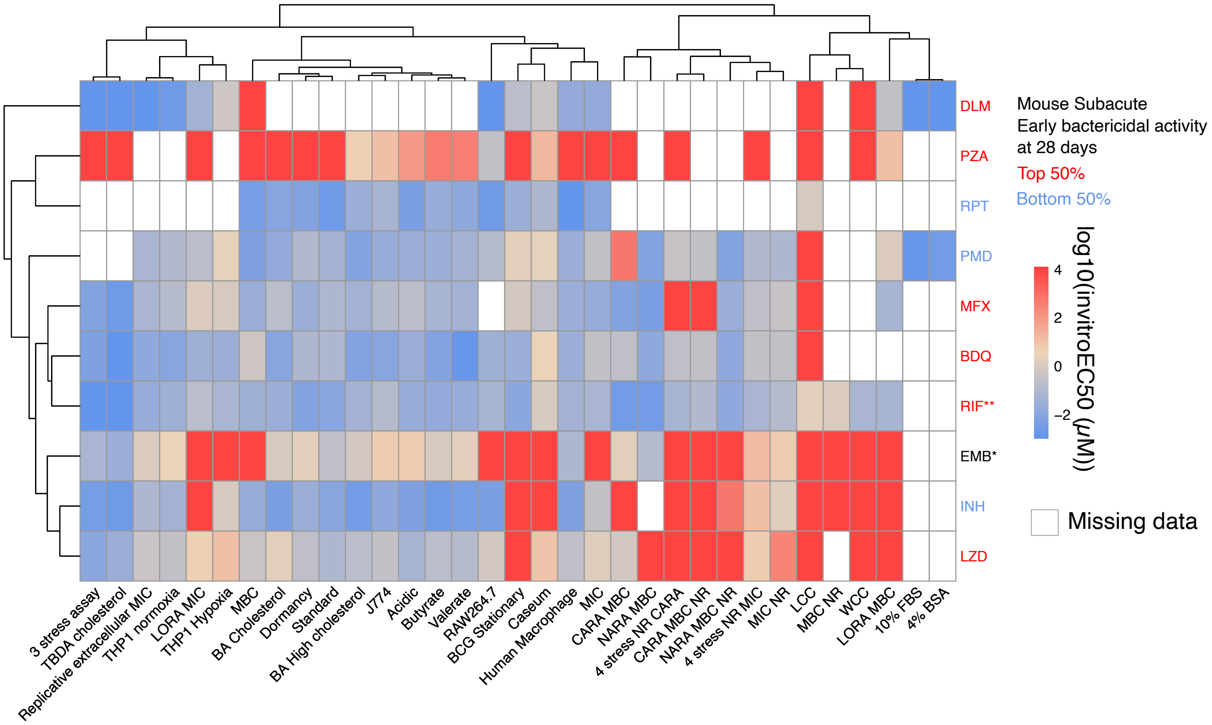

Figure 2.2 A total of 33 in vitro assays were compiled for 10 TB drugs

Overview of assays and drugs available in database as heatmap with hierarchical clustering – drug potency alone was unable to account for drug efficacy. Drugs reported as inactive at highest concentration tested were assigned a value of 9999. Drugs in the dataset were ranked by their efficacy, defined as the change in bacterial burden at day 28 of treatment using the maximum dose in the dataset into either the top or bottom 50%.

A rich dataset of in vitro assays was compiled

We compiled 33 unique assays for 10 drugs with corresponding PK-PD models and clinical data available. Most of these assays only had reported drug potencies rather than a full dose-response curve. Hence, we focused on EC50 rather than Emax to generate the exposure-response.

Out of these 33 assays, 5 were macrophage assays involving the addition of an immune cell line to Mtb, 24 were a change in culture condition, either via a media formulation or oxygen deprivation, 3 were nutrient-rich conditions e.g. MIC and 1 was an ex vivo assay using harvested caseum from New Zealand White rabbits (Fig 2.2).

Drug potency (EC50) alone was insufficient to predict in vivo efficacy in mice

The drugs were then ranked by efficacy using the maximum tested dose in animal studies against their total drop in CFU at 28 days from baseline in a subacute mouse infection model. A subacute model was chosen for evaluation as these were the models we used previously for translation to clinical EBA predictions. Despite there being an extensive database, there was no clear separation of drug effect in mice based on drug potency alone, suggesting that considering the PK profile and thus exposure of each drug would be important too in determining the early efficacy of a drug (Fig 2.2).

(a)

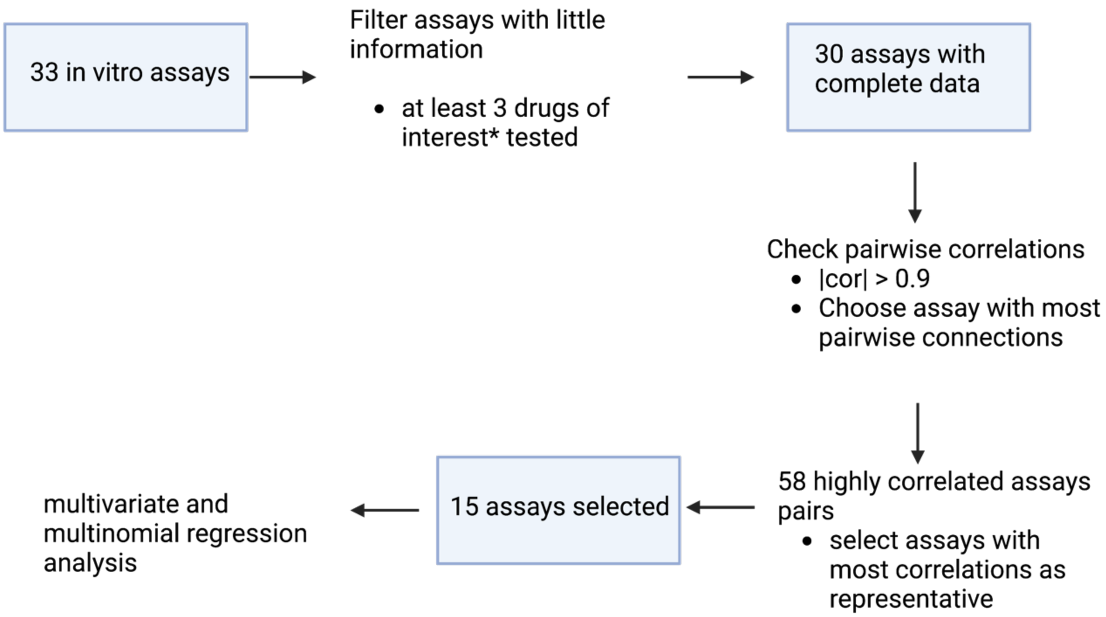
33 in vitro assays
Filter assays with little information
at least 3 drugs of interest* tested
30 assays with complete data
Check pairwise correlations
|cor| > 0.9
Choose assay with most pairwise connections
58 highly correlated assays pairs
select assays with most correlations as representative
15 assays selected
multivariate and multinomial regression analysis

*Drugs of interest: BDQ, DLM, INH, EMB, PZA, PMD, MXF, LZD, RIF, RPT

(b)

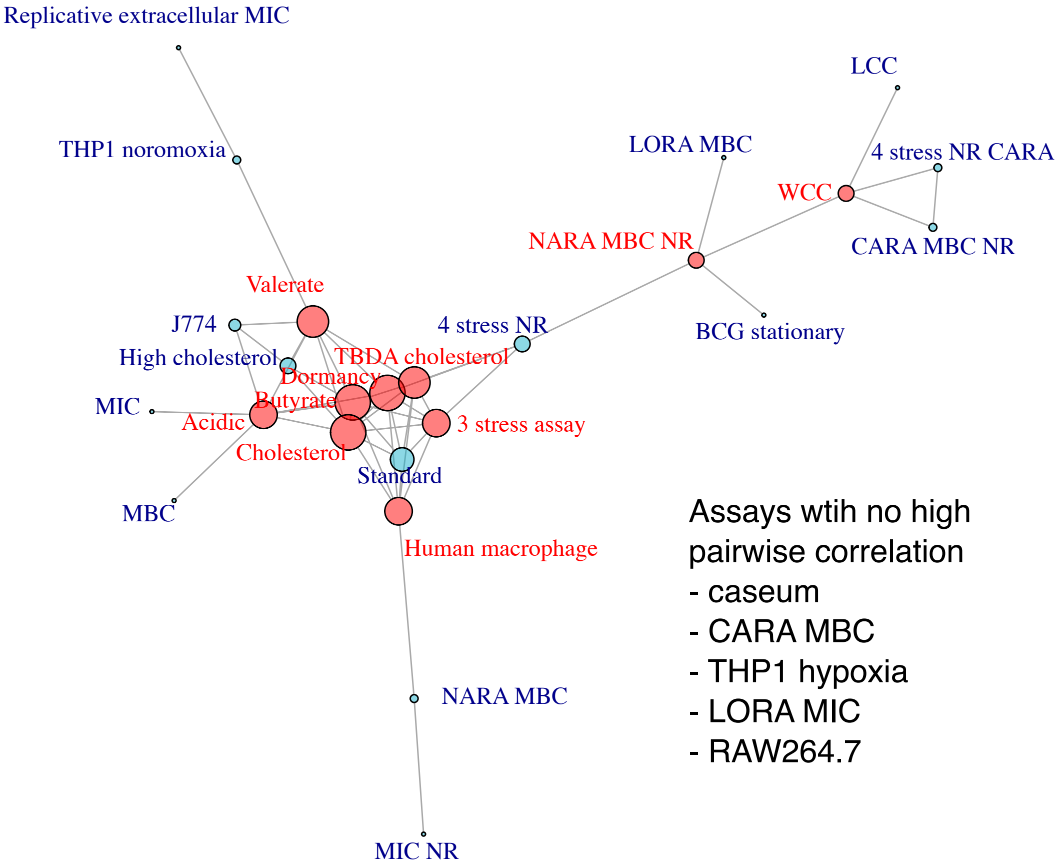
Replicative extracellular MIC
THP1 noromoxia
LCC
LORA MBC
4 stress NR CARA
WCC
NARA MBC NR
CARA MBC NR
Valerate
J774
4 stress NR
BCG stationary
High cholesterol
TBDA cholesterol
Dormancy
Butyrate
MIC
Acidic
3 stress assay
Cholesterol
Standard
MBC
Human macrophage
NARA MBC
MIC NR

Assays wtih no high pairwise correlation
- caseum
- CARA MBC
- THP1 hypoxia
- LORA MIC
- RAW264.7

(c)

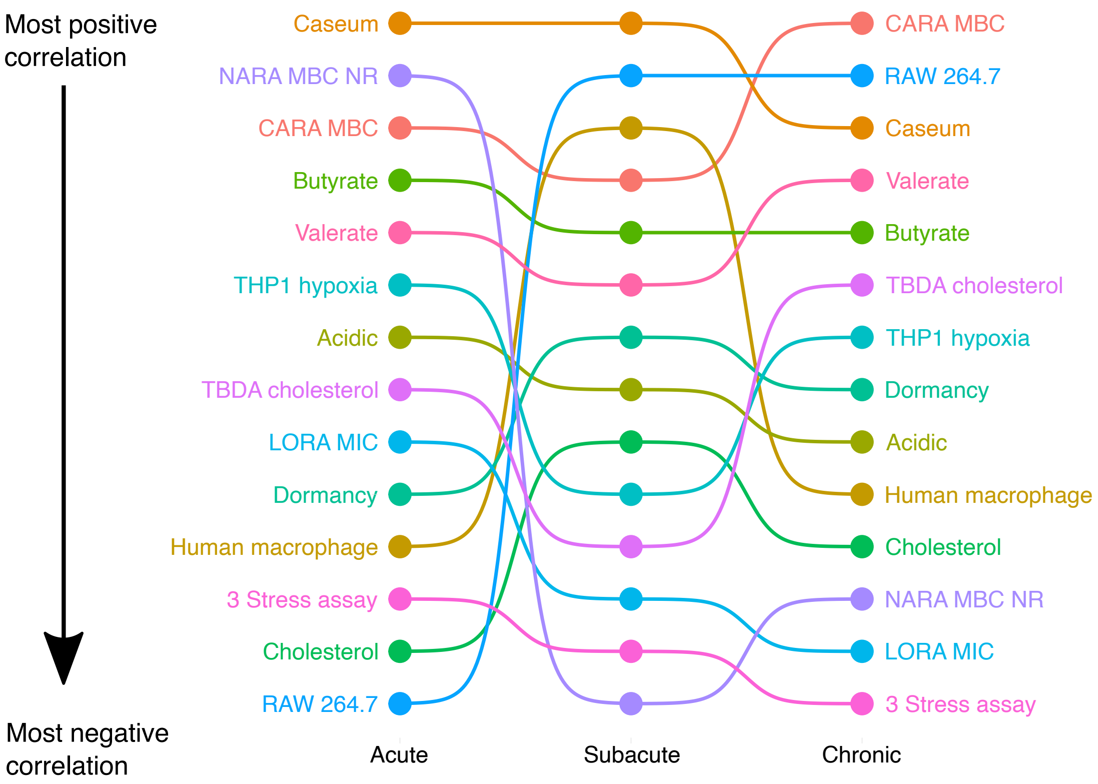

Figure 2.3 Feature selection criteria for in vitro assays prior to multivariate and multinomial regression to predict in vivo EC50

(a) Feature selection pipeline for multivariate and multinomial regression pipeline for the robust prediction of in vivo EC50 from in vitro EC50. For multinomial regression, in vivo EC50 values were binned based on their distribution and the median of each bin used to estimate the exposure response relationship in vivo.
(b) High correlations between in vitro assays exist for 25 assays. Assays were highly correlated when pairwise correlation (r) was larger than 0.9. The assays highlighted in red have more than 6 high correlations among in vitro pairwise comparisons and were chosen as representative of other highly correlated in vitro assays.
(c) Ranked in vitro EC50 correlations among 15 selected features against in vivo EC50 values. Caseum consistently held top correlations across mouse infection models among chosen assays. The associated plots are available in SFig1.

Feature selection picked in vitro assays most representative of the dataset

To reduce the amount of redundancy in the model, we carried out feature selection on all 33 assays, selecting assays that had information on more than 3 drugs of interest, as well as assays with a high number of pairwise correlations (>6 edges in a network plot of pairwise in vitro assay EC_{50} correlations) (Fig 2.3a). 3 assays did not have sufficient information about drugs of interest and were discarded. Using pairwise correlation, we found 58 in vitro assay pairs with $|R| > 0.9$ indicating strong pairwise correlation. Five assays, caseum, CARA MBC, THP1 hypoxia, LORA MIC and RAW264.7 did not have high pairwise correlations with other assays and were selected as features. Out of the remaining 25 drugs, 8 drugs with more than 6 edges in the large cluster were chosen and the other assays based on the highest number of connected edges within a smaller cluster. NARA MBC NR and WCC were also chosen as they were representative of their clusters (Fig 2.3b). A total of 15 in vitro assays were selected for further testing.

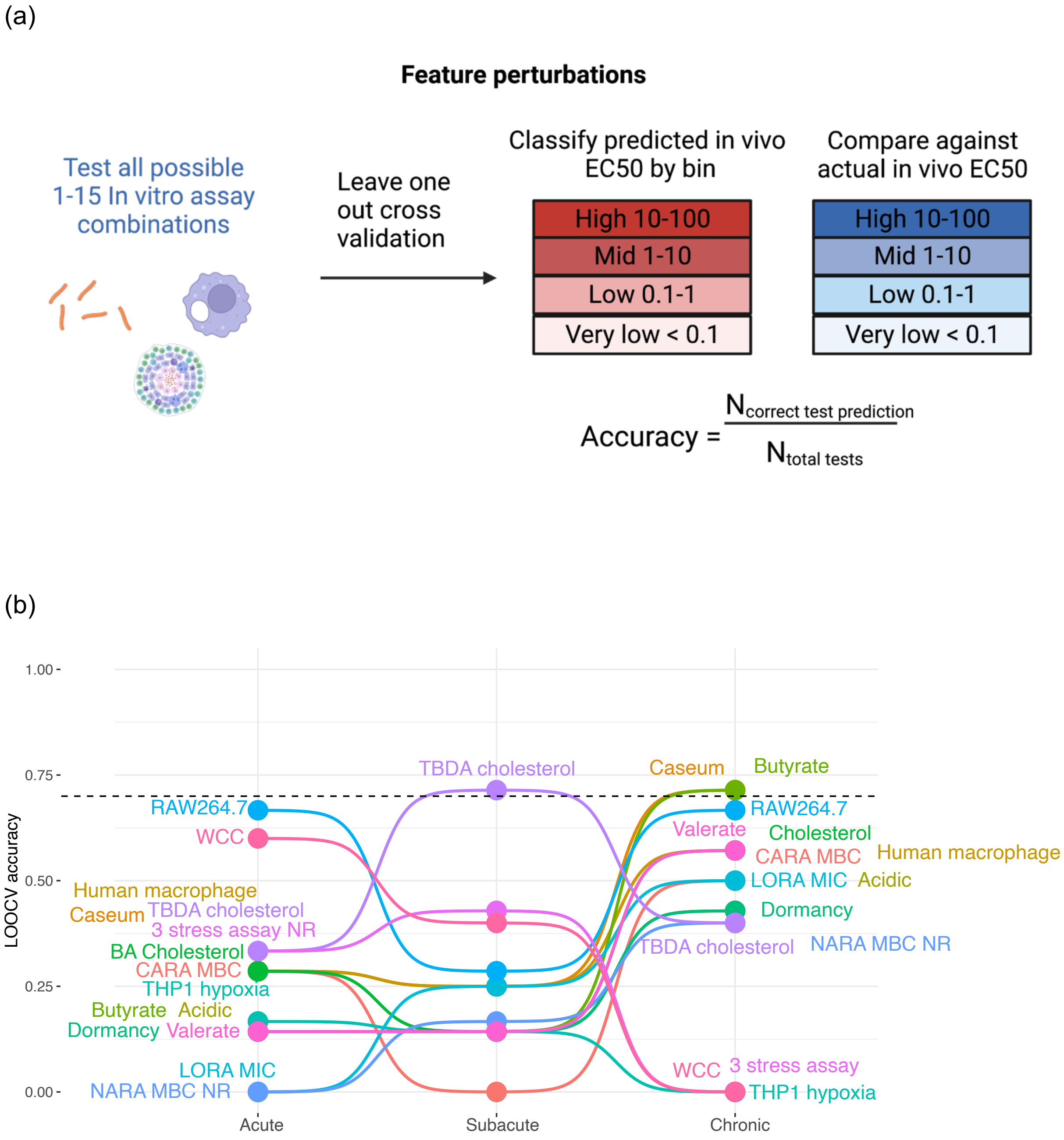
(a)
Feature perturbations
Test all possible 1-15 In vitro assay combinations
Leave one out cross validation
Classify predicted in vivo EC50 by bin
High 10-100
Mid 1-10
Low 0.1-1
Very low < 0.1
Compare against actual in vivo EC50
High 10-100
Mid 1-10
Low 0.1-1
Very low < 0.1
Accuracy = N correct test prediction / N total tests
(b)
LOOCV accuracy
1.00
0.75
0.50
0.25
0.00
Acute
Subacute
Chronic
RAW264.7
WCC
Human macrophage
Caseum
TBDA cholesterol
3 stress assay NR
BA Cholesterol
CARA MBC
THP1 hypoxia
Butyrate
Acidic
Dormancy
Valerate
LORA MIC
NARA MBC NR
TBDA cholesterol
Caseum
Butyrate
RAW264.7
Valerate
Cholesterol
CARA MBC
Human macrophage
LORA MIC
Acidic
Dormancy
TBDA cholesterol
NARA MBC NR
WCC
3 stress assay
THP1 hypoxia

(c)

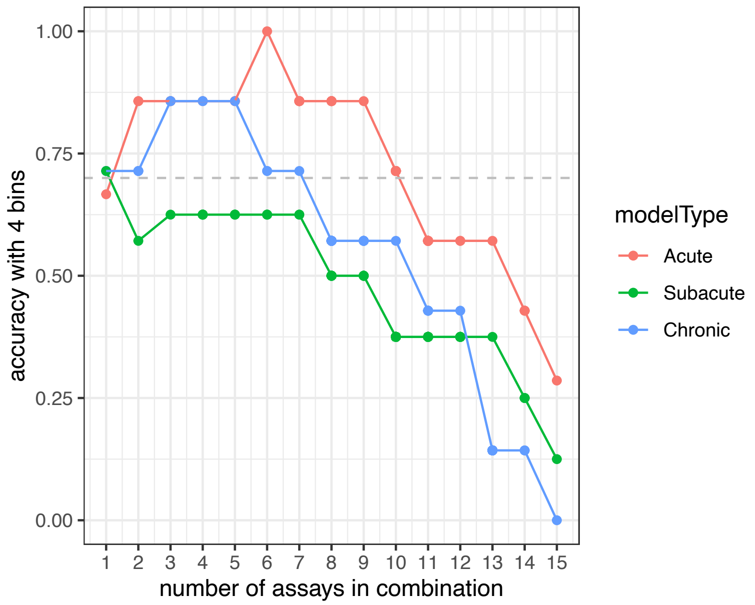

accuracy with 4 bins
1.00
0.75
0.50
0.25
0.00
1
2
3
4
5
6
7
8
9
10
11
12
13
14
15
number of assays in combination
modelType
Acute
Subacute
Chronic

(d)

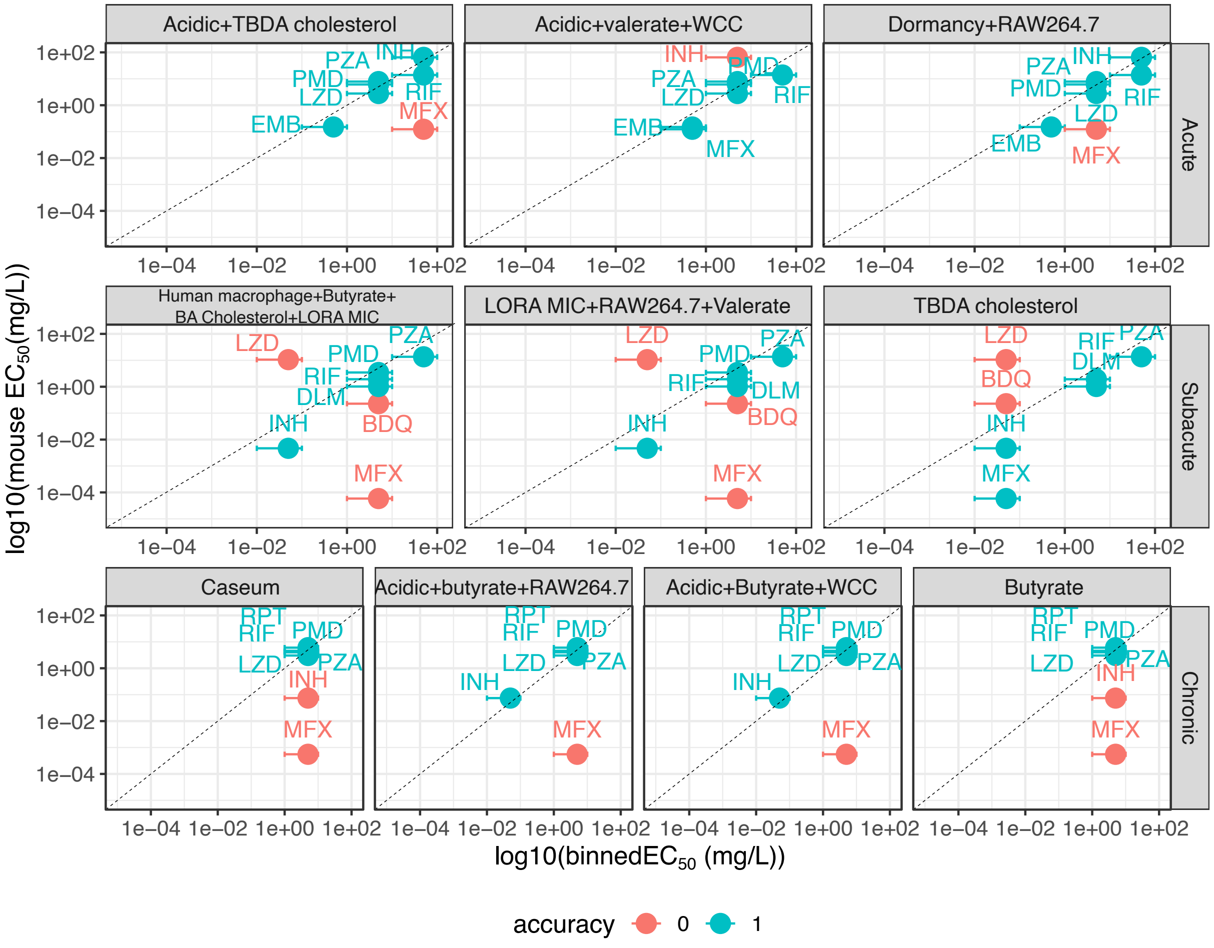

Acidic+TBDA cholesterol
Acidic+valerate+WCC
Dormancy+RAW264.7
Acute
Human macrophage+Butyrate+
BA Cholesterol+LORA MIC
LORA MIC+RAW264.7+Valerate
TBDA cholesterol
Subacute
Caseum
Acidic+butyrate+RAW264.7
Acidic+Butyrate+WCC
Butyrate
Chronic
PZA
INH
PMD
LZD
RIF
MFX
EMB
RPT
DLM
BDQ
1e+02
1e+00
1e−02
1e−04
log10(mouse EC_{50}(mg/L))
log10(binnedEC_{50} (mg/L))
accuracy
0
1

Figure 2.4 Feature perturbation to find minimum number of features to make reliable predictions

(a) Feature perturbation to find minimum number of features to make reliable prediction. Despite moderate correlations between features and in vivo EC50, prediction accuracy of multivariate and multinomial regression was low, prompting investigation using feature perturbation.
(b) Single assays were able to classify in vivo EC50 with reasonable accuracy.
(c) Feature perturbation suggests 4 assays or less produced decent prediction accuracy across all infection models. This suggests feature interactions are detrimental to model accuracy.
(d) test drug results from leave one out cross validation of all 10 drugs with the best performing combinations.

Table 2.1 Suggested in vitro assays for in vivo EC50 predictions based on 10 drugs

Mouse infection model	**Median in vivo E_{max}**	**Best performing assay combinations**
Acute	0.968	• Dormancy, RAW264.7 • **Acidic, TBDA cholesterol** • Acidic, Valerate, WCC
Subacute	0.594	• TBDA cholesterol • LORA MIC, RAW264.7, Valerate • **Human Macrophage, Butyrate, BA Cholesterol, LORA MIC**
Chronic	0.421	• Acidic, Butyrate, RAW264.7 • Acidic, Butyrate, WCC • **Caseum** • Butyrate

Caseum assay shows good univariate correlation against in vivo EC_{50} across all infection models

To further understand how each assay might contribute to the prediction of in vivo EC_{50}, we did a univariate correlation analysis of each in vitro assay EC_{50} against their corresponding in vivo EC_{50} (Fig 2.3c). The ranking shows that caseum was the top assay in both acute and subacute mouse infection models, and third to CARA MBC and RAW264.7 assays in the chronic mouse infection model. This suggests that the caseum assay would be a good robust predictor for in vivo mouse EC_{50} prediction.

Feature perturbation suggests 4 or less in vitro assays gave a good prediction of in vivo EC50 across mouse infection model types

Multivariate regression was unable to give good predictions using all 15 selected features due to overfitting of the training dataset (SFig2.3a). We then tried multinomial regression by classifying the in vivo EC_{50} values into four bins (very low <0.1, low 0.1-1, mid 1-10, high > 10). While the test prediction improved slightly, it was still insufficient to get a reliable classification of the in vivo EC_{50}(SFig2.3b). However, as we saw low to moderate correlations against in vivo mouse EC_{50} for all correlations (SFig2.2), it was possible that there were multiple interacting features within the dataset, leading us to attempt feature perturbation to find the minimum number of features required to make a reliable prediction. We simulated all possible 1-15 combinations of in vitro assays based on the 15 assays from feature selection (Fig 2.4a). Accuracy from LOOCV showed that a combination of 3 assays gave good predictions (>70%) for all mouse infection models. Individual assay performance using LOOCV was sufficient for subacute and chronic mouse infection models using TBDA cholesterol and caseum assay respectively. A single assay was not able to predict acute mouse infection EC_{50} with good accuracy (Fig 2.4b). Based on the accuracy of the best performing combination of assays, we suggest that 4 assays or less are sufficient to predict in vivo mouse EC_{50} (Fig 2.4c). We suggest the following combinations for each mouse infection model based on which combinations gave the highest accuracy with LOOCV and how often an assay appeared among the top combinations. If two combinations were equally ranked, we then chose the assay that was less biologically complex as the preferred assay. Our suggestions on assay combinations are in Table 2.1.

(a)

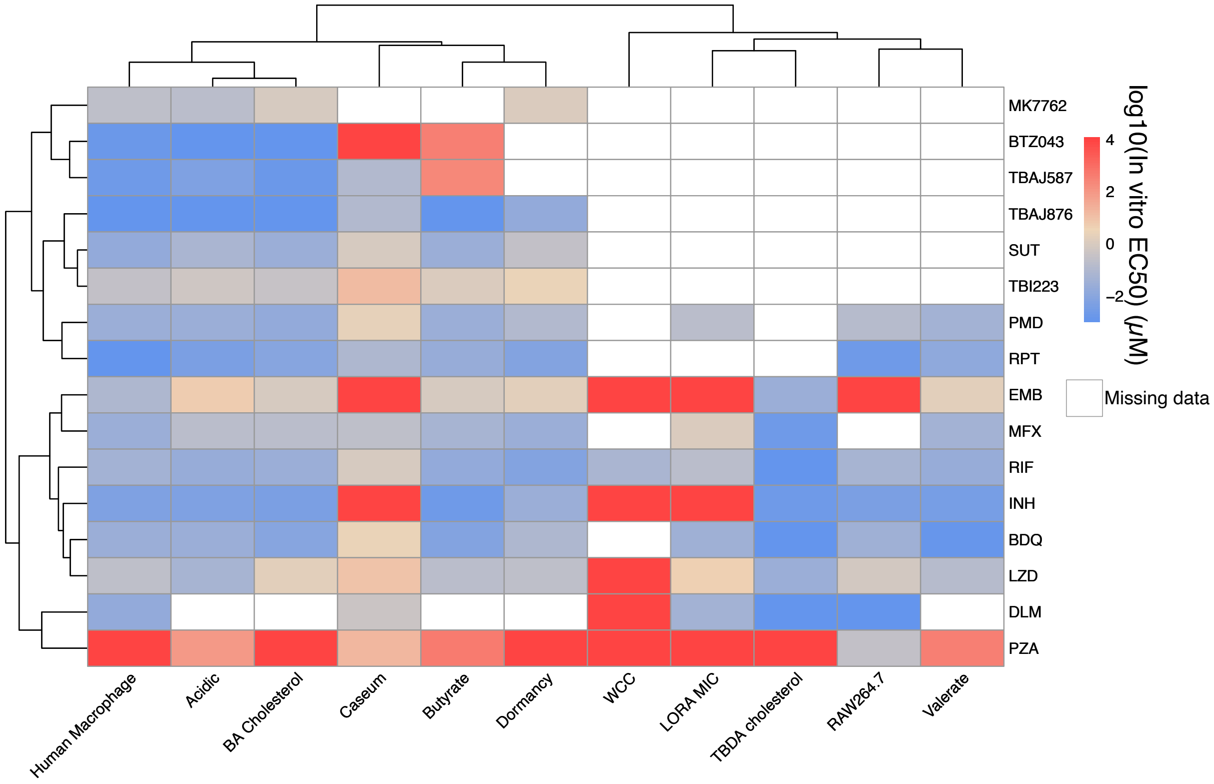
MK7762
BTZ043
TBAJ587
TBAJ876
SUT
TBI223
PMD
RPT
EMB
MFX
RIF
INH
BDQ
LZD
DLM
PZA
Human Macrophage
Acidic
BA Cholesterol
Caseum
Butyrate
Dormancy
WCC
LORA MIC
TBDA cholesterol
RAW264.7
Valerate
log10(In vitro EC50) (μM)
4
2
0
−2
Missing data

(b)

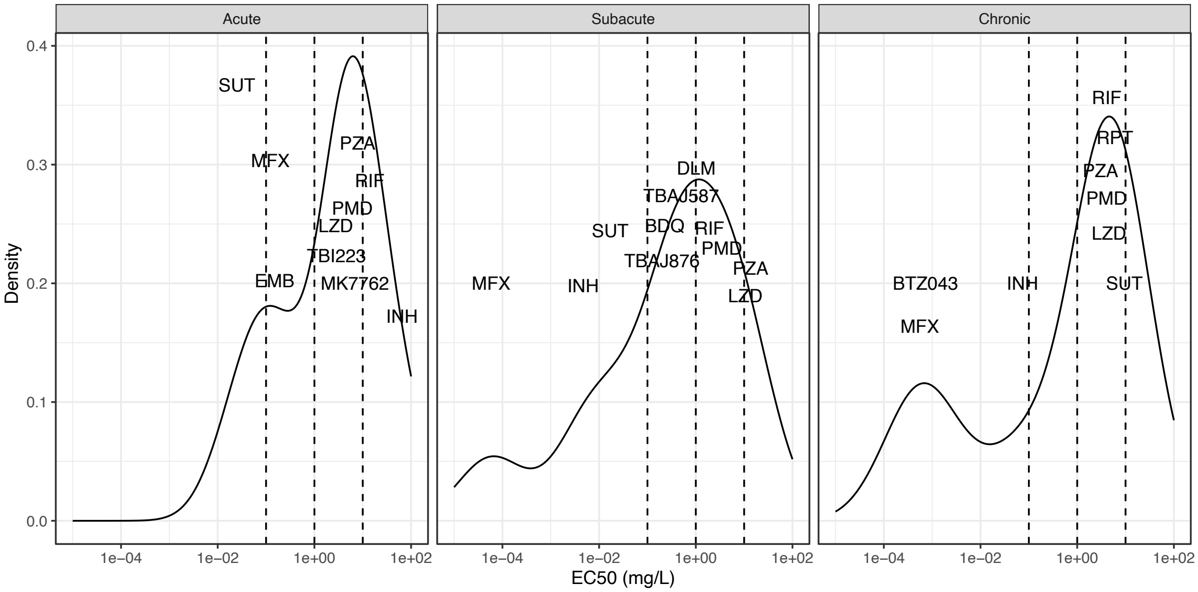
Acute
Subacute
Chronic
Density
0.4
0.3
0.2
0.1
0.0
1e−04
1e−02
1e+00
1e+02
EC50 (mg/L)
SUT
MFX
PZA
RIF
PMD
LZD
TBI223
EMB
MK7762
INH
DLM
TBAJ587
SUT
BDQ
RIF
PMD
TBAJ876
PZA
LZD
MFX
INH
RIF
RPT
PZA
PMD
LZD
BTZ043
INH
SUT
MFX

(c)

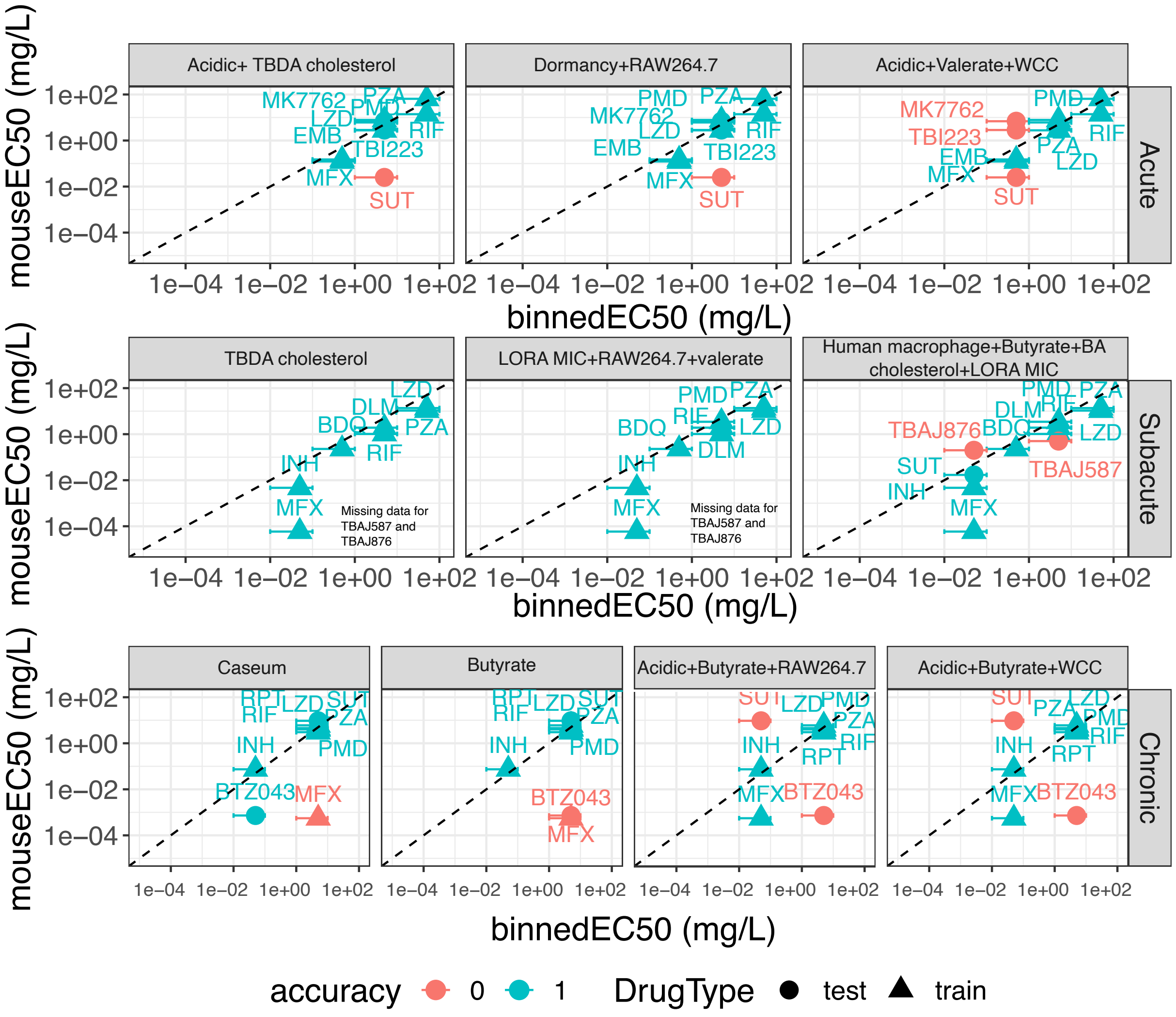
Acidic+ TBDA cholesterol
Dormancy+RAW264.7
Acidic+Valerate+WCC
Acute
TBDA cholesterol
LORA MIC+RAW264.7+valerate
Human macrophage+Butyrate+BA cholesterol+LORA MIC
Subacute
Caseum
Butyrate
Acidic+Butyrate+RAW264.7
Acidic+Butyrate+WCC
Chronic
Missing data for TBAJ587 and TBAJ876
MK7762
PZA
PMD
LZD
RIF
EMB
TBI223
MFX
SUT
BDQ
DLM
INH
TBAJ876
TBAJ587
RPT
BTZ043
mouseEC50 (mg/L)
binnedEC50 (mg/L)
1e−04
1e−02
1e+00
1e+02
accuracy
0
1
DrugType
test
train

(d)

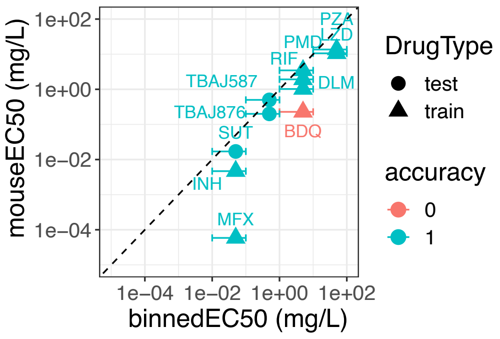
PZA
LZD
PMD
RIF
DLM
TBAJ587
TBAJ876
BDQ
SUT
INH
MFX
mouseEC50 (mg/L)
binnedEC50 (mg/L)
1e−04
1e−02
1e+00
1e+02
DrugType
test
train
accuracy
0
1

Figure 2.5 New TB drugs used as validation with selected in vitro assays could also be predicted with reliable accuracy

(a) Data overview of 6 new TB drugs with the original 10 TB drugs used for testing with selected best performing assays from multinomial classification.
(b) In vivo EC50 distribution into 4 bins per mouse infection model type. Error bars represent the upper and lower bounds of the classification bin.
(c) Selected assay combinations were generalizable to new drugs
(d) Retrained subacute assay containing human macrophage, butyrate, BA cholesterol and LORA MIC had reasonable predictions in both training and testing set using a 80:20 split.

Selected in vitro assay combinations work well in predicting in vivo EC50 of new drugs in acute and chronic mouse infection models

Using the model trained on all 10 drugs, we input newly generated in vitro data from 6 drugs into their respectively trained mouse infection models (Fig 2.5a). TBI223 and MK7762 had in vivo EC_{50} in the acute infection model while TBAJ876 and TBAJ587 had in vivo EC_{50} in the subacute mouse infection model. BTZ043 was tested in a chronic mouse model and SUT had in vivo EC_{50} in all mouse infection models.

The acute combination that worked best was tied between acidic+TBDA cholesterol and dormancy+RAW264.7. As perturbing the media for both acidic and TBDA cholesterol was simpler than doing a co-culture of mouse macrophages with Mtb, acidic+TBDA was the preferred combination (Fig 2.5a). Surprisingly, the caseum assay alone performed much better than both combinations of three in vitro assays in the chronic mouse model. Due to a lack of in vitro assay information for subacute, we were unable to reliably make predictions for new drugs with the exception of our four in vitro assay combination human macrophage, butyrate, BA cholesterol and LORA MIC.

When we retrained the model by compiling all the drugs together and doing a new 80:20 training:test split, we were able to achieve good predictions in the dataset for both training and testing drugs.

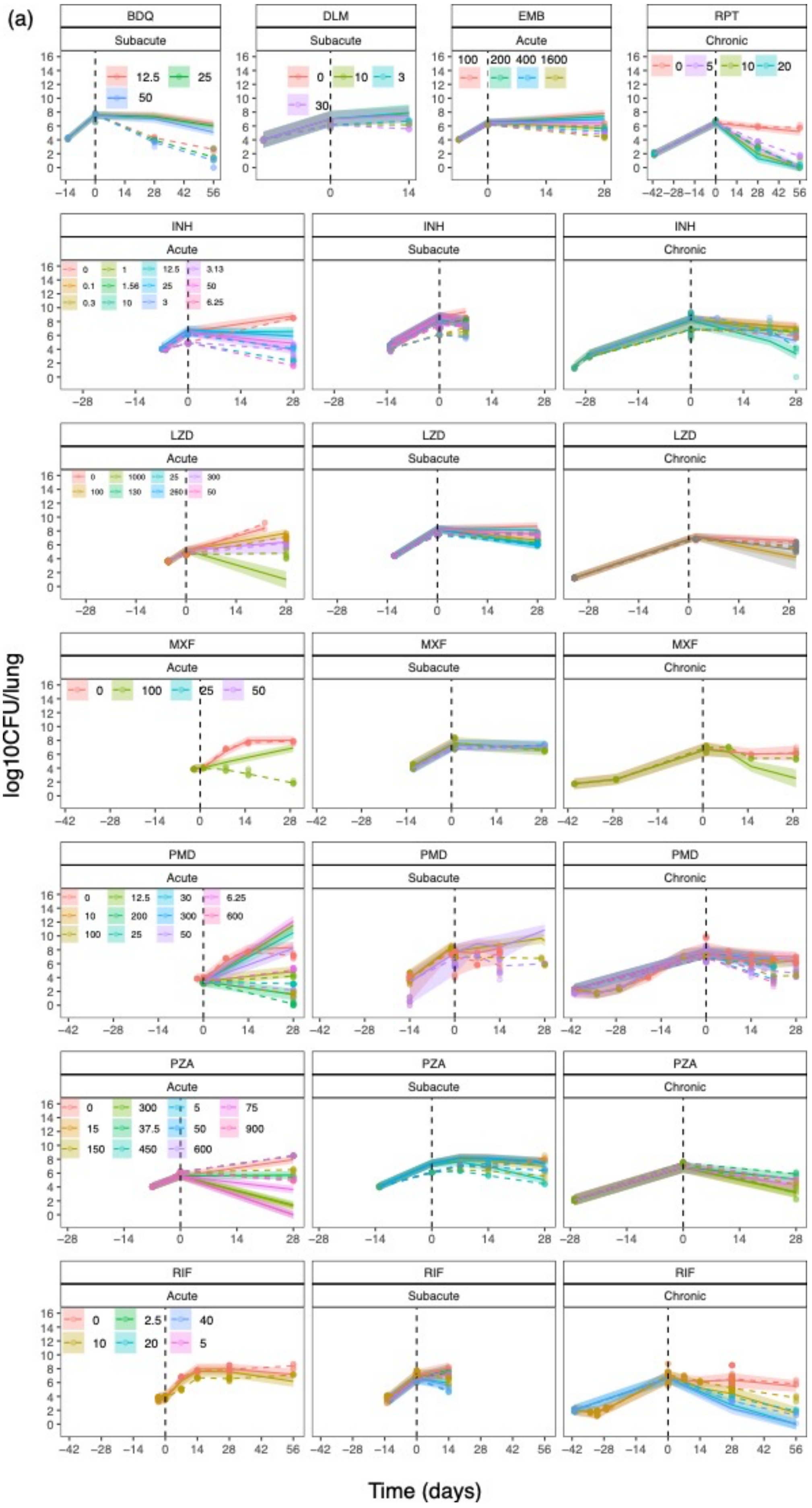
(a)
BDQ
Subacute
12.5
25
50
DLM
Subacute
0
10
3
30
EMB
Acute
100
200
400
1600
RPT
Chronic
0
5
10
20
INH
Acute
0
0.1
0.3
1
1.56
10
12.5
25
3
3.13
50
6.25
INH
Subacute
INH
Chronic
LZD
Acute
0
100
1000
130
25
260
300
50
LZD
Subacute
LZD
Chronic
MXF
Acute
0
100
25
50
MXF
Subacute
MXF
Chronic
PMD
Acute
0
10
100
12.5
200
25
30
300
50
6.25
600
PMD
Subacute
PMD
Chronic
PZA
Acute
0
15
150
300
37.5
450
5
50
600
75
900
PZA
Subacute
PZA
Chronic
RIF
Acute
0
10
2.5
20
40
5
RIF
Subacute
RIF
Chronic
log10CFU/lung
0 2 4 6 8 10 12 14 16
−42 −28 −14 0 14 28 42 56
Time (days)

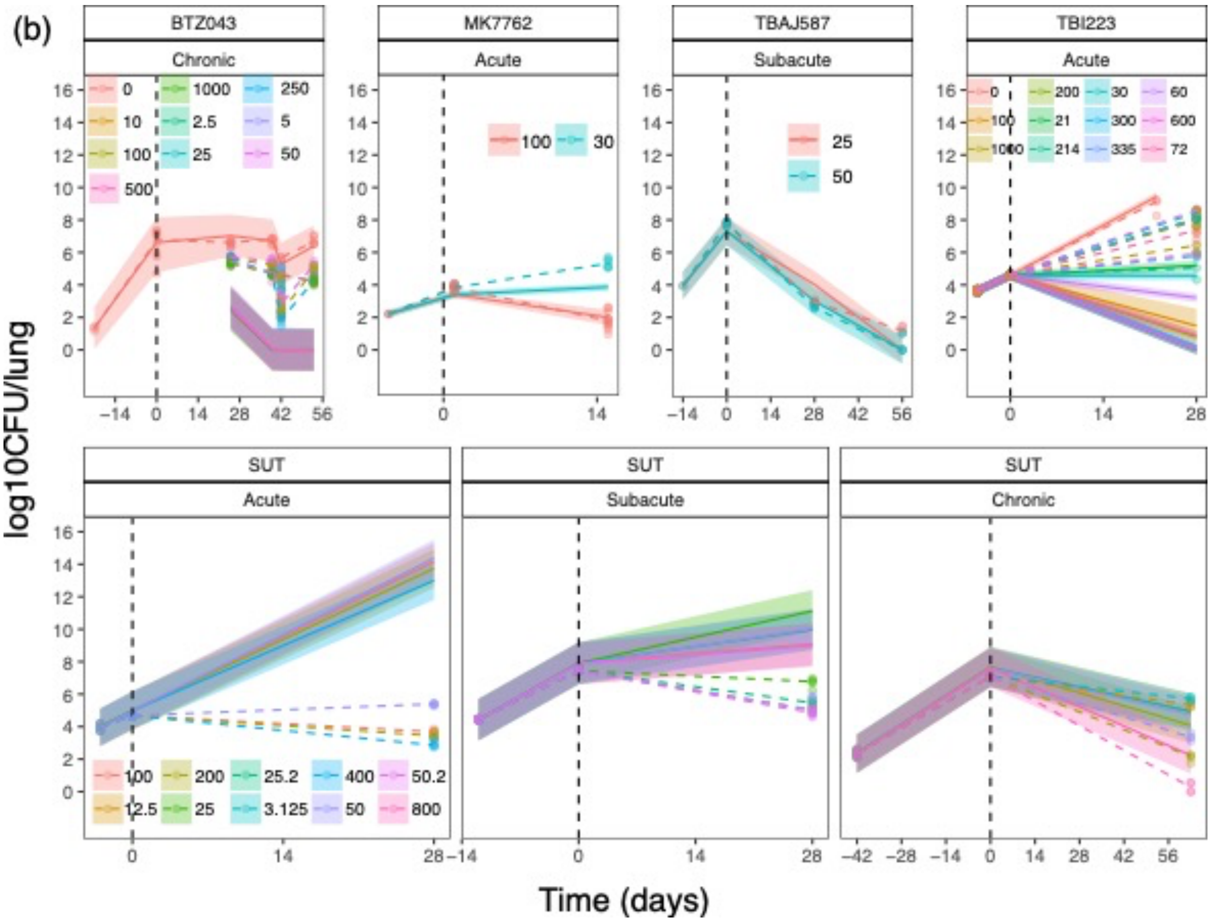

Figure 2.6 Using predicted in vivo EC50, we could approximate mouse CFU drop over time with drug treatment across different mouse infection models.

(a) The original 10 TB drugs used to build the prediction model and their simulated prediction intervals over observed mouse data.
(b) new TB drugs and their simulated prediction intervals from predicted in vivo EC50 over observed mouse data.

Binned EC50 values gave good predictions of mouse CFU profile

After predicting the in vivo EC50 from the best performing combo of in vitro assays, we took the median of each bin the predicted in vivo EC50 was in, along with the median Emax per mouse infection model as the exposure-response relationship in mice in our integrated PK-PD model with bacterial dynamics. This allowed us to predict the outcome in mice over time over a range of drug doses for all 10 training drugs (Fig 2.6a). Interestingly, while we were able to accurately predict the in vivo EC_{50} values for the new drugs, we were not able to capture the mouse CFU profile as successfully as we did with the original 10 drugs, suggesting the new drugs might differ in other exposure response parameters too.

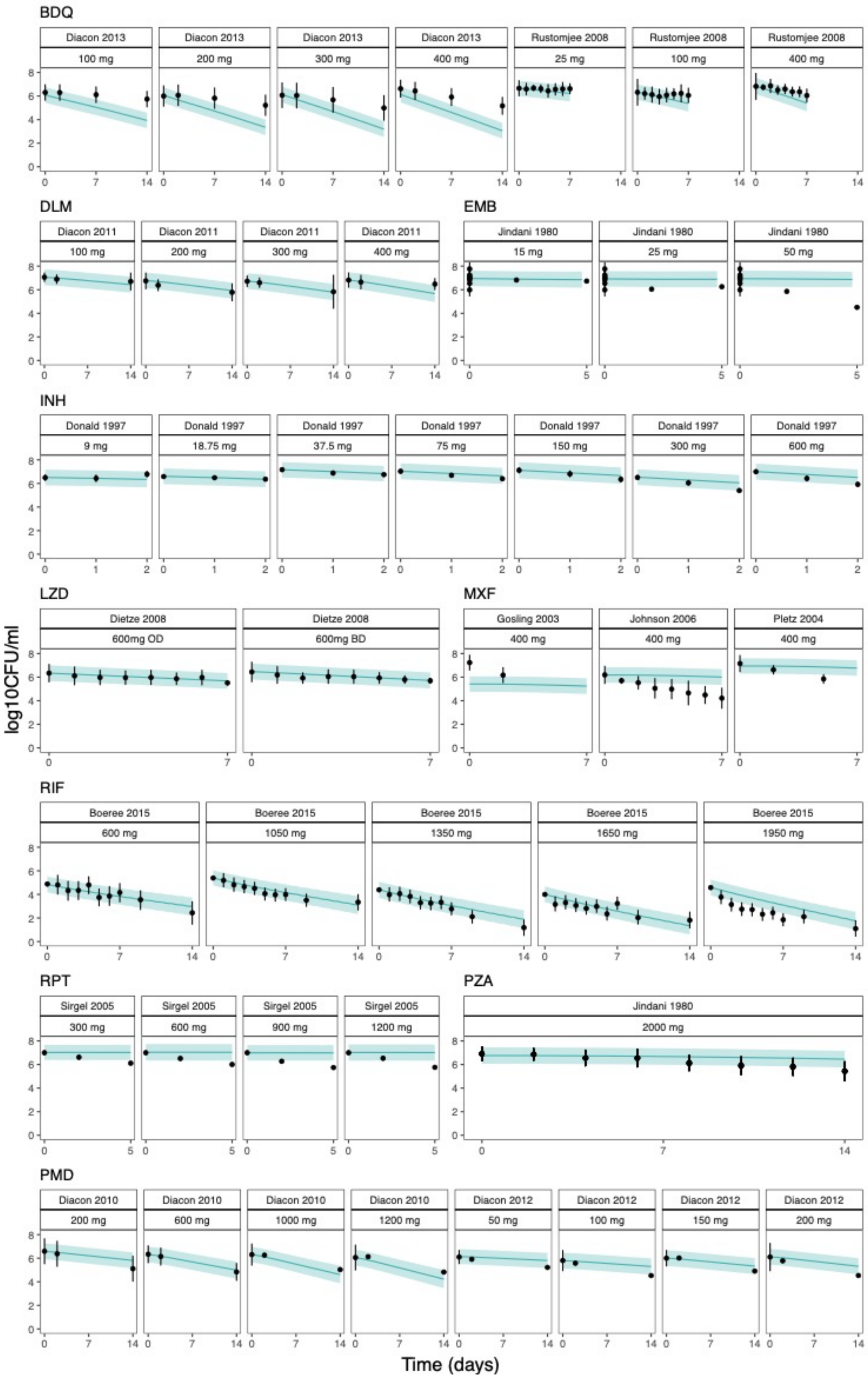

Figure 2.7 Clinical EBA prediction using in vivo exposure response relationships from in vitro data

In vitro to in vivo exposure response predictions for subacute mouse infection models were used with clinical PK models to generate the exposure response relationship. Blue line depicts the median model prediction while the blue ribbon is the 95% prediction interval. Points represent observed clinical data from 14 different studies.

Predicted in vivo exposure response was useful for the prediction of clinical EBA

Similarly, by combining clinical drug exposure with our predicted exposure-response, we were able to get EBA predictions for all 10 drugs over 15 different studies. Our results were largely similar to our preclinical mouse to human predictions, with most predictions overlapping well with the observed clinical data, except for BDQ which had an overpredicted EBA, and RPT, which was likely underpredicted due to a post-antibiotic effect unaccounted for by the current PK-PD model. This demonstrates that exposure-response relationships can be translatable between systems, provided in vivo PK is well described.

Discussion

In vitro assays are the least resource intensive way of screening a drug for efficacy in the drug development pipeline. However, reported in vitro drug potency should be coupled with drug exposure to gain better understanding of a drug's in vivo efficacy. Using our in vivo mouse PK-PD parameters, we have successfully identified which in vitro assays are informative for the prediction of mouse bacterial burden with drug treatment, as well as short-term clinical outcomes. Furthermore, we have demonstrated our predicted exposure-response relationship allows us to predict in vivo EC50 using a set of 3 in vitro assays. This is useful both in designing animal studies as well as suggesting what are reasonable first in human (FIH) doses for clinical testing.

Binned EC50 allows for a robust, reproducible prediction of drugs across datasets

Our initial dataset was limited in that we only had 10 drugs against a total of 15 features split across three different mouse infection models. We thus employed LOOCV as our method of cross-validation instead of the traditional 80:20 training to testing ratio. Trying to predict in vivo EC_{50} as a continuous variable using multiple linear regression led to large amounts of model overfitting in the training set, but very poor predictions in our left out testing drug. Binning the in vivo EC50 into bins, while less accurate, still provided a good estimate of the in vivo EC50, while allowing the model to be more robust to make reliable predictions of the left-out testing drug. The median of the bin also provided a good estimate for the overall exposure-response as seen with the prediction of mouse CFU burden with drug treatment overlapping well with observed experimental data.

While initial clustering and data exploration was done in µM, we decided to do the binning and predictions of EC50 in mg/L as that is the concentration that is commonly reported for PK studies and we wanted to be as consistent as possible with those models. As the main driver of the drug's effect is its exposure characterized as mg/L over time, rather than its potency directly, the predictions in mg/L are more translatable for directly adding into a PK-PD model without additional unit conversions.

Four or less in vitro assays were required for the robust prediction of in vivo EC50 in mice

Due to high correlation between the in vitro assays, it was no surprise that a smaller set of in vitro assays would be representative of the various TB pathophysiology states. With TB pathophysiology being extremely heterogeneous, both acute and subacute mouse infection models required more than one assay to have reliable prediction of in vivo EC_{50}, suggesting different assays describing different biological niches were required for in vivo EC50 prediction. Interestingly, the chronic mouse infection model was well described by the caseum assay alone despite Balb/c mice not forming necrotic lesions. It is possible that after the initial inoculation, the bacteria have reached a more steady state equilibrium, thus allowing for a single assay to reflect in vivo drug potency well.

Insufficient data in the low in vivo EC50 bin of the subacute infection model led to initial poor predictions

Initially, the only drug present in the low bin of the subacute infection model was BDQ. As TBAJ876 and TBAJ587 both have in vivo EC50 in the low bin too, the model might not have had sufficient information to make a good classification. Upon compiling both old and new drugs and retraining the dataset, we were able to achieve much better predictions.

Limitations and future directions

Due to data availability, our dataset was small and biased toward drugs that had already been approved or are in clinical development for TB. This was disadvantageous in being able to understand the significance and weights of each assay within the multinomial regression as our sample size was too small to have significant p-values despite the good accuracy. Having more drugs to validate the pipeline, including drugs that did not make it into in vivo testing would be useful to test the robustness of the model to help aid decisions on the best compounds to move forward. Furthermore, this study is currently limited to only single drugs and short-term EBA. Further work is on going to predict the efficacy of drug combinations.

Conclusion

Using our integrated mouse PK-PD model with bacterial dynamics, we were able to reliably measure in vivo EC50 from mouse infection models across 3 different infection loads and incubation times. This allowed us to use in vivo EC50 as a standard to compare against reported in vitro assay potencies and thus find which assays were most informative for further drug development. Despite the limitations of a small dataset, we have successfully created a pipeline that allows us to predict exposure responses from in vitro studies to in vivo studies. This is a novel piece of work that shows how we can use PK-PD concepts to further help us translate our in vitro results to predict in vivo outcomes both in animal and clinical studies.

References

1. Global Tuberculosis Report 2022. https://www.who.int/teams/global-tuberculosis-programme/tb-reports/global-tuberculosis-report-2022.
2. Nahid, P. *et al.* Executive Summary: Official American Thoracic Society/Centers for Disease Control and Prevention/Infectious Diseases Society of America Clinical Practice Guidelines: Treatment of Drug-Susceptible Tuberculosis. *Clin. Infect. Dis.* **63**, 853–867 (2016).
3. Vernon, A., Fielding, K., Savic, R., Dodd, L. & Nahid, P. The importance of adherence in tuberculosis treatment clinical trials and its relevance in explanatory and pragmatic trials. *PLoS Med.* **16**, e1002884 (2019).
4. Franzblau, S. G. *et al.* Rapid, low-technology MIC determination with clinical Mycobacterium tuberculosis isolates by using the microplate Alamar Blue assay. *J. Clin. Microbiol.* **36**, 362–366 (1998).
5. Connolly, L. E., Edelstein, P. H. & Ramakrishnan, L. Why is long-term therapy required to cure tuberculosis? *PLoS Med.* **4**, e120 (2007).
6. Zhang, Y., Yew, W. W. & Barer, M. R. Targeting persisters for tuberculosis control. *Antimicrob. Agents Chemother.* **56**, 2223–2230 (2012).
7. Ernest, J. P. *et al.* Translational predictions of phase 2a first-in-patient efficacy studies for antituberculosis drugs. *bioRxiv* 2023.01.18.524608 (2023) doi:10.1101/2023.01.18.524608.

Supplementary figures

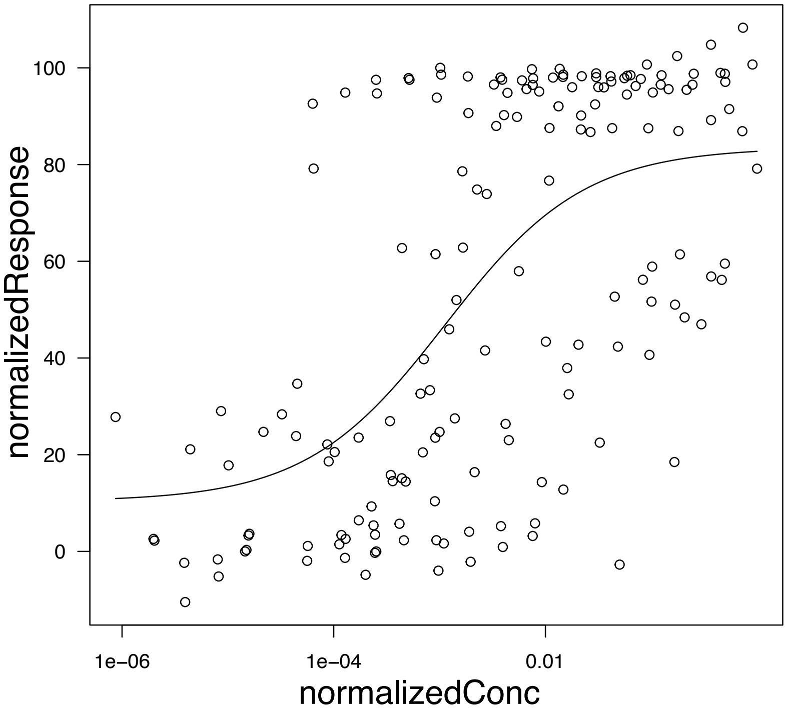

SFigure 2.1 A log logistic regression with hill coefficient of 1 was sufficient to fit all the data points.

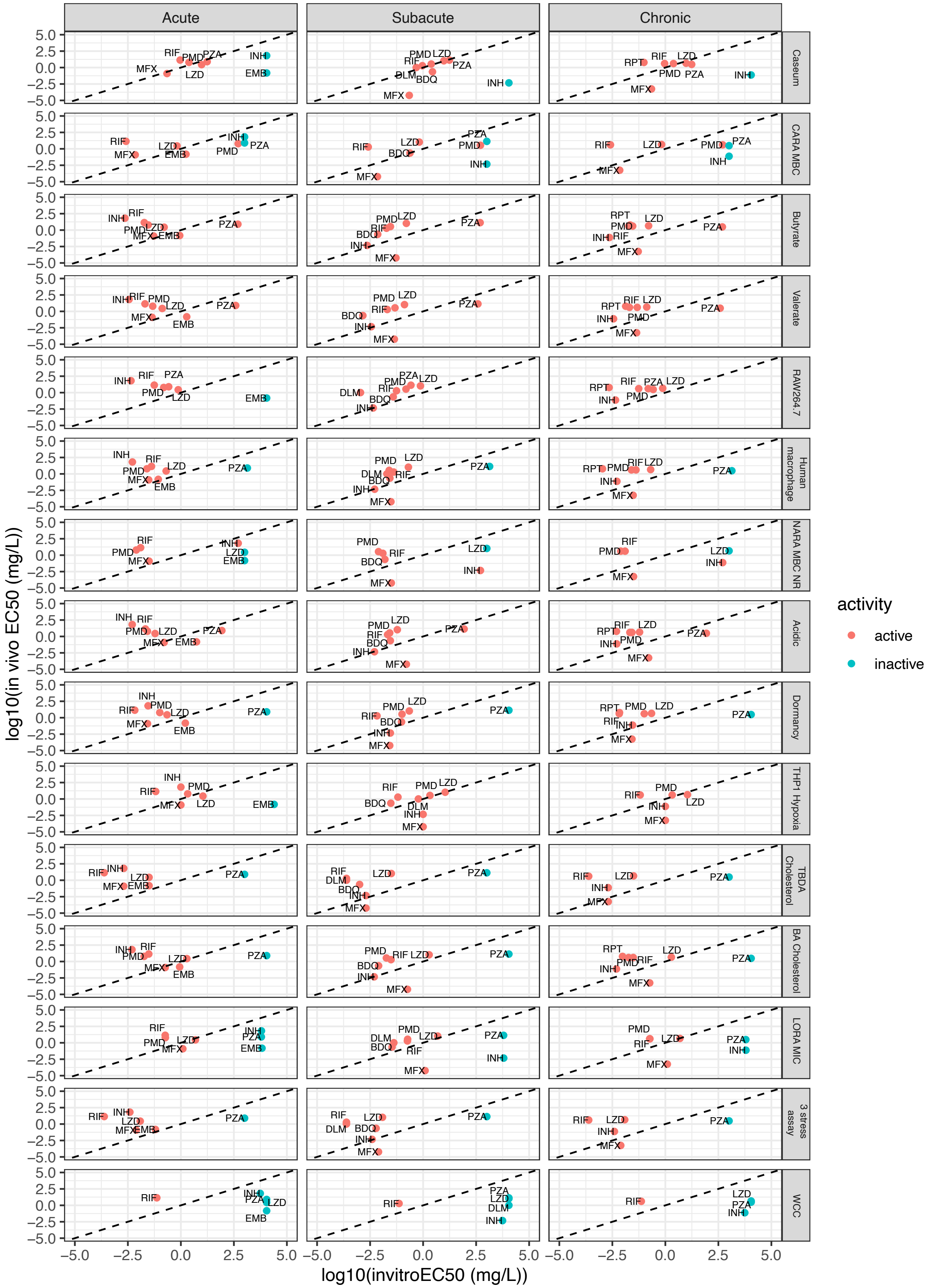
Acute
Subacute
Chronic
Caseum
CARA MBC
Butyrate
Valerate
RAW264.7
Human macrophage
NARA MBC NR
Acidic
Dormancy
THP1 Hypoxia
TBDA Cholesterol
BA Cholesterol
LORA MIC
3 stress assay
WCC
log10(in vivo EC50 (mg/L))
log10(invitroEC50 (mg/L))
−5.0
−2.5
0.0
2.5
5.0
activity
active
inactive
INH
RIF
PZA
EMB
MFX
LZD
PMD
BDQ
DLM
RPT

SFigure 2.2 Correlation plot of in vitro EC50 to in vivo EC50 by in vitro assay across all 3 mouse infection models.

(a)

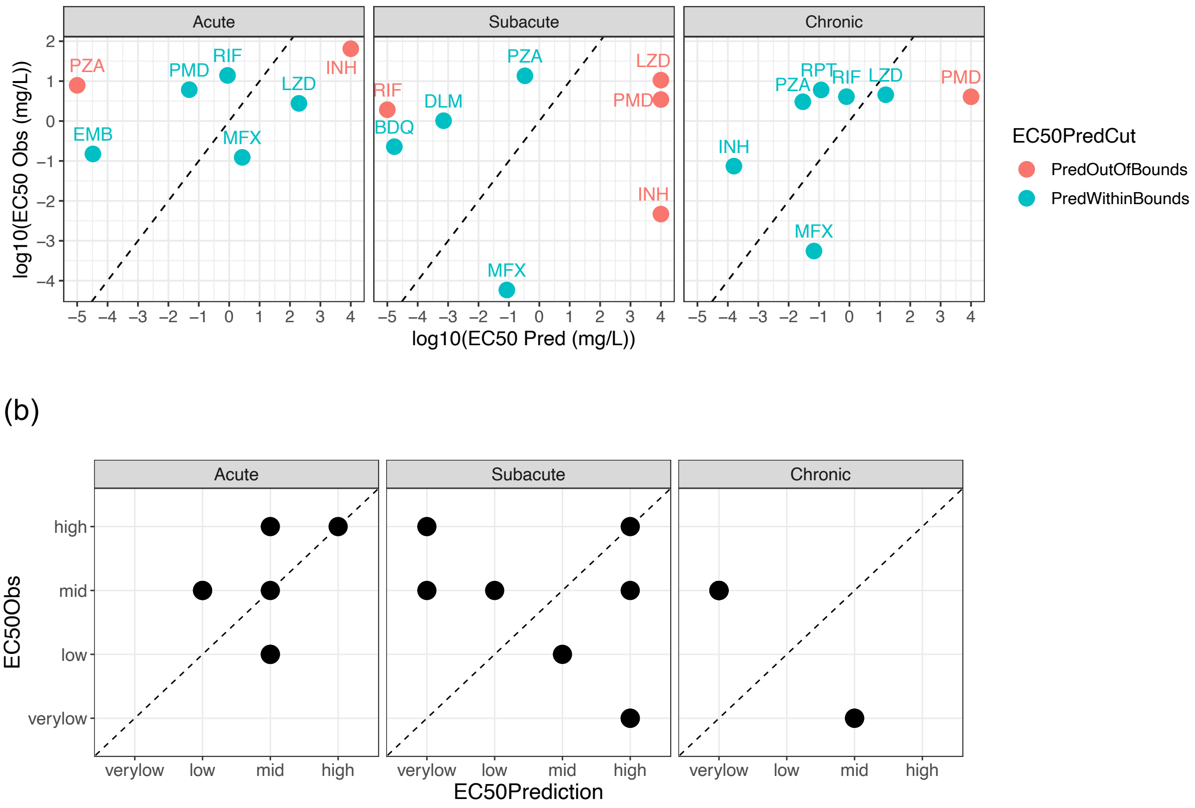

SFigure 2.3 Using all 15 selected features led to poor prediction accuracy.

Leave one out drug cross validation prediction of left one out drug in vivo EC50 using (a) multivariate regression (b) multinomial regression both had over fitted models with the training dataset and were not able to achieve good accuracy with the left one out drug.

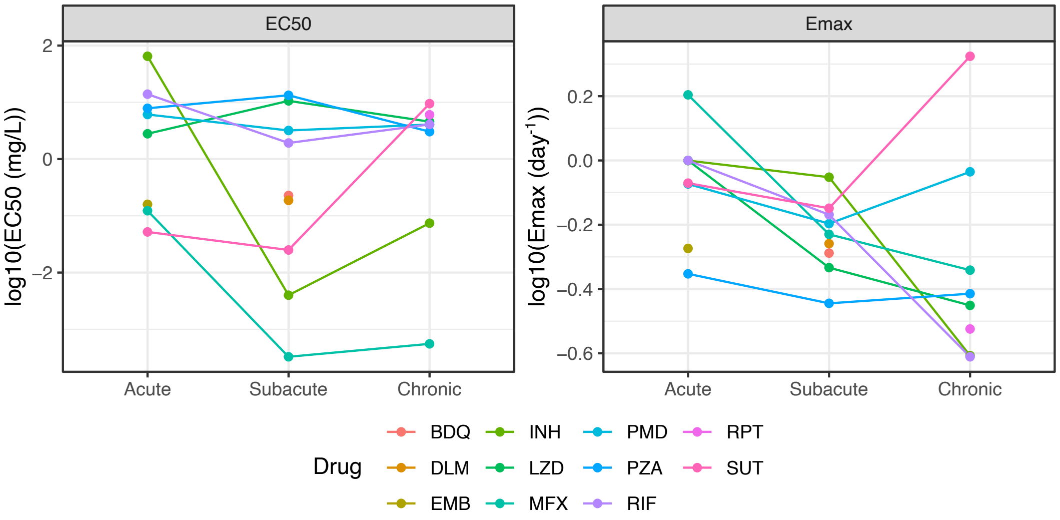

SFigure 2.4 In vivo Emax and EC50 trends across mouse infection models

Emax shows a general downward trend with lower bacterial inoculation and longer incubation time while EC50 does not hold a clear trend against mouse infection model. The median Emax of each infection model was thus used for mouse PKPD simulations along with the predicted in vivo EC50 from in vitro assays.

Chapter 3 The human and mouse gut microbiomes modulate host hepatic CYP3A4 enzyme activity

Abstract

Drug clearance is highly dependent on CYP abundance and activity. However, significant interindividual variation in major liver enzyme CYP3A of up to 30- to 40-fold variation exists. Genetic polymorphisms alone cannot account for this variation. Recent evidence suggests the gut microbiome can modulate CYP expression and activity. Hence, we aim to elucidate the functional consequences and mechanisms of the gut microbiome's modulation of CYP3A4 activity. We compared midazolam's rate of elimination between conventionally-raised (CONVR) mice against germ-free (GF) mice and found that GF mice had a higher rate of elimination despite a lower expression of hepatic Cyp3a11, the mouse ortholog of human CYP3A4, compared to CONVR mice. Similarly, mice colonized with a human (HUMD) microbiome displayed an increased Cyp3a11 (ortholog of human CYP3A4) expression but no significant change in the rate of midazolam elimination. The decrease in CYP3A4 expression and activity was also observed with the human liver cell line HepaRG. We then characterized the inhibitor using microsomal assays which revealed the inhibitor had sphingolipid characteristics. We further observed decreased binding affinity (K_m) of liver microsomes and decreased membrane fluidity in CONVD, HUMD, and CONVR mice compared to GF mice. This supported our hypothesis that gut microbial sphingolipids influenced enzyme activity by altering membrane fluidity. Lastly, we incubated four unique human stool water samples with HepaRG, which reduced CYP3A4 clinical index substrate, midazolam's clearance to differing extents, suggesting the microbiome may contribute to interindividual variation in drug clearance. Our findings demonstrate that both human and mouse microbiomes are capable of inducing CYP3A4, but also inhibiting its function, potentially

via an alteration in membrane fluidity. With both induction and inhibition capabilities, the gut microbiome has the potential to influence interindividual variation in CYP3A4, which the *in vitro* HepaRG assay demonstrates. Characterizing the unique gut microbiome of an individual may thus be the next key in helping us to predict CYP3A4 mediated drug clearance more effectively.

Introduction

CYP3A4 is a major hepatic drug metabolizing enzyme with large interindividual variation

Nearly 75% of marketed drugs are acted upon by CYPs, with ~50% of those metabolized by CYP3A4 [1]. Differences in CYP3A4 activity have broad consequences for drug efficacy and toxicity [2,3]; decreased CYP3A4 activity can lead to severe adverse events, while increased CYP3A4 activity can lead to poor therapeutic efficacy.

CYP3A4 has great variability, 30- to 40-fold at basal levels [4]. Despite multiple *CYP3A4* polymorphisms, there has been no clear genetic association to account for all the variation in CYP3A4 function [5].

The murine gut microbiome influences Cyp expression in mice

Multiple studies have characterized the effect of the gut microbiome by comparing germ-free (GF) mice against conventionally raised (CONVR), or conventionalized (CONVD) mice[6–10]. All have concluded that having a microbiome induces Cyp3a11 expression in mice, as measured via RNA-seq, qPCR, or a mouse liver microsomal assay. Furthermore, we know that the microbiome has diverse metabolic capabilities and can produce a large number of small molecules, some of which are biologically active and influence CYP activity[11]. The gut microbiome could thus help to explain CYP3A4 interindividual variation.

The effect of the human microbiome on CYP expression has not been well characterized

Humans and mice share approximately 85% mRNA similarity[12] and mouse microbiomes are largely different from human microbiomes[13]. Studying the effect of the human microbiome in both *in vivo* gnotobiotic mouse models as well as *in vitro* human cell lines would thus make these findings more translational for clinical use.

Furthermore, pharmacokinetic (PK) experiments for drugs proposed to be influenced by the microbiome have been done mostly via oral administration[9,14,15], which leads to a PK profile confounded with absorption parameters[16,17], another area the microbiome is reported to influence. Administration of intravenous (IV) drugs will thus allow for a clearer picture in understanding hepatic drug metabolism as we can measure drug clearance directly by bypassing the drug absorption process[16].

Our study thus aims to characterize the functional consequences of gut microbial colonization in both human and mouse models of hepatic clearance, as well as the potential mechanisms by which this can occur.

Employing drug-drug interaction tools to study gut microbe drug interactions

To understand the gut microbiome's effect on drug metabolism in a rigorous and well-validated manner, we adapted most of our methods from the Food and Drug Administration’s drug-drug interaction guidance[2]. We first performed a total RNA-seq analysis on GF, humanized (HUMD), CONVD, and CONVR mice livers to understand the broad impact of colonization on hepatic gene expression. This was followed by pharmacokinetic studies in mice and mechanistic studies in both mouse and human *in vitro* systems.

Functional consequences of gut microbial colonization were characterized by administering midazolam, an FDA clinical index Cyp3a11 substrate, via IV tail vein administration to either GF, HUMD, or CONVR mouse models and measuring midazolam's rate of elimination and systemic exposure over time.

After, we used HepaRG cells, a well-validated human hepatocyte cell line, to study both inhibition and induction capabilities of the microbiome on human hepatocytes. Lastly, mouse microsomes derived from GF or colonized mice were used to understand the mechanism of action.

Materials

Table 3.1 Reagents used

Reagent	**Source**	**Identifier**
Stool water fractions and portal vein blood reagents		
MilliQ Water	Filtered in-house	
Heparin Sodium Crude	Sigma-Aldrich	SIAL-H5515-25KU
Sodium Chloride, NaCl, Molecular/Proteomic Grade	Fisher Scientific	60-037
0.22 µm syringe filter	VWR International	28145-501
10 kDa centrifugal filters	Millipore Sigma	UFC510024
Chloroform	Fisher Scientific	288306-1L
Methanol	Sigma-Aldrich	34860-4X4L-R
Methyl-tertbutylether (MTBE)	Fisher Scientific	177040010
Acetonitrile	Fisher Scientific	34998
Nitrogen gas industrial grade	UCSF logistics	13515105
Mild Alkaline hydrolysis		
Potassium hydroxide (KOH)	Fisher Scientific	LC193701
Hydrochloric acid	Fisher Scientific	258148-4L
Methanol	Sigma-Aldrich	34860-4X4L-R

Reagent	Source	Identifier
HepaRG cell culture, maintenance and differentiation		
HPR101 proliferative state HepaRG cells	Biopredic International	HPR101
Fetal Bovine Serum, qualified, heat inactivated	Gibco	10438026
William's E Medium, no glutamine	LifeTechnologies Corporation	12551032
Penicillin-Streptomycin (10,000 U/mL)	LifeTechnologies Corporation	15140122
GlutaMAX™ Supplement	Gibco	35050061
Insulin from bovine pancreas	MilliporeSigma	I0516-5ML
Dimethyl sulfoxide, ReagentPlus®, ≥99.5%	Sigma-Aldrich	D5879-100ML
Hydrocortisone	Cayman chemical	20739
Rifampicin	Cayman chemical	14423
Dulbecco's Phosphate-Buffered Saline	Corning	21-031-CV

Reagent	**Source**	**Identifier**
HepaRG activity assays		
CYP3A4 P450-Glo™ Assays with Luciferin-IPA	Promega	V9002
Midazolam Hydrochloride USP reference standard	Sigma-Aldrich	1443602
Acetonitrile	Fisher Scientific	34998
Alamar blue	Avantor	BUF012A
CyQUANT™ LDH Cytotoxicity Assay Kit	Thermo Scientific	C20301
CellTiter 96® Non-Radioactive Cell Proliferation Assay (MTT)	Promega	G4000
Rifampicin	Cayman chemical	14423
Microsome preparation, quantification and activity		
Sucrose, Ultrapure Bioreagent, for Density Gradient Centrifugation	Fisher Scientific	02-004-331
Protease Inhibitor Cocktail EDTA Free	Abcam	ab270055
Pierce™ BCA Protein Assay Kit	Thermo Fisher Scientific	23225
Mouse Cytochrome P450 3A4 ELISA Kit	Abclonal	RK02730
Benzyloxy resorufin (BzRes)	Cayman chemical	18077
NADPH Regeneration System A and B	Promega	V9510
Tween80	Fisher Scientific	RES3063T-A103
Midazolam Hydrochloride USP reference standard	Sigma-Aldrich	1443602

Reagent	Source	Identifier
Mouse in vivo IV midazolam clearance		
Midazolam 25 mg/5 mL IV injection	Covetrus NA	72622
Sodium citrate tribasic dihydrate	Sigma-Aldrich	C3434-250G
Innovative Med Tech Plastic Capillary Tubes 20 µL	Innovative Med Tech 100020	22757115
Midazolam LC/MS/MS analysis		
Midazolam Hydrochloride USP reference standard	Sigma-Aldrich	1443602
1-OH midazolam	Cayman chemical	10385
d4-midazolam	Cayman chemical	20199
QTRAP 6500 LC-MS/MS System	Sciex	
Synergi™ 4 µm Fusion-RP 80 Å, LC Column 50 x 2 mm, Ea	Phenomenex	00B-4424-B0
Shimadzu Nexera X2 HPLC	Shimadzu	

Reagent	Source	Identifier
Targeted sphingolipid panel		
QTRAP 6500 LC-MS/MS System	Sciex	
Synergi™ 4 µm Fusion-RP 80 Å, LC Column 50 x 2 mm, Ea	Phenomenex	00B-4424-B0
Shimadzu Nexera X2 HPLC	Shimadzu	
Sphingolipid activity assay in HepaRG cells		
D-erythro-Sphinganine	Cayman chemical	C835A97
Sphingosine-1-phosphate	Cayman chemical	C789A42
N-myristoyl-D-sphinganine	MilliporeSigma	80760

Reagent	**Source**	**Identifier**
RNA extraction and library preparation		
2-Mercaptoethanol	Bio-Rad	1610710
PureLink™ RNA Mini Kit	Thermo Fisher Scientific	12183018A
TURBO™ DNase (2 U/μL)	Invitrogen	AM2238
RNAClean XP	Beckman Coulter Life Sciences	A66514
Agilent RNA 6000 Nano Kit	Agilent	5067-1511
NEBNext® rRNA Depletion Kit v2 (Human/Mouse/Rat)	New England BioLabs	E7400X
NEBNext® Ultra™ II Directional RNA Library Prep Kit for Illumina	New England BioLabs	E7760L
NEBNext® Multiplex Oligos for Illumina® (Index Primers Set 1 and 2)	New England BioLabs	E6442S, E6440S
Agilent DNA 1000 Kit	Agilent	5067-1504

Reagent	**Source**	**Identifier**
16S and metagenomic sequencing		
ZR-96 BashingBead Lysis Rack	Zymo Research	S6012-50
ZymoBIOMICS 96 MagBead DNA Kit	Zymo Research	D4302
PicoGreen	Quant-It dsDNA, Life Technologies	P11496
SequalPrep Normalization Plate Kit	Invitrogen	A1051001
MinElute PCR Purification Kit	Qiagen	28004
QIAquick Gel Extraction Kit	Qiagen	28706X4
600 cycle MiSeq Reagent Kit	Illumina	MS-102-3003
PXR reporter assay		
Human PXR Reporter Assay System, 1 x 96-well format assays	Indigo biosciences	IB07001

Methods

Stool and cecal water preparation

The protocol for making stool and cecal water was adapted from M.Beaumont et al.[18]. Frozen stool or cecal samples stored at -80°C were partially thawed and a small sample was aliquoted and weighed. For every 100 mg of stool, 1 ml of MQ water was added. A large glass bead was then added and the samples were homogenized in a Biospec minibeadbeater96 for 1 min. Samples were immediately transferred to a refrigerated centrifuge set at 4°C and spun for 15 min at 21130*g*. After the supernatant was collected it was sterile filtered using a 0.22 µm filter. For treatment in HepaRG cells, stool water was diluted in serum-free cell media to 0.5% v/v before being filter-sterilized again and added immediately to cells. Unused stool water was stored at -20°C and thawed at room temperature before use.

Hepatic portal vein blood collection

To prevent the influence of anesthetics on the liver[18,19], portal vein blood was collected from freshly euthanized mice by opening up the mouse abdominal cavity and adding 600 µL of heparinized saline (50 IU/ml) to it. An aliquot (100 µL) of heparinized saline was first collected from the cavity as a negative control. After, the portal vein was cut and the blood collected from within the cavity. The collected blood is then spun at 2000*g*, 4°C for 15 min before plasma is collected and frozen at -80°C.

PXR reporter assay

A Pregnane X receptor (PXR) assay kit from Indigo biosciences was used according to the manufacturer's instructions. Reporter Cells (200 µl) were dispensed into wells of the assay plate and preincubated for 4-6 h. Following the pre-incubation period, culture media was discarded and 200 µl/well of the prepared 1X-concentration treatment media were added. Following 22-24 h incubation, treatment media was discarded, and Luciferase Detection Reagent was added. The intensity of light emission (in units of 'Relative Light Units'; RLU) from each assay well was quantified using a plate-reading luminometer.

Inhibitor size selection

Stool water was spun down in 10 kDa centrifugal filters for 30 min at 14000*g* at room temperature, per the manufacturer's protocol recommendations. To collect the fraction > 10 kDa, the filter was turned upside down and respun at 1000*g* for 2 min.

Methyl-tert butyl ether (MTBE)/acetonitrile (ACN) extraction

As a general extraction method to desalt and deproteinate stool water, a 50/50 solution of MTBE and ACN was used. MTBE/ACN (1200 µL) was added to 300 µL of stool water and vortexed on high for 2 h. The samples were then centrifuged at 4°C for 15 min at 2000*g*, separating them into a polar bottom phase and a nonpolar top phase. Precipitate at the bottom of the tube was discarded. All layers were then separated and evaporated to dryness using a constant stream of N_2 gas at 10 psi for 1 h at room temperature. The individual layers were reconstituted in a final volume of 300 µL MQ water.

Folch's method for lipid extraction

A two-step Folch's method optimized for bacterial lipid extraction[20] was used to fractionate stool water. First, 800 µL of chloroform and 400 µL of methanol were added to 300 µL stool water (8:4:3 chloroform/methanol/water) and vortexed on high for 2 h. The samples were then centrifuged at 4°C for 15 min at 2000*g*. The mixture separates into 3 layers, a top methanol/water layer, a middle precipitate layer, and a chloroform layer at the bottom. The top methanol/water layer was saved in a fresh tube, and 0.9% NaCl was added to the remaining layers. The mixture was then vortexed again briefly and spun down. All layers were then separated and evaporated to dryness using a constant stream of N_2 gas at 10 psi for 1 h at room temperature. The individual layers were reconstituted in a final volume of 300 µL MQ water.

Mild alkaline hydrolysis to test for sphingolipids

Methanol (400 µl) was added to 100 µl of stool water and vortexed for 2 h. The samples were spun down at 4°C, 21100*g* for 15 min and 450 µL of supernatant was collected. The sample was treated with 9 µl of 1 N KOH (final concentration 0.02 N) or 1 N HCl (final concentration 0.02 N) and incubated for 30 min at 37°C [21]. After an equal volume of either 1 N HCl or 1 N KOH was added to neutralize the reaction the samples were evaporated to dryness. Samples were reconstituted in 100 µL of MQ water.

HepaRG cell culture, maintenance, and differentiation

HepaRG cells were purchased from Biopredic international and cultured according to the suggested conditions[22–24]. Growth media consisted of Williams E Media supplemented with 10%

fetal bovine serum, 5 μg/ml insulin , 50μM hydrocortisone, 5 μg/ml penicillin-streptomycin, and 2 mM GlutaMAX™-I. A differentiating media consisted of the same ingredients as the growth media, but with the addition of 1.7% DMSO. Serum-free cell media had the same ingredients as the growth media without the addition of fetal bovine serum. All cell media was sterilized using a 0.22 μm filter before use. All concentrations stated are final concentrations. HepaRG cells were first seeded at $2x10^6$ cells per T75 flask in growth media for 2 weeks and the media changed every 2-3 days before the addition of 0.85% DMSO in growth cell media for 3 days, followed by differentiating media for another 11 days. After, the cells were then seeded at a density of 60 000 cells/well in differentiating media, with media changed every 2-3 days for another 12 days before use.

HepaRG induction experiments for CYP3A4 function

Initially, to screen for CYP3A4 inducers, HepaRG cells were put in DMSO free growth media 48 h before treatment to bring CYP3A4 expression back to a basal state[24]. After, treatments in serum-free cell media were added for 72 h. All treatments were done in quadruplicate. Stool water and its extracts were used at 0.5% v/v, while hepatic portal vein blood was used at 20% v/v. DMSO was kept to a maximum concentration of 0.1% v/v. Cell viability was measured using Alamar blue[25] at 40X dilution and fluorescence was measured at 570/590nm in a plate reader. After, cells were washed in PBS, and 50 μL of serum-free cell media containing CYP3A4glo-luciferin IPA (1:1000 dilution) was added. The cells were incubated for 1 h at 37°C, 5% CO_2, before adding an equal volume of luciferin detection substrate to measure CYP3A4 activity. An aliquot (80 μL) of each reaction per well was then transferred into a white, opaque 96 well plate, and luminescence was read using a plate reader.

HepaRG inhibition experiments for CYP3A4 function

To measure CYP3A4 activity, HepaRG cells were put in DMSO-free growth media 48 h before treatment. Treatments were added along with 0.1 µM rifampicin to induce CYP3A4 activity for 72 h before CYP3A4glo-luciferin IPA was added to measure CYP3A4 activity via luminescence using the same protocol as stated above. Cell viability was measured using the same procedure as stated above.

HepaRG rapid inhibition assay for CYP3A4 function

Similar to the inhibition experiment, HepaRG cells were put in DMSO free growth media 48 h before treatment. The cells were then treated for 72 h with only 0.1 µM rifampicin to induce CYP3A4. The cells were washed with PBS and 50 µL of treatments were added and incubated for 1 h at 37°C, 5% CO_2 along with 5 µl of 4X diluted Alamar blue to check cell viability. Cell viability was measured and then 50 µL of luciferin-IPA substrate (1:1000) in serum-free media was added and the mixture incubated for 1 h at 37°C, 5% CO_2. An equal volume of luciferin detection reagent was added and 160 µL of reaction mixture was transferred to a white 96 well plate and luminescence read on a plate reader. Dose response curves were fitted using log logistic regressions in R to obtain IC_{50} and Hill coefficients[26].

HepaRG intrinsic clearance assay with midazolam

To mimic the closest possible expression to primary hepatocytes, the vehicle was serum-free cell media with 1.7% DMSO for treatment[23]. The protocol was adapted from B.Bonn et al.[27]. The cells were treated with 0.22 µm filtered 0.1% stool water from human donors for 72 h. The cells were then washed and 100 µL of 1 µM midazolam in 1.7% DMSO serum-free cell media was added to each well. At time points (0, 15, 30, 60, 90, 120 and 180 min), the reactions were stopped by taking 80 μl from the respective wells, and lysing the cells by the addition of 160 μL of ACN spiked with 0.1 μM d4-midazolam as an internal standard. Both the cell media and ACN were combined and quenched samples were kept on ice. The collection plate was centrifuged at 3000 rpm for 30 min at 4°C to pellet any remaining proteins before the supernatant was collected and midazolam quantified via LC-MS/MS. Cell viability was measured using the same procedure as stated above.

Dynamic light scattering of stool water and its fractions from organic solvent extractions

Stool water and its extracted fractions from MTB/ACN and Folch's method were tested 0-5% v/v in 0.22 μm filtered PBS in 4-fold dilutions for 8 concentrations. Each sample (30 μL) was loaded into a black, 384 well plate with a clear bottom in quadruplicates. The plate was then read by the DynaPro II Plate Reader DLS (Wyatt Technologies) to characterize our samples for colloid formation. Colloid characteristics such as Auto correlation function (ACF), radius, normalized intensity, and sum of squares were calculated using the DynaPro II software.

Liver microsome preparation

We adapted our microsome preparation protocol from M.Bodero et al[28]. Fresh livers collected from euthanized mice were washed in PBS and flash-frozen in liquid nitrogen before preparation. The frozen livers were weighed and then homogenized using prechilled Dounce homogenizers on ice until homogenous, using 250 mM sucrose with 1% v/v protease inhibitor cocktail as homogenization buffer. A volume of 1 ml of homogenization buffer was added for every 100 mg of liver. The homogenates were then spun at 10,000*g* for 10 min to remove tissue debris, and the supernatant further spun at 20,000*g* for 2 h to pellet microsomes. The microsomes were then resuspended in homogenization buffer and stored at -80°C. Microsome yield was quantified using a Pierce™ BCA Protein Assay Kit for total protein content. Microsomes were then diluted to working concentrations of either 2500 µg/ml or 5000 µg/ml in homogenization buffer and stored at -80°C until use. Microsomes used for mechanism of inhibition studies were made in bulk from GF mice donated by the UCSF gnotobiotic core.

Microsome Cyp3a11 ELISA quantification

Liver microsomal Cyp3a11 content was quantified by diluting working microsome stocks of 5000 µg/ml at 200X dilution in 100 mM phosphate buffered saline (PBS), before quantification using the Mouse Cytochrome P450 3A4 ELISA Kit according to the manufacturer's protocol.

Microsome reversible inhibition assay with stool water

Stool water was tested as a reversible inhibitor using benzyloxy resorufin (BzRes) as the CYP3A4 specific probe substrate[29]. Experiments were performed in 96-well plates and all treatments were carried out in triplicate. BzRes (0, 0.156, 0.3125, 0.625, 1.25 µM) was preincubated at 37°C for 5 min with 100 µg/ml microsomes, NADPH B, and 100 mM potassium phosphate buffer (pH 7.4) with multiple concentrations of stool water (0-5% v/v, 5 concentrations in 2-fold dilutions). The reactions were initiated by the addition of 5 µl NADPH A, yielding a final incubation mixture of 100 µl with 2% ACN (v/v)[30]. Incubation was carried out at 37°C for 30 min before an 80 µl aliquot was removed and quenched with 160 µL of ice-cold ACN. The plate was then read for fluorescence intensity (560/590 nm, excitation/emission), and the appropriate blanks were subtracted from the reads. All subsequent data analysis was done in R. Nonlinear regressions [31] were fitted and K_m and V_{max} parameters were extracted from the curves.

Microsome test for tight binding inhibition

Stool water was tested as a tight binding inhibitor[32] using BzRes as the probe substrate. BzRes was used at a fixed concentration of 20 µM. Experiments were performed in 96-well plates and all assays were carried out in triplicate. Stool water (0-5% v/v, 8 concentrations in 2-fold dilutions), NADPH B, and 100 mM potassium phosphate buffer (pH 7.4) were preincubated at 37°C for 5 min with multiple concentrations of microsomes (50, 100, 200, 400µg/ml). The reactions were initiated by the addition of 5 µl NADPH A, yielding a final incubation mixture of 100 µl with 2% ACN (v/v)[30]. Incubation was carried out at 37°C for 30 min before an 80 µl aliquot was removed and quenched with 80 µL of ice-cold ACN. The plate was then read for fluorescence intensity (560/590 nm, excitation/emission), and the appropriate blanks were subtracted from the reads. All subsequent data analysis was done in R. Nonlinear regressions were fitted and IC_{50} of stool water for each microsome concentration was determined.

Microsome test for time dependent inhibition - BzRes was used as the probe substrate in this experiment. Incubations (n = 3) were conducted in 96-well plates. Primary incubation mixtures comprising either MW water 5% v/v or stool water 5% v/v were preincubated at 37°C for 5 min with microsomes (500 µg/ml) and NADPH B in potassium phosphate buffer (100 mM, pH 7.4). To initiate the enzymatic reaction, either 5 µl NADPH A or 5 µl of potassium phosphate buffer was added to the primary incubation. The final primary incubation mixture volume was 100 µl and contained 2% (v/v) organic solvent[30]. At different preincubation time points (0, 5, 10, 15, 20, 25 and 30 min) after the addition of NADPH A, 10 µl aliquots of the primary incubation were transferred to 90 µl of the secondary incubation containing 20 µM BzRes, the NADPH regenerating system, and 100 mM potassium phosphate buffer (pH 7.4) to yield a 10-fold dilution. The secondary incubation mixtures were incubated at 37°C for 30 min before 80 µl aliquots were removed and quenched with an equal volume of ice-cold ACN. The plate was then read for fluorescence intensity (560/590 nm, excitation/emission), and the appropriate blanks were subtracted from the reads. Linear regressions were fitted and tested for statistical significance in R.

Microsomal Michaelis Menten kinetics with midazolam

To characterize the kinetics of liver microsomes derived from mice with different gut microbial colonization states with their midazolam pharmacokinetic profiles, midazolam was used as a probe substrate[33]. Experiments were performed in 96-well plates and all samples were carried out in triplicate. Midazolam (0, 3.9, 7.8, 15.6, 31.25, 62.5, 125, 250 µM) was preincubated at 37°C for 5 min with NADPH B, 100 mM potassium phosphate buffer (pH 7.4) and microsomes (50 µg/ml) derived from individual mice (GF n=4, CONVD n = 4, CONVR n=4, SPF n=4). The reactions were initiated by the addition of 5 µl NADPH A, yielding a final incubation mixture of 100 µl with 2% ACN (v/v). Incubation was carried out at 37°C for 30 min before an 80 µl aliquot was removed and quenched with 160 µL of ice-cold ACN containing 0.1 µM d4-midazolam (internal standard). The plate was then centrifuged at 4°C, 1500*g* for 30 min and the supernatant was collected for LCMS/MS analysis. Quantification of samples was done using Analyst 1.6.2 software and subsequent analyses were done in R.

Microsome membrane fluidity assay

Membrane fluidity was characterized using a membrane fluidity kit (Abcam). Microsomes were incubated for 1 h at room temperature protected from light in a labeling solution consisting of 5 µM pyrenedecanoic acid (PDA) and 0.08% v/v pluronic F127 in PBS to a total volume of 100 µL per replicate. Each microsome sample was assayed in triplicate. Unincorporated PDA was removed by the addition of 1000 µL of 250 mM sucrose and centrifuging at 4°C, 21130*g* for 1 h.

The supernatant was then removed and resuspended in PBS, and fluorescence was read at both 400 nm (monomer) and 450 nm(excimer) using the appropriate filter for excitation at 350 nm.

Mouse studies

Mice housing and conditions

All mouse experiments were approved by the University of California San Francisco Institutional Animal Care and Use Committee. Housing conditions are specified (either gnotobiotic or SPF as described below). The mice were housed at temperatures ranging from 19-24°C and humidity ranging from 30-70%. No mice were involved in previous procedures before experiments were performed. The initial gnotobiotic colonization experiments examining gut microbial composition and host gene expression were done in male C57/B6 mice. After we found Cyp3a11 as a top hit, we switched to female Balb/C mice for easier IV administration were used in this study. Female mice were also preferred due to their higher basal expression of Cyp3a11 which would make differences in Cyp3a11 expression and function more evident.

Gnotobiotic mouse studies

Balb/c mice (females ages 10-14 weeks) for midazolam time profile studies or C57/B6 mice (males ages 8-14 weeks) for microsome and gene expression studies were obtained from the University of California, San Francisco (UCSF) Gnotobiotics core facility (gnotobiotics.ucsf.edu) and housed in gnotobiotic Iso positive cages (Tecniplast) for the duration of each experiment (Class Biologically Clean). Mice were colonized via oral gavage with either human stool or mouse cecal samples. In the host gene expression study, mice were colonized for 6 weeks and fecal pellets collected every week to monitor colonization. For harvesting microsomes and midazolam pharmacokinetic experiments, mice were colonized for 2 weeks.

Preparation of inoculation media for complex colonizations in GF mice

Colonization media was prepared using BHI with supplements 0.05% Cysteine-HCl, 1 μg/mL Vitamin K, 5 μg/mL Hemin and 15% glycerol before filter sterilization with a 0.22 μm filter. The colonization media was then equilibrated in an anaerobic chamber for at least 5 days prior to use. For every 1g of either cecal content or human stool sample, 10 ml of colonization media was added. The mixture was then vortexed thoroughly until homogenous and strained with a 100 μm mesh strainer to remove large debris. The resulting inoculum was stored at -80°C and transferred into a BSL2 hood for colonization via oral gavage before the inoculated mice were transferred to techniplast cages. Inoculation media (100 μL) was delivered by oral gavage using a 20-gauge feeding tube with a rounded tip. Animals were monitored carefully over the following 10 min and again the next day for complications of gavage or colonization.

CONVR mouse studies

Balb/c mice (females, ages 10-14 weeks) were ordered from Jackson Labs. The mice were kept in specific pathogen-free facilities until the day of the experiment.

IV Midazolam PK studies

IV midazolam 10 mg/kg was administered to mice via tail vein injection. All experiments were done in biosafety cabinets to ensure the environment remained sterile. Blood was drawn via tail vein into heparinized plastic capillaries, and 20 µL of blood was collected at various time points (15, 30, 60, 120, 180, 360 and 480 min) and added to 60 µL of 0.1 M sodium citrate solution as the anticoagulant. Blood samples were kept on ice and centrifuged at 4°C, 2000*g* for 15min, and the plasma supernatant collected for LC/MS/MS quantification. At the end of the time course, mice were euthanized and their livers, portal vein blood, and cecal samples were collected for further analyses. Due to midazolam's sedative properties, mice were given 1 ml of normal saline via subcutaneous injection to ensure hydration. Samples were extracted by adding 5 µl of plasma to 145 µl of ACN with 50 ng/ml d4-midazolam. Samples were centrifuged at 2000*g* for 30 min at 4°C and supernatant was taken for LC/MS/MS analysis.

Measurement of midazolam and 1-OH midazolam metabolite formation via LC/MS/MS

All samples were analyzed using a Shimadzu Nexera X2 HPLC (Agilent Technologies Inc., Santa Clara, CA, USA) interfaced with the AB SCIEX QTRAP 6500 tandem mass spectrometry (MS/MS) system (AB SCIEX, Framingham, MA, USA). Separation was performed on a Phenomenex Synergi 4µm Fusion-RP 80 A LC column 50X2 mm. The column and sample temperatures were maintained at 25°C and 4°C, respectively. Samples were delivered using an injection volume of 5 µL. The aqueous mobile phase (A) was 0.1% v/v formic acid in milli-Q water whereas the organic mobile phase (B) consisted of 0.1% formic acid v/v in methanol. The gradient program was as follows: The flow rate was set to 0.6 mL/min. A linear gradient was used, with the initial mobile phase consisting of 5% solvent B, which was increased to 95% over a period of 3 min and maintained for 1 min before returning to 5% solvent B, with column equilibration for 1 min between injections. The retention times of midazolam, d4 midazolam, and 1'-hydroxymidazolam were 1.9, 1.9, and 2.1 min respectively. All analyses were performed in ESI positive mode. The MS source conditions were as follows: The optimized MS/MS method for this analysis used the transitions m/z 326→291, m/z 342→324, and m/z 330→295 for midazolam, 1'-hydroxymidazolam, and d4-midazolam, respectively. The collision energy voltages used for midazolam, 1'-hydroxymidazolam, and d4 midazolam were 26, 20, and 26 V, respectively. Parameters that were kept constant for all the analytes were the capillary temperature which was set at 270°C and the vaporizer temperature at 300°C, collision pressure was set to 1.5 mTorr and the sheath gas pressure was 60 arbitrary units and the auxiliary gas pressure was 20 arbitrary units. Chromatographic peak integrations were performed with Analyst software ver. 1.6.2 (Applied Biosystems).

Standard curves for measuring midazolam in vivo in mice over time- Midazolam and 1-OH midazolam were quantified using a standard curve from concentrations of 0, 3.75, 5, 7.5, 15, 25, 50, 125, 250, 500, 1000 and 1500 ng/ml; quality controls of 10, 100 and 750 ng/ml were run in triplicate. Internal standard was 50 ng/ml d4-midazolam. Standard curves were fitted using linear regression, 1/x weighting in Analyst 1.6.2. An acceptable range for quality controls was within ±20% of accuracy from known concentrations. To ensure that the sample concentrations fell within the standard curve, we diluted samples with a predicted high concentration from 180 min and below in MQ water 10X before extraction. Standards were prepared similarly to samples, with 5 µl of blank mouse plasma spiked into 145 µl of ACN containing standard and internal standard.

Standard curves for microsome assays - For microsome assays, only 1-OH midazolam was quantified using a standard curve from concentrations of 0, 0.00625, 0.0125, 0.025, 0.05, 0.1, 0.2, 0.3 and 0.4 µM. Quality controls were run in triplicate at concentrations of 0.02, 0.08, and

0.15 µM. Standards were prepared in a similar method to samples. An acceptable range for quality controls was within ±20% of accuracy from known concentration.

Standard curves for HepaRG intrinsic clearance

For HepaRG intrinsic clearance, only midazolam was quantified with a standard curve from concentrations of 0, 0.03125, 0.0625, 0.125, 0.25, 0.5, 0.75 and 1 µM. Quality controls were run in triplicate at 0.05 and 0.6 µM. An acceptable range for quality controls was within ±20% of accuracy from known concentrations.

Targeted metabolomics using sphingolipid panel - This method was modified in reference to an in-house targeted sphingolipid panel of 35 known sphingolipids from the UCSF Quantitative Metabolite Analysis Center (QMAC). All samples were analyzed using a Shimadzu Nexera X2 HPLC (Agilent Technologies Inc., Santa Clara, CA, USA) interfaced with the AB SCIEX QTRAP 6500 tandem mass spectrometry (MS/MS) system (AB SCIEX, Framingham, MA, USA). Separation was performed on a Synergi 4µMm Fusion-RP 80 A LC column 50X2 mm (Agilent Technologies Inc., Santa Clara, CA, USA). Samples were delivered using an injection volume of 1 µL. The aqueous mobile phase (A) was 0.1% v/v formic acid in milli-Q water whereas the organic mobile phase (B) consisted of 0.1% formic acid v/v in methanol. Mobile phases were delivered at a flow rate of 0.6 mL/min. The gradient program was as follows: A linear gradient was used, with the initial mobile phase consisting of 90% solvent B, which was increased to 100% after 3 min and maintained for 3 min before returning to 90% solvent B, with column equilibration for 2 min between injections. Individual compound MS parameters and retention times are available under supplementary materials.

RNA-seq of mouse liver from complex colonizations - Total RNA was extracted from either flash-frozen or tissue stored in RNA later® using a pure link RNA miniprep kit with 1% v/v beta-mercaptoethanol in lysis buffer. The standard kit protocol was followed and samples were cleaned up with turboDNAse and RNAcleanXP magnetic beads (1.8X beads to sample). RNA quality was then checked using a Bioanalyzer and RNA nano reagents to calculate the RIN scores. Samples with RIN scores <4 were re-extracted or discarded if insufficient sample was left.

Nebnext rRNA depletion kit was used to deplete abundant rRNA reads and total RNA libraries prepared using NEBNext® Ultra™ II Directional RNA Library Prep Kit for Illumina. Samples were indexed with NEBNext® Multiplex Oligos for Illumina® (Index Primers Set 1 and 2). Samples were checked for size and quantified using a bioanalyzer and DNA 1000 reagents before pooling to an even DNA concentration per sample. A preliminary MiSeq run was carried out before a Novaseq S4 2 lane run for a 300 bp library was used for deep sequencing.

Sample reads were demultiplexed before being trimmed and filtered using FastP[34]. Libraries from both lanes were merged and STAR was used to align the reads to host index MM27[35]. After, featureCounts[36] was used to annotate the genes from the aligned reads.

FeatureCount tables were analyzed in R, and samples were visualized using principal component analysis (PCA) and DESeq2[37] for differences between colonization groups. Pathway analyses were carried out using PathFindR[38].

To identify genes regulated by PXR and CAR, we utilized a previously published database from J. Cui et al. which details gene changes in the mouse liver transcriptome using PXR and CAR specific agonists[39].

16S rRNA Sequencing and Analysis

Human stool samples, mouse pellets, and cecal contents were homogenized with bead beating for 5 min (Mini-Beadbeater-96, BioSpec) using the ZR BashingBead lysis matrix containing 0.1 and 0.5 mm beads and the lysis solution provided in the ZymoBIOMICS 96 MagBead DNA Kit. The samples were then centrifuged for 5 min at 3,000 *g* and the supernatant was transferred to 1 mL deep-well plates. The DNA was then purified using the ZymoBIOMICS 96 MagBead DNA Kit according to the manufacturer's instructions.

For human samples, 16S rRNA gene PCR was carried out using GoLay-barcoded 515F/806R primers [40] targeting the V4 region of the 16S rRNA gene according to the methods of the Earth Microbiome Project (earthmicrobiome.org). Amplicons were quantified with PicoGreen and pooled at equimolar concentrations. For other samples, 16S rRNA gene PCR was carried out as per reference protocol and primers [41]. Amplicons were pooled and normalized using the SequalPrep Normalization Plate Kit. For both mouse and human samples, aliquots of the pools were then column (MinElute PCR Purification Kit, Qiagen) and gel purified (QIAquick Gel Extraction Kit, Qiagen). Libraries were then quantified and sequenced with a 600 cycle MiSeq Reagent Kit (250x250; Illumina) with ~15% PhiX.

Sequencing reads were demultiplexed using QIIME before denoising and processing with DADA2[42]. Taxonomy was assigned using the DADA2 implementation of the RDP classifier[43] using the DADA2 formatted training sets for SILVA123 (benjjneb.github.io/dada2/assign.html). A phylogenetic tree was constructed using FastTree [44] with midpoint rooting. Sequence variants were filtered such that they were present in more than one sample with at least a total of 10 reads. The PhILR Euclidean distance was calculated by first carrying out the phylogenetic isometric log ratio transformation (philr, PhILR [44,45]) followed by calculating the Euclidean distance (vegdist, Vegan [46,47]). Principal coordinate analysis (PCoA) was carried out using the pcoa function of APE[46]. ADONIS calculations were carried out (adonis, Vegan) with 999 replications on each distance metric. The Wald test in the DESeq2 package [37,46,47]was used to analyze differential abundances on count data, using features that represented at least 0.05% of total sequencing reads. Centered log2-ratio (CLR) normalized abundances were calculated as Aclr=[log2(A1/ga), log2(A2/ga),… log2(An/ga),], where A is a vector of read counts with a prior of 0.5 added and ga is the geometric mean of all values of A. Time-course analyses were carried out using linear mixed effects models (lmerTest [48]) using mouse as a random effect to account for repeated sampling across time. Corrections for multiple hypothesis testing to false discovery rate (FDR) using the Benjamin-Hochberg method [48,49] were performed where applicable.

Metagenomic Shotgun Sequencing and Analysis - Fecal DNA from human stool, mouse pellets, and cecal samples were isolated as described above. Whole-genome shotgun libraries were prepared using the Nextera XT DNA Library Prep Kit (Illumina). Paired ends of the libraries were sequenced on the Illumina NovaSeq 6000 platform. Raw Illumina reads underwent quality trimming and adaptor removal using FastP[34] and host read removal by mapping to the human genome (GRCh38) with BMTagger[50]. Taxonomic profiling and annotation were performed using Metaphlan 3.0.1[51]**.**

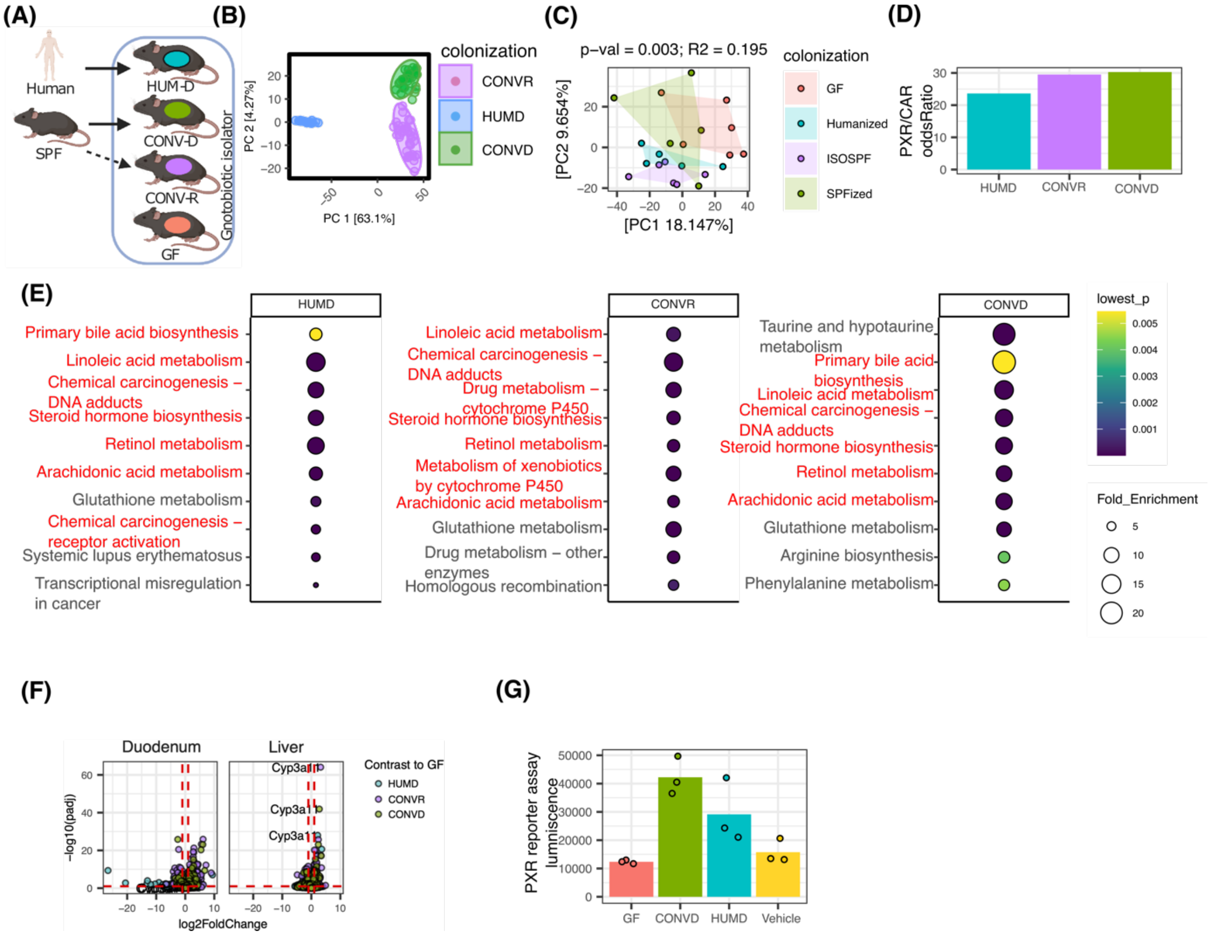

Figure 3.1 Gut microbial colonization with both mouse and human microbiomes impacts drug metabolism pathways in the liver.

(A) Experimental setup for RNA-seq in mice with complex colonizations. Mice were gavaged with either a human stool (HUMD, n = 6) or mouse cecal sample (CONVD, n=6) or kept germ-free (GF, n=6) and housed in a gnotobiotic isolator for 6 weeks prior to sac.

(B) Principal coordinates analysis (PCoA) plot of 16S rRNA sequencing characterizing the uniqueness of each complex microbial community in the colonized mice after 6 weeks of colonization showed each colonization has its own unique microbial community. Oval represents 95% confidence interval.

(C) Principal component analysis (PCA) plot of RNA-seq data in the liver between mice with different colonizations shows colonization results in significantly different transcriptomic profiles between different colonization groups (adonis test, padj < 0.01, R^2 = 0.195).

(D) Odds ratio of the proportion of genes significantly expressed in PXR/CAR regulated genes against the proportion of all significantly expressed genes in the whole mouse genome from differential expression analysis comparisons between colonized and GF mice. The proportion of

significant genes regulated by PXR/CAR was significantly enriched compared to the overall proportion of significant genes. (Chi-squared test, pval < $2.2*10^{-16}$)
(E) Pathway enrichment analysis of the top 10 enriched pathways by fold enrichment shows that the majority of genes that changed significantly between GF and colonized mice are related to Cyps involved in endo- and xenobiotic metabolism. All pathways containing Cyps were highlighted in red text.
(F) Volcano plots of gene expression in colonized mice compared to germ-free (GF) show Cyp3a11 is significantly and highly differentially expressed in all 3 complex colonization groups in the liver but not the intestine.
(G) PXR luminescence reporter assay shows the presence of PXR agonists in cecal water from CONVD and HUMD mice.

GF mice colonized with either human stool (HUMD) or mouse cecal content (CONVD) had unique microbiomes 6 weeks post colonization

To first get a broad overview of the gut microbiome's effect on drug metabolism, we colonized germ-free (GF) mice with a human (HUMD, n = 6) or a mouse microbiome (CONVD, n = 6) for 6 weeks. Uncolonized GF mice and conventionally raised mice (CONVR) were also similarly housed in the gnotobiotic isolator and used as comparisons (Fig 3.1A). 16S rRNA sequencing on mouse pellets collected post 6 weeks of colonization showed 3 distinct complex gut microbial communities (CONVD, CONVR, HUMD) without overlap on a PCoA (Fig 3.1B). CONVR and CONVD notably had differences in gut microbial composition too, despite both being murine sources, likely due to sample handling in preparing the inoculation media for CONVD mice. There was a much larger difference between HUMD and CONVD, being separated mainly by PC1, which was expected as the inoculations came from different species. Notably, when comparing relative abundances between HUMD and CONVD, *Bacteroidetes* stood out as a phyla that had a large number of differences (Supplementary Fig 3.1C). More information on colonization efficiency, gut microbial composition over time and alpha diversity are available in Supplementary Fig 3.1.

Total RNA-seq reveals an enrichment of PXR and CAR related genes in both CONVD and HUMD mice

Livers from these mice were collected and their total RNA extracted and sequenced. Differential expression analysis (DESeq) [37] of RNA-seq data from each of these unique microbiome comparisons (Fig 3.1B) against GF mice showed that there was an enrichment of genes regulated by PXR and CAR [39] (Chi-squared test, p.value < 0.01 for all 3 groups) (Fig 3.1D). PXR and CAR are xenobiotic sensing nuclear receptors that regulate a large number of drug metabolizing enzymes and transporters [52].

Cyp3a11, the mouse ortholog of human CYP3A4 is highly upregulated in the livers of both CONVD and HUMD mice

We also found that across colonizations, endobiotic and drug metabolism pathways involving Cyps were highly enriched in the top 10 pathways using PathFindR [38] (Fig 3.1E). More notably, we found that one of the most significant hits in the dataset was the major hepatic drug metabolizing enzyme, Cyp3a11, the mouse ortholog of human CYP3A4[53] (Fig 3.1F). This finding has previously been reported in several other studies [6–8,10]. A follow up screen using a PXR reporter assay helped us confirm the presence of PXR agonists within cecal water samples of CONVD and HUMD mice (Fig 3.1G) used in the gene expression study (Fig 3.1A).

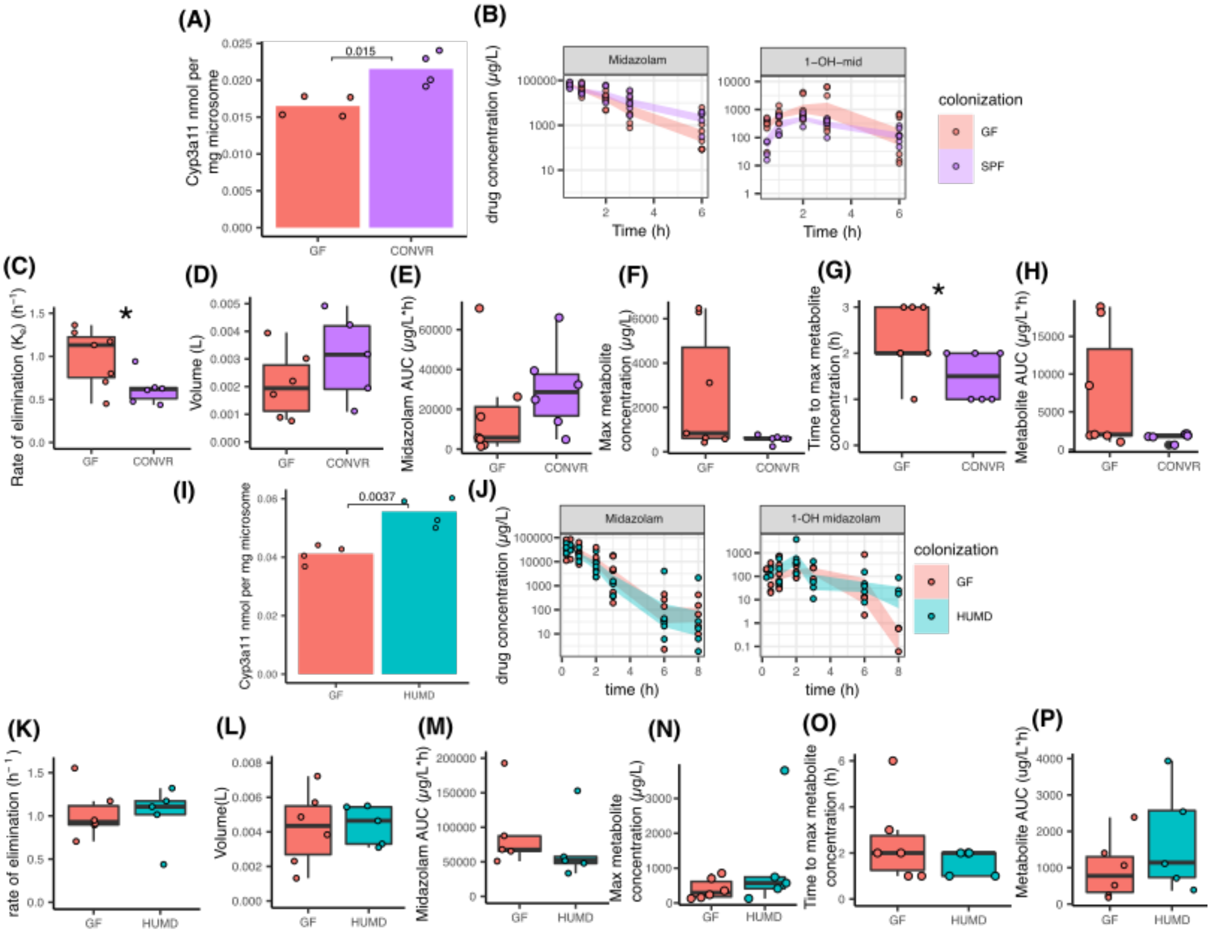

Figure 3.2 Gut microbial colonization with both mouse and human microbiomes induce Cyp3a11 expression but does not increase hepatic clearance of the Cyp3a11 substrate midazolam.

(A) ELISA quantification of Cyp3a11 in mouse liver microsomes show that CONVR mice have higher levels of microsomal Cyp3a11 compared to GF (Student's t.test, p.val < 0.05).
(B) IV midazolam 10 mg/kg concentration-time profiles in CONVR (n = 8) and GF (n =7) mice for both parent drug (midazolam) and primary metabolite (1-OH midazolam).
(C) Elimination rate constant describing midazolam elimination in CONVR and GF mice as determined by noncompartmental analysis shows GF mice have a larger midazolam elimination rate constant than CONVR mice. (Student's t.test, p.val < 0.05).
(D) Volume of distribution in CONVR and GF mice as determined by noncompartmental analysis shows no difference. (Student's t.test, p.val > 0.10),
(E) Total systemic exposure (area under the curve, AUC) of midazolam in CONVR and GF mice shows mean AUC in CONVR mice was 1.66 times higher compared to GF. (Student's t.test, p.val > 0.1)
(F) Maximum metabolite concentration (C_{max}) of 1-OH midazolam in CONVR and GF mice shows CONVR produces a higher 1-OH midazolam C_{max} compared to GF mice. (Student's t.test, p.val <0.1).
(G) Time to maximum metabolite concentration (t_{max}) of 1-OH midazolam in CONVR and GF mice shows CONVR mice have a shorter t_{max}. (Student's t.test, p.val <0.1)

(H) AUC of 1-OH midazolam in CONVR and GF mice shows CONVR mice have a smaller systemic exposure of metabolite compared to GF. Student's t.test (p.val < 0.1).
(I) ELISA quantification of Cyp3a11 in mouse liver microsomes show that HUMD mice have higher levels of microsomal Cyp3a11 compared to GF. (Student's t.test, p.value < 0.05)
(J) IV midazolam 10mg/kg concentration-time profiles in HUMD (n = 5) and GF (n =6) mice for both parent drug (midazolam) and primary metabolite (1-OH midazolam).
(K) Midazolam elimination rate constant in HUMD and GF mice as determined by noncompartmental analysis. (Student's t.test, p.val > 0.10).
(L) Volume of distribution (Vd) in HUMD and GF mice as determined by noncompartmental analysis. (Student's t.test, p.val > 0.10)
(M) Total systemic exposure (area under the curve, AUC) of midazolam in HUMD and GF mice. (Student's t.test, p.val >0.1)
(N) Maximum metabolite concentration (C_{max}) of 1-OH midazolam in HUMD and GF mice. (Student's t.test, p.val >0.1)
(O) Time to maximum metabolite concentration (Tmax) of 1-OH midazolam in HUMD and GF mice. (Student's t.test, p.val >0.1)
(P) AUC of 1-OH midazolam in HUMD and GF mice. (Student's t.test, p.val > 0.1).

Cyp3a11 protein expression increased with colonization with both mouse and human microbiomes

To determine if the increase in Cyp3a11 gene expression also led to increased protein content, we ran a Cyp3a11 ELISA to quantify its actual protein expression. We observed a significantly higher abundance of Cyp3a11 protein per mg of microsome in both CONVR and HUMD mice (Fig 3.2A, 3.2G). The 38% mean increase with CONVD and 35% mean increase with HUMD Cyp3a11 expression compared to GF should lead to a similar increase in midazolam rate of elimination as well [54].

Cyp3a11 substrate midazolam rate of elimination in mice did not correlate with increased Cyp3a11 expression

Interestingly, increased Cyp3a11 expression did not correlate with our *in vivo* pharmacokinetic studies using midazolam. Midazolam was the probe substrate of choice due to its clearance being mainly by hepatic Cyp3a11 and its high permeability and solubility as a BDDCS class 1 drug, making it susceptible to few transporter effects [55]. IV midazolam 10 mg/kg administered to either GF or CONVR mice showed the rate of elimination in CONVR mice (mean k_e 0.621 h^{-1} , standard deviation 0.178 h^{-1}) to be approximately 40% lower compared to GF mice (mean k_e 0.986 h^{-1} , standard deviation 0.337 h^{-1}) (Fig 3.2B, C). While the study was powered to detect a difference in Ke of 60% or more using t.test with n = 6 mice per group, standard deviation 33.7%, and power 0.8, we still saw a clear difference in magnitude as CONVR mice were hypothesized to have faster clearance, but instead had lower clearance compared to GF mice.

In the metabolite profile of primary metabolite 1-OH midazolam, we noticed a shorter t_{max} in CONVR mice compared to GF (1.5 h, standard deviation 0.55 h, CONVR vs 2.3 h, standard deviation 0.76 h, GF). The mean maximum metabolite concentration (C_{max}) and AUC in CONVR mice were 4.5 times lower compared to GF (Fig 3.2F-H, t.test, p.value < 0.1). This further supports our hypothesis that complex gut microbiomes produce an inhibitor that alters enzyme affinity of Cyp3a11 to midazolam.

HUMD and GF mice similarly showed no significant change in midazolam elimination rate constant (Fig 3.2K) despite the increase in Cyp3a11 in HUMD mice. Similarly, we noticed that in the profile of primary metabolite 1-OH midazolam, HUMD mice had a mean 14% higher C_{max} and shorter t_{max} (mean 1.5 h, standard deviation 0.58 h) compared to GF mice (mean 1.8 h, standard deviation 0.84 h), suggesting midazolam metabolism to 1-OH midazolam was more efficient in the initial first 2 hours (Fig 3.2M-N).

The clearance of 1-OH midazolam in both CONVR and HUMD mice was lower compared to GF as seen by the shallower slope (Fig 3.2B, J) and higher metabolite AUC (Fig 3.2H, P). This suggests that phase 2 glucuronidation of 1-OH midazolam might also be affected by colonization. RNA expression of Ugts in mice livers for both CONVR and HUMD were not significantly downregulated (Supplementary Fig 3.2) compared to GF however, pointing to the possibility of an Ugt inhibitor being present as well. Having the clearance either reduced or not changed despite the higher Cyp3a11 expression in both HUMD and CONVR mice shows that this effect is generalizable across both human and mouse gut microbiomes.

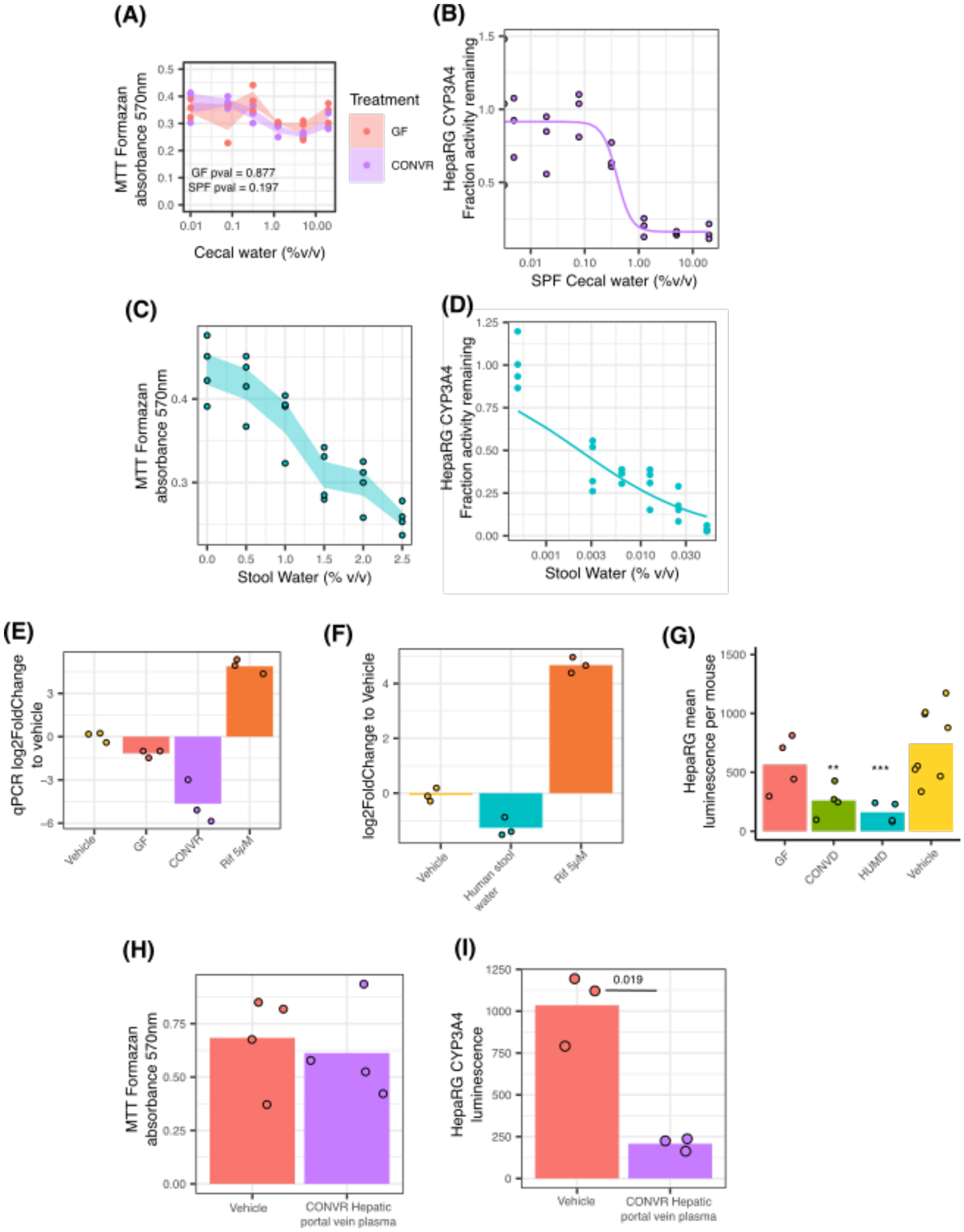

Figure 3.3 Mouse cecal and human stool water inhibit CYP3A4 in HepaRG cells at concentrations that are non-toxic to cells.

(A) MTT assay for cell viability post 72 h incubation with cecal water from both CONVR and GF mice show that cecal water at tested concentrations was not significantly toxic to HepaRG cells. (Spearman's correlation test)
(B) Log-logistic regression of HepaRG Cyp3a11 activity measured using luciferin-IPA against 4-fold dilutions of CONVR mouse cecal water show CYP3A4 is inhibited in a dose-dependent manner.
(C) MTT assay for cell viability post 72h incubation with human stool water shows stool water should be tested at concentrations <0.5%
(D) Log-logistic regression of HepaRG Cyp3a11 activity measured using luciferin-IPA against 2-fold dilutions of human stool water shows a dose-dependent inhibition of stool water on HepaRG cells.
(E) qPCR of CYP3A4 in HepaRG cells treated with 20% cecal water shows a decrease in CYP3A4 gene expression greater than 2-fold with CONVR cecal water.
(F) qPCR of CYP3A4 in HepaRG cells treated with 0.5% human stool water shows a decrease in CYP3A4 gene expression greater than 2-fold.
(G) HepaRG cells incubated with sterile filtered cecal water 2.5% v/v from GF (n =4), CONVD (n=4), or HUMD (n=4) mice for 72 h in cell media show a decrease in CYP3A4 activity as seen with decreased luminescence of CYP3A4glo IPA substrate. Each point represents a mean of 4 technical replicates in a 96 well plate. ANOVA with Tukey hsd post hoc test was used to determine statistical significance.
(H) Pooled hepatic portal vein plasma 20% v/v from CONVR mice (n=3) incubated with HepaRG cells for 72h does not show a difference in cell viability measured by MTT cell viability assay. (Student's t.test, pval > 0.05)
(I) Pooled hepatic portal vein plasma 20% v/v from CONVR mice (n=3) incubated with HepaRG cells for 72h show a decrease in HepaRG CYP3A4 activity compared to the vehicle of 20% heparinized normal saline. Each point is a technical replicate. (Student's t.test, pval < 0.05).

Establishing HepaRG as a reliable screening tool for gut microbial metabolites

Initial screenings of stool water using microsomes yielded very strong inhibition effects due to the high propensity for enzyme sequestration due to the high amount of colloid formation in stool water [56]. This resulted in microsomal inhibition being much stronger than it was in reality. An intact CYP enzyme system such as a HepaRG assay that was less susceptible to such *in vitro* artefacts was preferable [57].

Screening gut microbial metabolites from stool in cell culture was a challenge due to the high amount of toxic metabolites present in stool [58]. While DMSO was a key component in differentiating media to maintain a high level of CYP expression in HepaRG cells, it also causes a high amount of stress to cells [59], making cells easily susceptible to toxicity from treatments. By using a low dose of 0.1 μM rifampicin to induce CYP3A4 rather than DMSO however, we were able to establish a robust and sensitive model and preparation method for stool water to screen for CYP3A4 inhibitors produced by the microbiome without significant cell toxicity. Unlike most papers that establish cell viability using the lactodehydrogenase (LDH) assay [60], we had to use Alamar blue which measures cell viability via metabolic function [61] instead as our biological matrices, stool water, and portal vein plasma, contained high levels of LDH [62,63], which significantly confounded our cell viability results. We further validated the cell viability results using the MTT assay, which measures cell viability using mitochondrial activity [64] to demonstrate that the cells were viable at the stool water concentrations tested. While cecal water could be tested at concentrations up to 20% v/v(Fig 3.3A), stool water had to be highly diluted, with the maximum nontoxic concentration to be used at 0.5% v/v (Fig 3.3C).

One caveat of this method, however, was that strong CYP3A4 inhibitors also tended to give higher viability readouts with Alamar blue, as seen with our positive control ketoconazole, making it possible that the cell viability for certain stool water fractions was smaller than we observed. This is why visual observation of the cells for monolayer integrity and morphology [65]was carried out as well to ensure overall cell health. We defined cell toxicity as a statistically significant change in correlation of cecal water/stool water concentration to resazurin fluorescence (Spearman's correlation) and/or disruption of the HepaRG monolayer. Alamar blue cell viability results for subsequent experiments are available in Supplementary Fig 3.3.

Mouse cecal and human stool water contain Cyp3a11 inhibitor that decreases both expression and function

Based on the multiple PXR and CAR genes being upregulated (Fig 1C), we hypothesized that mouse cecal water from both HUMD and CONVD mice would induce CYP3A4 in HepaRG cells, a validated human hepatocyte cell line commonly used for the study of drug induction of CYP enzymes. At the concentrations that were deemed to be nontoxic, we found that both human stool and CONVR cecal water inhibited CYP3A4 in a dose-dependent fashion instead (Fig 3.3B, D).

We then quantified HepaRG CYP3A4 gene expression via qPCR with both mouse cecal water and human stool water. CONVR cecal water 20% v/v inhibited CYP3A4 expression (log2 fold change to vehicle -4.65 +/- sd 1.49) to a larger extent compared to GF cecal water 20% v/v (log2 fold change to vehicle -1.16 +/- sd 0.271) (Fig 3.3E). Similarly, human stool water 0.5% v/v also inhibited CYP3A4 gene expression by 2-fold (Fig 3.3F). When we tested for function, we found that cecal water from HUMD and CONVD mice 2.5% v/v inhibited CYP3A4 activity (79% and 65% decrease in activity to vehicle) to a much greater extent compared to GF cecal water (24% decrease in activity to vehicle) (Fig 3.3G). This further supported our hypothesis that these microbiomes were also producing an inhibitor.

To ensure that the compound was also bioavailable to the liver, we harvested hepatic portal vein plasma from CONVR mice (n=3) and treated HepaRG cells with them in a similar manner. The plasma was pooled to get sufficient volume for experiments. We also observed strong CYP3A4 inhibition (~80% decrease in activity to vehicle) (Fig 3.3I) without significant cell toxicity (Fig 3.3H), indicating that the inhibitor was able to get past the intestine walls into the portal vein and thus reach the liver to exert its effect.

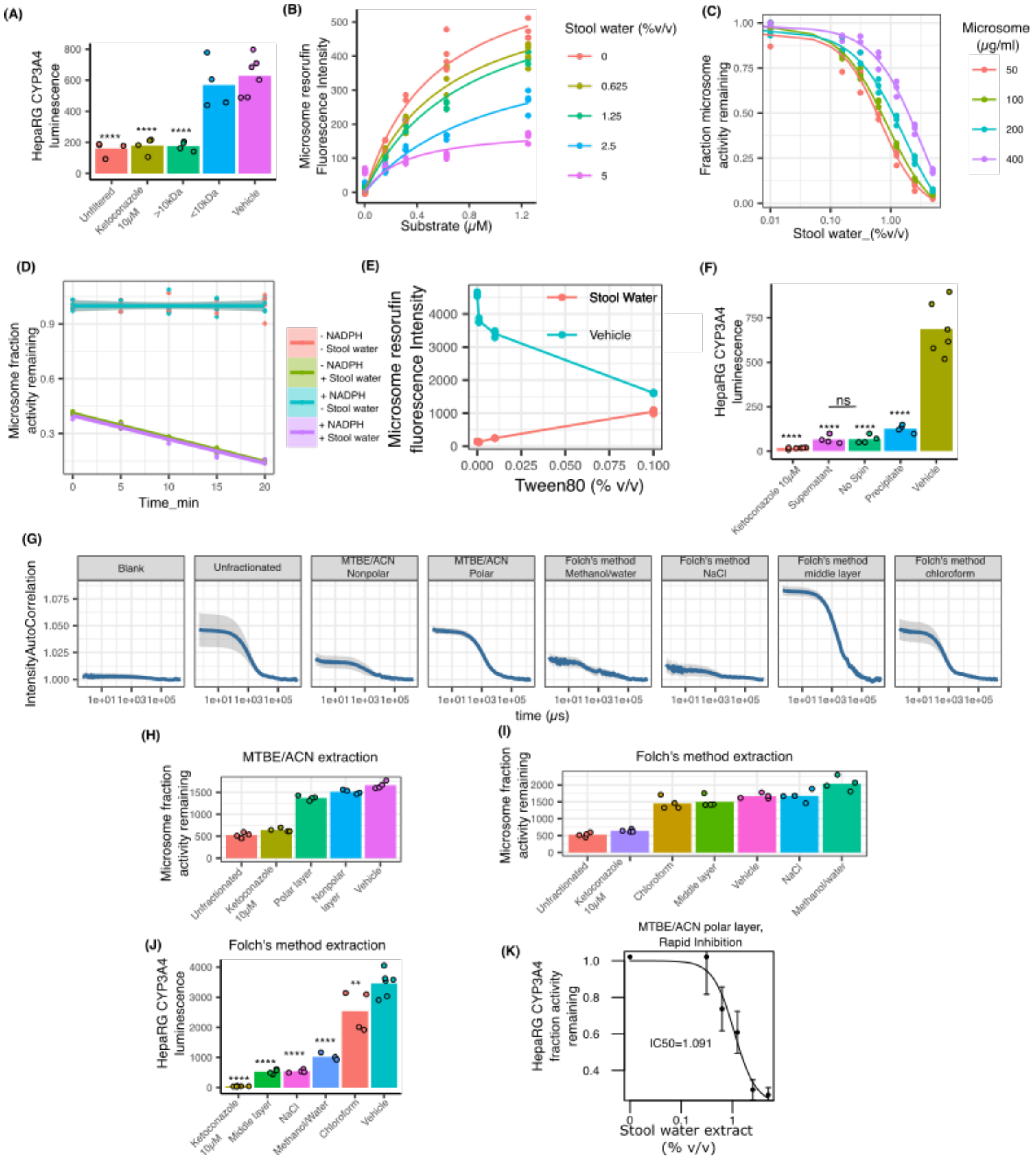

Figure 3.4 The Cyp3a11 inhibitor has colloidal properties and can rapidly cause inhibition in both microsomal and intact cell systems.

(A) HepaRG cells incubated with human stool water size selected for either larger or small than 10 kDa show loss of activity in fractions smaller than 10 kDa. ANOVA with Tukey hsd post hoc test was used to determine statistical significance.

(B) Characterizing the inhibitor's mechanism of inhibition using an increasing concentration of stool water against increasing concentrations of Cyp3a11 specific substrate benzyloxy resorufin reveals the mechanism is not competitive.

(C) Tight binding assay characterizing the effect of increasing microsome concentration on IC_{50} of stool water shows an increasing IC_{50} with increasing microsome concentration.

(D) Time dependent inhibition of microsomes with stool water with or without NADPH cofactor present in preincubation shows that the inhibitor exhibits NADPH independent time dependent inhibition.

(E) Testing for the presence of colloidal aggregates in stool water by addition of a nonionic surfactant Tween 80 to disrupt aggregates and recover Cyp activity in microsomes.

(F) Centrifuged sterile filtered stool water at 4°C, 21130*g*, tested in HepaRG cells for CYP3A4 activity showed that the inhibitor was not easily pelleted.

(G) Dynamic light scattering of stool water and its organic solvent extractions at 0.3125% v/v. Folch's method reveals the inhibitor was released from its colloid in its aqueous fractions but continued to show activity as observed in Fig 4B.

(H) MTBE/ACN extract has less activity compared to unfractionated stool water in microsomes, indicating organic solvent extraction reduces the propensity for non-specific colloidal aggregation.

(I) Folch’s method also yields less activity in microsomes compared to unfractionated stool water. Of note, the methanol/water layer increased Cyp3a11 activity.

(J) A two-step Folch’s method applied to stool water reveals the inhibitor is amphiphilic, with the inhibitory activity present in all layers of extraction, both polar and nonpolar when tested against HepaRG.

(K) A 1h incubation of stool water extracted with MTBE/ACN (50/50) in HepaRG cells shows that the inhibitor rapidly decreases CYP3A4 activity.

Characterizing the inhibitor’s chemical properties and mechanism of action

With CYP3A4 inhibition being reproduced both *in vivo* in mice and *in vitro* in HepaRG cells, we sought to characterize the inhibitor’s properties. We first attempted to characterize the inhibitor by size selection using HepaRG as a screening tool before characterizing its mechanism of inhibition using mouse liver microsomes for both reversible and tight binding inhibition. Characterizing the inhibitor for its mechanism of inhibition would help us to better understand its inhibitory potency and chemical properties to isolate the compound more effectively.

Size selection by filtration revealed the compound was >10 kDa in stool water

Thinking that the inhibitor was likely to be a small molecule, we first did size selection using centrifugal filters. To our surprise, we found that stool water fractions < 10 kDa did not inhibit HepaRG CYP3A4 activity (ANOVA with Tukey hsd post hoc, pval > 0.1), but rather, the active component remained in the filter residue >10 kDa with ~66% decrease in CYP3A4 activity compared to control (ANOVA with Tukey hsd post hoc, pval < 0.01) (Fig 3.4A). This decrease in activity was similar to unfiltered stool water. This was consistent with the molecule either being a macromolecule, highly protein bound, or a colloidal aggregator.

Reversible inhibition assay shows stool water does not act via competitive inhibition

Reversible inhibition of CYP3A4 by stool water using BzRes as the probe substrate showed that with increasing stool water concentration, V_{max} was reduced, but K_m remained relatively consistent (K_m at 0% v/v stool water 0.56 μM, K_m at 5% v/v stool water 0.32 μM) (Fig 3.4B), with none of the values being more than 2-fold different from vehicle control[20,32]. This suggested that the mode of reversible inhibition was not competitive.

Increased microsome concentration increases IC_{50}, suggesting tight binding

We then tested the inhibitor for tight binding by testing increasing stool water concentrations against increasing microsome concentrations. As stool water resulted in increasing IC_{50} (0.685, 0.859, 1.61 and 3.26% v/v for microsome concentrations 50, 100, 200 and 400 μg/ml respectively) and steeper dose responses with increasing microsome concentrations, this pointed toward the molecule being a tight binder (Fig 3.4C). Tight binders will have increased IC_{50} with increased microsome concentration due to a 1:1 binding ratio with the enzyme [32].

The inhibitor showed NADPH independent time dependent inhibition

As the molecule showed tight binding, further testing for time dependent inhibition was warranted. Stool water's inhibition of Cyp3a11 increased over time with or without the presence of NADPH in the primary incubation to an equal magnitude (K_{obs} without NADPH 0.011min^{-1} (0.0102-0.0119 min^{-1}, 95% confidence interval), K_{obs} with NADPH 0.0102min^{-1} (0.00907-0.0113 min^{-1}, 95% confidence interval)) (Fig 4D), indicating that the time dependency was NADPH independent and likely not CYP mediated such as via mechanism-based inhibition [32].

Inhibitor forms colloidal aggregates whose inhibitory activity can be attenuated by detergent

All three inhibition assays (Fig 3.4B-D) suggested that the inhibitor was a colloidal aggregator[13,56,57]. It was likely that the inhibitor was sequestering enzyme activity via aggregation. This was confirmed by adding small amounts of nonionic detergent, tween 80, to an enzyme incubation of 5% v/v stool water and comparing its activity against vehicle (Fig 4E) [32]. Activity was almost fully recovered with the addition of 0.1%v/v tween 80.

The inhibitor could not be easily pelleted unlike most aggregate forming molecules

Small molecule aggregates are usually easily removed via centrifugation[57]. However, despite spinning the stool water down at 21130*g*, 4°C for 30 min, the supernatant still retained most of the stool water's activity when compared with unspun stool water (ANOVA with Tukey post hoc test, pval > 0.05) (Fig 3.4F). The colloidal properties along with the aggregate being hard to pellet suggest the inhibitor could be a lipid.

Dynamic light scattering confirms the presence of colloids in stool water and its extracted fractions

Dynamic light scattering was employed to confirm the presence of colloids in stool water and its fractions. At the concentration closest to our usual HepaRG assay stool water concentration of 0.5% v/v, we found that stool water contained colloids, as seen by a well-defined sigmoidal curve (Fig 3.4G). Organic solvent fractions (methanol/water fraction of Folch's method and MTBE/ACN nonpolar fraction) however caused the release of the inhibitor from the colloid as observed in the MTBE/ACN nonpolar fraction and methanol/water fraction of Folch's method(Fig 3.4G). These fractions were shown to have much lower activity in microsome assays (Fig 3.4H-I) but were still highly active in inhibiting HepaRG CYP3A4 activity (Fig 3.4J). This points toward a separate mechanism from nonspecific aggregation inhibiting CYP3A4 activity.

The inhibitor was likely to be amphipathic and was present in both polar and nonpolar layers of Folch's method

When we tested all three layers from Folch's method against HepaRG cells we found that inhibitory activity was present in all layers, with a preference toward the polar and unextractable middle layers (Fig 3.4J). This suggested that the compound had amphiphilic properties, potentially being a charged lipid.

Testing for aggregation in a cell-based HepaRG assay shows activity possibly separate from aggregation

The above findings shed light that our molecule is likely to be colloidal and that microsome and other *in vitro* enzyme assays may not be suitable to estimate true enzyme activity values due to the *in vitro* enzyme sequestration that occurs due to aggregation. Unlike microsomes which are enzyme containing vesicles from fragmented rough endoplasmic reticulum, HepaRG cells contain fully intact organelles with CYPs attached within its membranes, making it much more difficult for aggregation to occur[57,66].

To ensure that the inhibition was still occurring in an intact system and that the molecule was not a protein, we extracted the inhibitor from stool water using MTBE/ACN (50:50 v/v) which would precipitate and denature most proteins[63] and incubated its reconstituted extract for an hour with HepaRG before immediately measuring CYP3A4 activity. The MTBE/ACN extract rapidly inhibited CYP3A4 activity, in a dose-response manner (Fig 3.4K). Curve fitting using log-logistic regression showed fixing the Hill coefficient to 1 (drc LL.4, Akaike's information criterion (AIC) -10.2) had a similar fit to having a Hill coefficient greater than 1 as defined by the model fitting (drc LL.5, AIC -8.42). A general rule of thumb for a significant change in AIC value would be a difference of 10 or more[67]. This implied that the dose response was not unusually steep and that the inhibition was less likely to be via aggregation, which tends to produce steep dose-response curves[57,67].

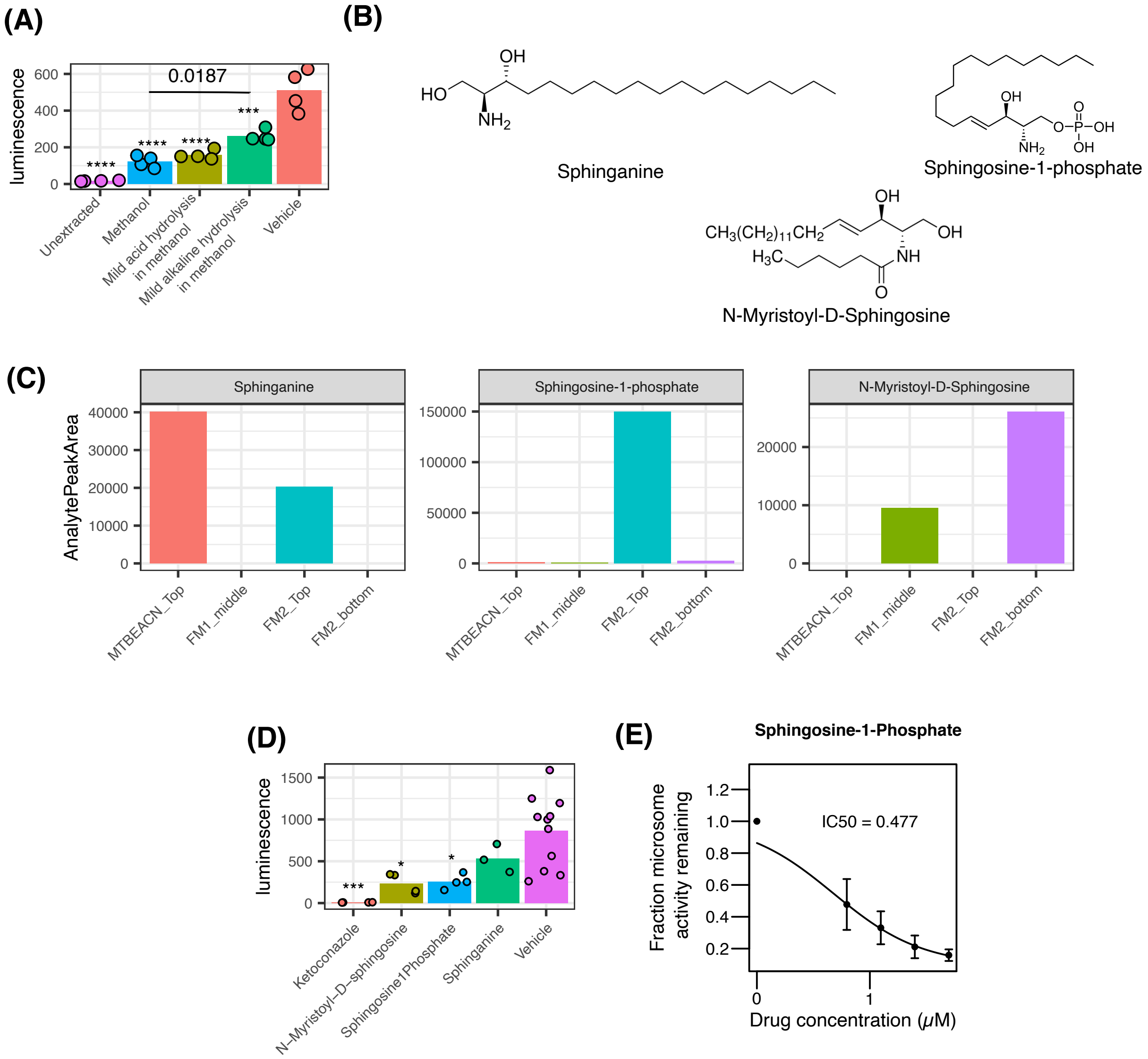

Figure 3.5 Sphingolipids present in stool water extracts can inhibit CYP3A4 activity in HepaRG cells.

(A) Mild alkaline hydrolysis is a process that selects for sphingolipids. Although some activity was lost compared to stool water without hydrolysis, mild alkaline hydrolysis still retained inhibitory activity. (ANOVA with Tukey post hoc test)

(B) Structures of known sphingolipids selected for testing. These compounds were easily purchased commercially, present in the active fractions of Folch's method, and were structurally diverse from one another.

(C) Targeted abundances of known sphingolipids in selected extraction methods compatible with LC/MS/MS analysis shows different sphingolipids were abundant in different fractions.

(D) Selected sphingolipids tested at 2.5 μM showed CYP3A4 inhibition in HepaRG cells after coincubation for 72 h. This implies that more than one sphingolipid contributes to CYP3A4 inhibition.

(E) Sphingosine-1-phosphate, which was highly abundant in the methanol/water layer from Folch's method, shows dose dependent inhibition.

Using mild alkaline hydrolysis to select for sphingolipids, an amphipathic class of lipids known to be produced by both host and the microbiome

The gut microbiome is a known producer of sphingolipids, a class of charged lipids, which are known to be bioavailable in the host liver and exert a wide range of physiological effects[68]. Our previous tests using cecal water also showed that GF cecal water did inhibit CYP3A4 activity, although to a lesser extent compared to CONVD and HUMD cecal water (Fig 3.3E). This suggested that the compound could be also produced by the host, of which sphingolipids are known to be produced by both host and microbiome. We thus did a preliminary selection using mild alkaline hydrolysis in methanol, a technique known to select sphingolipids from other lipids[69]. Stool water post alkaline hydrolysis (51 ± 12.3% activity remaining) lost some inhibitory activity compared to the unhydrolyzed control (24 ± 26.2% activity remaining) (pval <0.05), but was still able to significantly inhibit CYP3A4 activity compared to vehicle (pval <0.01), giving us more confidence that the compound could be a sphingolipid (Fig 3.5A).

A targeted sphingolipid panel identified structurally diverse and active sphingolipids present in different stool water fractions

A targeted sphingolipid panel was then applied to different organic solvent extractions of stool water, where we aimed to identify a panel of 35 known sphingolipids in the different fractions. Sphinganine, sphingosine-1-phosphate, and N-myristoyl-D-Sphingosine were chosen for testing as these compounds were easily purchased commercially, present in the active fractions of our extractions (Fig 5C), and were structurally diverse from one another (Fig 3.5B). All of our compounds showed CYP3A4 inhibition in HepaRG cells (Fig 5D). Also, sphingosine-1-phosphate demonstrated inhibition in a dose dependent manner, suggesting that it and similar compounds could be the inhibitor (Fig 3.5E).

An interesting observation we noticed for N-Myristoyl-D-Sphingosine and sphinganine was that their dose responses were bell-shaped, unlike a normal sigmoidal dose response curve (Supplementary Fig 3.4). This is a known phenomenon for colloidal molecules which reflects the concentration of bioactive, monomeric compounds at low concentrations, before aggregating in solution at higher concentrations, sequestering the bioactive compound[70].

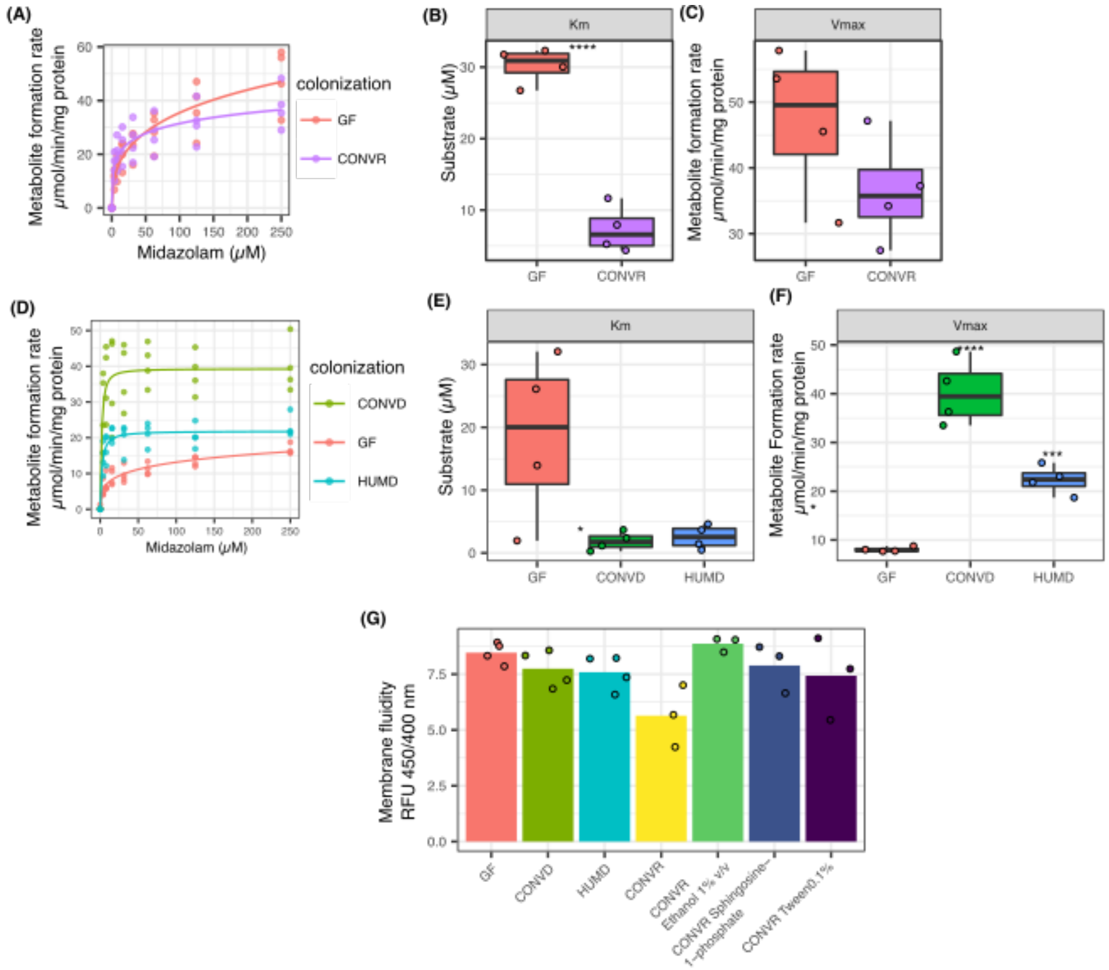

Figure 3.6 Gut microbiome modifies microsome membrane fluidity and function

(A) Michaelis Menten plot comparing enzyme kinetics of GF and CONVR mice using midazolam as a probe substrate shows GF microsomes are not as easily saturated with higher K_m and V_{max}.
(B) Binding affinity (K_m) extracted from fig 6A per mouse shows GF mice have a much lower binding affinity with higher K_m compared to CONVR mice.
(C) Maximum metabolite formation rate (V_{max}) from fig 6A per mouse shows GF mice have higher V_{max} compared to CONVR mice.
(D) Michaelis Menten plot comparing enzyme kinetics of GF, CONVD and HUMD mice using midazolam as a probe substrate shows CONVD and HUMD mice have higher V_{max} and also higher enzyme affinity as seen with lower K_m values.
(E) Binding affinity (K_m) extracted from Fig 6D per mouse shows GF mice have a much lower binding affinity with higher K_m compared to CONVD and HUMD mice.
(F) Maximum metabolite formation rate (V_{max}) from Fig 6D per mouse shows CONVD and HUMD mice have higher V_{max} compared to GF mice.
(G) Membrane fluidity assay of microsomes collected from GF, CONVD, HUMD and CONVR mice show GF mouse microsomes had the most fluid membranes.

Characterizing mouse liver microsomes derived from GF and colonized mice

Knowing that the inhibitor was likely acting on a site independent of the CYP enzyme (Fig 3.4B-D) and that there were multiple possible sphingolipid inhibitors (Fig 3.5D), we hypothesized that the inhibition was likely occurring via membrane interactions. To investigate we characterized the Michaelis Menten kinetics and microsomal membrane fluidity of CONVR vs GF mouse microsomes, as well as CONVD, HUMD vs GF mouse microsomes using our optimized microsome method to preserve the effect of the gut microbiome on Cyp3a11 enzymes.

Preserving the microbiome's effect on liver microsomes required the addition of protease inhibitor during preparation

An interesting observation we came across during this investigation was that the addition of a protease inhibitor cocktail during microsome preparation preserved the effect of the gut microbiome. In preparations without protease inhibitor cocktail, the microsomal activity of CONVR mice was much larger (approximately 2-fold increase in activity) compared to GF mice (Supplemental Fig 3.5A). With the protease inhibitor, GF mice have approximately 20% higher activity, which correlates more with our observed *in vivo* midazolam clearance in mice (Fig 3.1A). All methods, except for Tris HCl with protease inhibitor, were able to produce CYP450 CO spectrums, indicating intact and functional CYPs (Supplemental Fig 3.5B). As midazolam is highly cleared by hepatic CYP3A4 and not affected highly by transporter effects, its *in vivo* clearance should correlate highly with enzyme activity without other interferences[71]. Hence, we believe that the microsomal preparation with the addition of just protease inhibitor cocktail more accurately reflects enzyme activity in vivo compared to preparation without a protease inhibitor. It is likely that the protease inhibitor cocktail not only protects against enzyme degradation, but also preserves membrane integrity, and thus is used in microsome preparations studying protein-membrane interactions.

GF mouse microsomes have lower binding affinity and lesser saturation compared to CONVR microsomes

As microsomes had both lipid bilayer membrane and enzymatic components, we sought to characterize the microsome Michaelis Menten kinetics from GF and CONVR mouse microsomes using midazolam as a probe substrate. Midazolam was used instead of BzRes so we could make comparisons back to the *in vivo* pharmacokinetic midazolam profiles as well.

One of the first striking differences we found was that GF mice had a lowered enzyme affinity for midazolam as noted by its increased K_m compared to CONVR mice (Fig 3.6A, B). With the increased K_m, GF microsomes did not reach saturation even at 250 μM midazolam which was 20 times K_m in CONVR mice. This is expected as K_m is half of V_{max}, implying that a higher K_m would usually imply a higher V_{max} when all Michaelis Menten assumptions hold [72]. This helps to explain the 1-OH midazolam pharmacokinetic profile in CONVR vs GF mice, with CONVR mice having a shorter t_{max} due to higher enzyme binding affinity allowing for a faster initial reaction, and lower C_{max} due to CONVR being more easily saturated compared to GF mice (Fig 3.2B). Notably, GF mice had a higher rate of elimination of midazolam which could be attributed to its lower saturation rate at higher midazolam concentrations. This means that its enzyme activity would continue increasing with increased concentrations of midazolam, compared to CONVR mice, which would have a constant rate of metabolite production at high concentrations of midazolam.

GF mice colonized with either mouse cecal (CONVD) or human stool (HUMD) also shows an increase in binding affinity compared to GF

When we compared GF against CONVD and HUMD mice, both the colonized mice groups did have higher V_{max}, which matches the ELISA results of higher Cyp3a11 expression per mg of microsome, which would expectedly give higher V_{max} values. However, GF mice still had a higher K_m compared to both CONVD and HUMD mice (Fig 3.6E). This was evident in the 1-OH midazolam metabolite profile of HUMD vs GF mice too, with GF mice having a longer t_{max} compared to HUMD mice (Fig 3.2J). Both results from CONVR vs GF and HUMD and CONVD vs GF mice imply that the gut microbial colonization changes Cyp3a11 binding affinity for midazolam.

Gut microbial colonization reduces membrane fluidity in mouse microsomes

Our measurement of membrane fluidity with lipophilic pyrene probes showed that GF mice had higher membrane fluidity (RFU 8.46 ± 0.48) compared to CONVD (RFU 7.74 ± 0.836) and HUMD mice (RFU 7.59 ± 0.782) (Fig 3.6G). CYP3A4 has been shown to be highly sensitive to changes in membrane fluidity[73], suggesting this could be the mechanism by which the gut microbiome influences enzyme kinetics and thus hepatic clearance. Interestingly, sphingosine-1-phosphate increased membrane fluidity (Fig 3.6G). However, sphingolipids tend to form microdomains where cholesterol can bind in a more entropically favoured fashion[74]. This could in turn increase membrane rigidity instead which we observe with the colonized mice.

Alteration of enzyme kinetics by the gut microbiome is consistent across gender

Our initial microsome studies comparing gene expression and microsome activities between GF, CONVD, and HUMD mice were done in C57/B6 male mice. However, upon confirming that Cyp3a11 was a target of interest, we switched to balb/c female mice, which were easier to administer IV drugs to and had generally higher basal levels of Cyp3a11 expression compared to male mice. The difference between sexes helps to explain the differences in V_{max} between GF mice in Fig 3.6A and B. However, we still see a consistent signal of altered K_m (Fig 3.6B, E) and V_{max} (Fig 3.6C, F) values when comparing GF against colonized mice, indicating the effect was not limited to one gender.

Time and of gut microbial colonization may influence the extent Cyp3a11 inhibition

In Fig 3.6A, CONVR mice were colonized since birth, but in Fig 3.6B, CONVD mice were colonized for only 2 weeks as adult GF mice prior to sacrificing. Compared to GF, CONVD mice had a 4-fold higher V_{max} while CONVR had a lower V_{max} compared to GF. It is possible that the age at colonization and duration of colonization can have effects on how much the membrane fluidity is altered. Age dependent changes in membrane fluidity are a known phenomenon[75,76]. However, both CONVD and CONVR demonstrate a reduction in K_m and membrane fluidity, indicating that the effect was still generalizable.

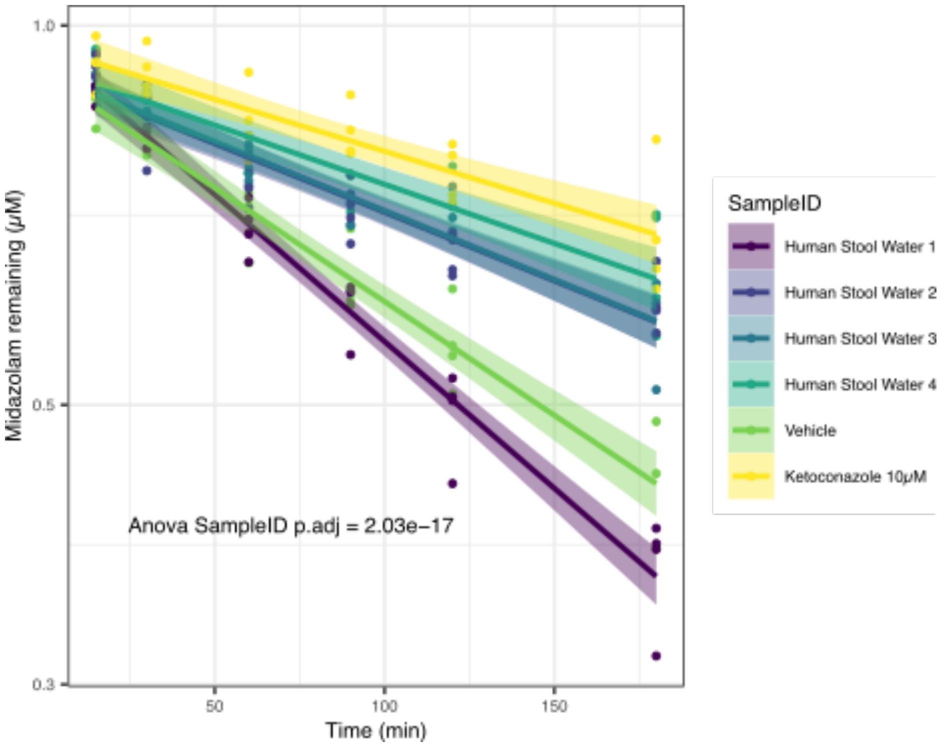

Figure 3.7 Unique human stool samples modulate midazolam metabolism in HepaRG cells.

Midazolam metabolism was quantified in HepaRG cells incubated with stool water and showed different levels of CYP3A-mediated metabolism. (ANOVA test for difference between linear regressions was run only between samples with vehicle and ketoconazole controls excluded. Padj < 0.01)

Human stool water from four unique donors alter CYP3A4-mediated midazolam metabolism in HepaRG cells to different extents

Since human stool water was able to inhibit CYP3A4 activity, we investigated whether stool water from different human donors would affect CYP3A-mediated metabolism differently. After incubating HepaRG cells in serum-free differentiating media for 72 h with 0.1% v/v stool water, we measured HepaRG's ability to metabolize midazolam over time. Each unique stool water sample produced a different extent of metabolism (ANOVA padj <0.01), supporting our hypothesis that the gut microbiome could be producing an inhibitor that modulates CYP3A4 activity that may contribute to inter-individual variation. While three out of four of our samples caused inhibition, one sample resulted in a higher rate of midazolam metabolism than vehicle (Fig 3.7), suggesting that the microbiome both induces and inhibits CYP3A4 activity.

Discussion

Gut microbiomes of both mice and humans inhibit Cyp3a11 and CYP3A4 activity

To the best of our knowledge, we are the first to report that the human gut microbiome decreases hepatic drug clearance and that alteration of membrane fluidity is a potential mechanism for this effect. In our quest to understand the functional consequences of the gut microbiome on CYP3A4 mediated drug clearance, we have found that in *in vivo* mouse studies, gut microbial colonization with both human and mouse microbiomes induces hepatic mouse Cyp3a11 gene and protein expression. We also found that the gut microbiome produces Cyp3a inhibitors in both mouse and human microbiomes with CONVR and HUMD mice having a decreased rate of elimination or no change in rate of elimination, respectively, compared to GF. Screening of mouse cecal water and human stool water in human hepatocyte HepaRG cells also confirmed the presence of a human CYP3A4 inhibitor in both species.

While we are the first to describe the IV profile of midazolam in gnotobiotic mouse models, our UCSF gnotobiotic core has advised us that GF mice tend to require higher doses of ketamine/xylazine compared to CONVR mice for surgical procedures. Both Ketamine and xylazine are cleared mainly by hepatic CYP3A4 [77,78]. This supports our hypothesis that the microbiome reduces Cyp3a11 mediated drug clearance.

The human gut microbiome produces inhibitors with sphingolipid properties that reduce CYP3A4 activity and might contribute to interindividual variability

Further characterization of the CYP inhibitor using human stool water and its organic solvent extracts revealed the likelihood of multiple inhibitors. The inhibitors had sphingolipid-like properties, such as being hard to pellet by centrifugation, amphiphatic, and resistant to mild alkaline hydrolysis. Known sphingolipids, such as sphingosine-1-phosphate demonstrated inhibition of CYP3A4 activity in HepaRG cells. A separate study has shown similar inhibition of CYP3A4 expression with structurally related ceramides [79]. Lastly, our screen of altered midazolam metabolism in HepaRG cells from four different human donors shows that different microbiomes inhibit CYP3A4 to different extents, suggesting the gut microbiome might play a role in explaining CYP3A4 variability.

The importance of the administration route on CYP3A4 activity

The majority of PK studies in gnotobiotic mice have been done via oral administration which can cause clearance to be confounded by other processes affecting bioavailability such as intestinal metabolism and absorption. IP administration also has effects of absorption and first pass metabolism processes despite avoiding gut microbial metabolism [80]. IV administration bypasses these other processes, giving us a clear picture of hepatic clearance, and allowing us to conclude that gut microbial colonization inhibits Cyp3a-mediated clearance.

Gut microbial sphingolipids are bioavailable to the liver and impact host physiology

While most of our screenings were done using cecal water and stool water, we also ensured that our inhibitor was bioavailable by testing portal vein blood, which carries blood from the intestines directly to the liver. Another study by Johnson et al. looking at sphingolipids produced by the gut microbiome has similarly shown that sphingolipids produced by gut bacteria can transit from bacterial cells to the gut epithelium and hepatic portal vein, and exert an effect on host physiology[20]. Sphingolipids are known to mediate host-microbiome interactions, and were shown to influence host lipid metabolism [20]. Gut microbial sphingolipid production impacting host drug metabolism is hence highly plausible too, as we have described in our study.

Sphingosine-1-phosphate is produced by both the gut microbiome and host

Finding that Sphingosine-1-phosphate was an active compound in CYP3A4 inhibition produced by both gut microbiome and host [20] further helped us to explain our results that GF cecal water caused CYP3A4 inhibition, but to a smaller extent compared to CONVD and HUMD samples (Fig 3.3E). Interestingly, we did not observe significantly different changes in gene expression (DESeq2) to host sphingolipid metabolism or ceramide production in our liver samples with CONVD and HUMD samples compared to GF (Supplementary Fig 3.6).

Alteration of membrane fluidity affects CYP function

Sphingolipids are the second most abundant structural lipids after glycerolphospholipids [81]. Sphingolipids are also known to form lipid rafts with cholesterol, decreasing membrane fluidity [82,83]. CYP3A4 activity decreases with decreased membrane fluidity, but the successful inhibitor Sphingosine-1-phosphate increased membrane fluidity (Fig 3.6G), and the methanol/water extract containing S1P increased Cyp3a11 microsomal activity compared to vehicle(Fig 3.4I). This is likely because cholesterol was missing within the in vitro system. Sphingolipids make membranes more fluid which helps cholesterol to bind, making membranes more rigid [84].

Although our proposed mechanism is novel for gut microbial metabolites, similar proposed modifications to membrane structure have also been proposed with nanoparticle interference of CYP activity via integration with the microsomal membrane and alteration of active site binding [85].

Variation in *Bacteroidetes*, a known phylum of sphingolipid producers, could help explain interindividual variability

Our results with four different human donors demonstrate that different microbiomes can alter clearance to different extents (Fig 3.7). Notably, *Bacteroidetes*, one of the most abundant phyla in most human gut microbiomes[86,87], have known sphingolipid producers, with genomes of *Bacteroides* spp. and their relatives encoding serine palmitoyltransfease (SPT), allowing them to produce sphingolipids [68]. As one of the dominant phyla in the human gut microbiome, Bacteroidetes also have high interindividual variability[88–92]. It is thus plausible that the gut microbiome affects CYP3A4 activity via its Bacteroidetes abundance and sphingolipid production.

Caveats

Stool water preparation selects for hydrophilic compounds

Stool water preparation selects for compounds that are soluble in water and that are not highly protein bound, as these compounds are likely to be pelleted with the solid debris during centrifugation. Lithocholic acid (LCA), a known PXR inducer and gut microbial metabolite, is highly protein bound[93]. LCA is directly extracted from feces via organic solvent extraction[94]. This could also explain why the treatment of HepaRG with stool water decreased CYP3A4 mRNA expression, rather than increased as expected from the presence of PXR agonists in stool water.

Incubation time is important in determining the effect of gut microbial inhibitors on CYP3A4 activity

In Fig 4H and I, the microsomes were pre-incubated with the stool water fractions for only 5 min prior to starting the assay. However, with HepaRG (Fig 3.4K) and membrane fluidity (Fig 3.6G) assays, stool water fractions/sphingolipids were incubated for an hour prior to any measurements being done. It is likely that the gut microbial inhibitors need time to diffuse into and incorporate with the membrane before a noticeable effect can be observed.

Future directions

With the large metabolic capability of the gut microbiome, there are likely active CYP3A4 inhibitors that have yet to be characterized. Therefore, it would be worthwhile to carry out untargeted metabolomics on these stool water fractions to discover novel compounds that could be tested for effects on drug metabolism.

Since cholesterol and sphingolipids tend to form lipid rafts together, it will be important to test sphingolipids with cholesterol in microsomes to find out if that makes the microsomal membrane more rigid, increasing binding affinity.

We would also like to do more targeted metagenomic analyses between CONVR, CONVD, and HUMD on sphingolipid pathways. Our current analyses did not completely capture sphingolipid related pathways, and human gut microbiome genes were grossly overrepresented in the dataset compared to the less well characterized mouse gut microbiome (Supplementary Fig 3.7). 16S analyses however did point toward the *Bacteroidetes* phyla having the most differences between human and mouse microbiome in our study (Supplementary Fig 3.1C), which could account for differences in CYP induction and inhibition.

To find out if our hypothesis of either increased *Bacteroidetes* or sphingolipid pathway abundances correlates with decreased clearance, we would also like to test more human stool samples on HepaRG clearance to get a larger effect size, and explore the differences in gut microbial composition between the unique human stool donors using both a targeted sphingolipid and untargeted metagenomic approach.

We would also propose testing individual strains of *Bacteroidetes* with and without serine palmitoyltransferase both in mice as monocolonization and in HepaRG by incubating extracted lipids from Folch's method in bacterial culture to further test if bacterial derived sphingolipids are indeed causing the decrease in CYP3A4 activity.

Conclusion

In conclusion, our study has shown that both human and mouse microbiomes induce but also inhibit Cyp3a11 in mice and CYP3A4 in humans. *In vivo*, colonized mice had higher Cyp3a11 expression but did not necessarily have higher clearance. Screening using HepaRG cells showed high levels of CYP3A4 inhibition by both cecal and human stool water. Characterization of the inhibitor identified sphingolipids as a potential class of inhibitors, of which sphingosine-1-phosphate was shown to be a CYP3A4 inhibitor. Due to the nature of Cyp3a inhibition we observed using microsomes, we propose that the microbiome alters CYP activity via sphingolipid production that changes hepatic endoplasmic reticulum membrane fluidity. Different human microbiomes can also cause differences in CYP3A4-mediated metabolism in HepaRG cells. These findings help to shed light on the possibility that the gut microbiome could be another paradigm to understand CYP3A4 interindividual variability between humans.

References

1. Cytochrome P450 enzymes in drug metabolism: Regulation of gene expression, enzyme activities, and impact of genetic variation. *Pharmacol. Ther.* **138**, 103–141 (2013).
2. Center for Drug Evaluation & Research. In Vitro Drug Interaction Studies — Cytochrome P450 Enzyme- and Transp. https://www.fda.gov/regulatory-information/search-fda-guidance-documents/vitro-drug-interaction-studies-cytochrome-p450-enzyme-and-transporter-mediated-drug-interactions (2020).
3. Zhou, S. F., Xue, C. C., Yu, X. Q., Li, C. & Wang, G. Clinically important drug interactions potentially involving mechanism-based inhibition of cytochrome P450 3A4 and the role of therapeutic drug monitoring. *Ther. Drug Monit.* **29**, (2007).
4. Tracy, T. S. *et al.* Interindividual Variability in Cytochrome P450-Mediated Drug Metabolism. *Drug Metab. Dispos.* **44**, (2016).
5. Kathrin Klein, U. M. Z. Pharmacogenomics of Cytochrome P450 3A4: Recent Progress Toward the “Missing Heritability” Problem. *Front. Genet.* **4**, (2013).
6. Togao, M. *et al.* Effects of gut microbiota on in vivo metabolism and tissue accumulation of cytochrome P450 3A metabolized drug: Midazolam. *Biopharm. Drug Dispos.* **41**, 275 (2020).
7. Selwyn, F. P., Cheng, S. L., Klaassen, C. D. & Cui, J. Y. Regulation of Hepatic Drug-Metabolizing Enzymes in Germ-Free Mice by Conventionalization and Probiotics. *Drug Metab. Dispos.* **44**, (2016).
8. Kuno, T., Hirayama-Kurogi, M., Ito, S. & Ohtsuki, S. Effect of Intestinal Flora on Protein Expression of Drug-Metabolizing Enzymes and Transporters in the Liver and Kidney of Germ-Free and Antibiotics-Treated Mice. *Mol. Pharm.* **13**, (2016).
9. Zemanová, N. *et al.* Gut microbiome affects the metabolism of metronidazole in mice through regulation of hepatic cytochromes P450 expression. *PLoS One* **16**, e0259643 (2021).

10. Björkholm, B. *et al.* Intestinal Microbiota Regulate Xenobiotic Metabolism in the Liver. *PLoS One* **4**, e6958 (2009).
11. Stephanie L. Collins, A. D. P. The gut microbiome: an orchestrator of xenobiotic metabolism. *Yao Xue Xue Bao* **10**, 19 (2020).
12. Makałowski, W., Zhang, J. & Boguski, M. S. Comparative analysis of 1196 orthologous mouse and human full-length mRNA and protein sequences. *Genome Res.* **6**, (1996).
13. Hugenholtz, F. & de Vos, W. M. Mouse models for human intestinal microbiota research: a critical evaluation. *Cell. Mol. Life Sci.* **75**, 149–160 (2017).
14. Zimmermann, M., Zimmermann-Kogadeeva, M., Wegmann, R. & Goodman, A. L. Separating host and microbiome contributions to drug pharmacokinetics and toxicity. *Science* **363**, (2019).
15. Malfatti, M. A. *et al.* Manipulation of the Gut Microbiome Alters Acetaminophen Biodisposition in Mice. *Sci. Rep.* **10**, 4571 (2020).
16. Benet, L. Z. & Zia-Amirhosseini, P. Basic principles of pharmacokinetics. *Toxicol. Pathol.* **23**, (1995).
17. Sinha, V. K. *et al.* Predicting Oral Clearance in Humans. *Clinical Pharmacokinetics* vol. 47 35–45 Preprint at https://doi.org/10.2165/00003088-200847010-00004 (2008).
18. Beaumont, M. *et al.* Quantity and source of dietary protein influence metabolite production by gut microbiota and rectal mucosa gene expression: a randomized, parallel, double-blind trial in overweight humans. *Am. J. Clin. Nutr.* **106**, 1005–1019 (2017).
19. Bishop, B. *et al.* A prospective study of the incidence of drug-induced liver injury by the modern volatile anaesthetics sevoflurane and desflurane. *Aliment. Pharmacol. Ther.* **49**, 940–951 (2019).
20. Johnson, E. L. *et al.* Sphingolipids produced by gut bacteria enter host metabolic pathways impacting ceramide levels. *Nat. Commun.* **11**, 1–11 (2020).
21. An, D. *et al.* Sphingolipids from a symbiotic microbe regulate homeostasis of host intestinal

natural killer T cells. *Cell* **156**, 123–133 (2014).

22. Anthérieu, S., Chesné, C., Li, R., Guguen-Guillouzo, C. & Guillouzo, A. Optimization of the HepaRG cell model for drug metabolism and toxicity studies. *Toxicol. In Vitro* **26**, 1278–1285 (2012).
23. Aninat, C. *et al.* Expression of cytochromes P450, conjugating enzymes and nuclear receptors in human hepatoma HepaRG cells. *Drug Metab. Dispos.* **34**, 75–83 (2006).
24. Anthérieu, S. *et al.* Stable expression, activity, and inducibility of cytochromes P450 in differentiated HepaRG cells. *Drug Metab. Dispos.* **38**, 516–525 (2010).
25. O'Brien, J., Wilson, I., Orton, T. & Pognan, F. Investigation of the Alamar Blue (resazurin) fluorescent dye for the assessment of mammalian cell cytotoxicity. *Eur. J. Biochem.* **267**, 5421–5426 (2000).
26. Ritz, C., Baty, F., Streibig, J. C. & Gerhard, D. Dose-Response Analysis Using R. *PLoS One* **10**, e0146021 (2015).
27. Bonn, B., Svanberg, P., Janefeldt, A., Hultman, I. & Grime, K. Determination of Human Hepatocyte Intrinsic Clearance for Slowly Metabolized Compounds: Comparison of a Primary Hepatocyte/Stromal Cell Co-culture with Plated Primary Hepatocytes and HepaRG. *Drug Metab. Dispos.* **44**, 527–533 (2016).
28. Maria Bodero, J. F. A. Microsome Isolation from Tissue. *Bio-protocol* **4**, (2014).
29. Stresser, D. M. *et al.* Substrate-dependent modulation of CYP3A4 catalytic activity: analysis of 27 test compounds with four fluorometric substrates. *Drug Metab. Dispos.* **28**, 1440–1448 (2000).
30. Li, D. *et al.* Effect of Regular Organic Solvents on Cytochrome P450-Mediated Metabolic Activities in Rat Liver Microsomes. *Drug Metab. Dispos.* **38**, 1922–1925 (2010).
31. Focke, W. W., van der Westhuizen, I., Musee, Ndeke & Loots, M. T. Kinetic interpretation of log-logistic dose-time response curves. *Sci. Rep.* **7**, 1–11 (2017).
32. Strelow, J. *et al.* Mechanism of Action Assays for Enzymes. in *Assay Guidance Manual*

[Internet] (Eli Lilly & Company and the National Center for Advancing Translational Sciences, 2012).

33. Center for Drug Evaluation & Research. Table of Substrates, Inhibitors and Inducers. https://www.fda.gov/drugs/drug-interactions-labeling/drug-development-and-drug-interactions-table-substrates-inhibitors-and-inducers (2021).
34. Chen, S., Zhou, Y., Chen, Y. & Gu, J. fastp: an ultra-fast all-in-one FASTQ preprocessor. *Bioinformatics* **34**, i884–i890 (2018).
35. GENCODE - Mouse Release M28. https://www.gencodegenes.org/mouse/.
36. Liao, Y., Smyth, G. K. & Shi, W. featureCounts: an efficient general purpose program for assigning sequence reads to genomic features. *Bioinformatics* **30**, 923–930 (2013).
37. Love, M. I., Huber, W. & Anders, S. Moderated estimation of fold change and dispersion for RNA-seq data with DESeq2. *Genome Biology* vol. 15 Preprint at https://doi.org/10.1186/s13059-014-0550-8 (2014).
38. Ulgen, E., Ozisik, O. & Sezerman, O. U. pathfindR: An R Package for Comprehensive Identification of Enriched Pathways in Omics Data Through Active Subnetworks. *Front. Genet.* **0**, (2019).
39. Julia Yue Cui, C. D. K. RNA-Seq Reveals Common and Unique PXR- and CAR-target Gene Signatures in the Mouse Liver Transcriptome. *Biochim. Biophys. Acta* **1859**, 1198 (2016).
40. Caporaso, J. G. *et al.* Ultra-high-throughput microbial community analysis on the Illumina HiSeq and MiSeq platforms. *ISME J.* **6**, 1621–1624 (2012).
41. Gohl, D. M. *et al.* Systematic improvement of amplicon marker gene methods for increased accuracy in microbiome studies. *Nat. Biotechnol.* **34**, 942–949 (2016).
42. Callahan, B. J. *et al.* DADA2: High-resolution sample inference from Illumina amplicon data. *Nat. Methods* **13**, 581–583 (2016).
43. Wang, Q., Garrity, G. M., Tiedje, J. M. & Cole, J. R. Naive Bayesian classifier for rapid assignment of rRNA sequences into the new bacterial taxonomy. *Appl. Environ. Microbiol.*

73, 5261–5267 (2007).

44. Price, M. N., Dehal, P. S. & Arkin, A. P. FastTree 2 – Approximately Maximum-Likelihood Trees for Large Alignments. *PLoS One* **5**, e9490 (2010).
45. Silverman, J. D., Washburne, A. D., Mukherjee, S. & David, L. A. A phylogenetic transform enhances analysis of compositional microbiota data. (2017) doi:10.7554/eLife.21887.
46. Paradis, E., Claude, J. & Strimmer, K. APE: Analyses of Phylogenetics and Evolution in R language. *Bioinformatics* **20**, 289–290 (2004).
47. Dixon, P. VEGAN, a package of R functions for community ecology. *J. Veg. Sci.* **14**, 927–930 (2003).
48. Kuznetsova, A., Brockhoff, P. B. & Christensen, R. H. B. lmerTest Package: Tests in Linear Mixed Effects Models. *Journal of Statistical Software* vol. 82 Preprint at https://doi.org/10.18637/jss.v082.i13 (2017).
49. Westfall, P. H. & Stanley Young, S. *Resampling-Based Multiple Testing: Examples and Methods for p-Value Adjustment*. (John Wiley & Sons, 1993).
50. Package Recipe “bmtagger” — Bioconda documentation. https://bioconda.github.io/recipes/bmtagger/README.html.
51. Beghini, F. *et al.* Integrating taxonomic, functional, and strain-level profiling of diverse microbial communities with bioBakery 3. *Elife* **10**, (2021).
52. Yoav E. Timsit, M. N. CAR and PXR: The Xenobiotic-Sensing Receptors. *Steroids* **72**, 231 (2007).
53. Cyp3a11 MGI Mouse Gene Detail - MGI:88609 - cytochrome P450, family 3, subfamily a, polypeptide 11. http://www.informatics.jax.org/marker/MGI:88609.
54. Buyssens, L. *et al.* Hepatic Cytochrome P450 Abundance and Activity in the Developing and Adult Göttingen Minipig: Pivotal Data for PBPK Modeling. *Front. Pharmacol.* **0**, (2021).
55. Benet, L. Z., Broccatelli, F. & Oprea, T. I. BDDCS Applied to Over 900 Drugs. *AAPS J.* **13**, 519 (2011).

56. Screening in a spirit haunted world. *Drug Discov. Today* **11**, 607–615 (2006).

57. Auld, D. S., Inglese, J. & Dahlin, J. L. Assay Interference by Aggregation. in *Assay Guidance Manual [Internet]* (Eli Lilly & Company and the National Center for Advancing Translational Sciences, 2017).

58. Heuman, D. M., Pandak, W. M., Hylemon, P. B. & Vlahcevic, Z. R. Conjugates of ursodeoxycholate protect against cytotoxicity of more hydrophobic bile salts: in vitro studies in rat hepatocytes and human erythrocytes. *Hepatology* **14**, 920–926 (1991).

59. A dose-dependent effect of dimethyl sulfoxide on lipid content, cell viability and oxidative stress in 3T3-L1 adipocytes. *Toxicology Reports* **5**, 1014–1020 (2018).

60. Kumar, P., Nagarajan, A. & Uchil, P. D. Analysis of Cell Viability by the Lactate Dehydrogenase Assay. *Cold Spring Harb. Protoc.* **2018**, (2018).

61. Rampersad, S. N. Multiple Applications of Alamar Blue as an Indicator of Metabolic Function and Cellular Health in Cell Viability Bioassays. *Sensors* **12**, 12347 (2012).

62. Babson, A. L. & Phillips, G. E. A rapid colorimetric assay for serum lactic dehydrogenase. *Clin. Chim. Acta* **12**, 210–215 (1965).

63. Iatsenko, I., Boquete, J.-P. & Lemaitre, B. Microbiota-Derived Lactate Activates Production of Reactive Oxygen Species by the Intestinal NADPH Oxidase Nox and Shortens Drosophila Lifespan. *Immunity* **49**, 929-942.e5 (2018).

64. van Meerloo, J., Kaspers, G. J. L. & Cloos, J. Cell Sensitivity Assays: The MTT Assay. *Methods in Molecular Biology* 237–245 Preprint at https://doi.org/10.1007/978-1-61779-080-5_20 (2011).

65. Hamilton, G. A. *et al.* Regulation of cell morphology and cytochrome P450 expression in human hepatocytes by extracellular matrix and cell-cell interactions. *Cell Tissue Res.* **306**, 85–99 (2001).

66. Membrane-attached mammalian cytochromes P450: An overview of the membrane's effects on structure, drug binding, and interactions with redox partners. *J. Inorg. Biochem.* **183**, 117–

136 (2018).

67. Burnham, K. P., Anderson, D. R. & Huyvaert, K. P. AIC model selection and multimodel inference in behavioral ecology: some background, observations, and comparisons. *Behavioral Ecology and Sociobiology* vol. 65 23–35 Preprint at https://doi.org/10.1007/s00265-010-1029-6 (2011).
68. Sphingolipids in host–microbial interactions. *Curr. Opin. Microbiol.* **43**, 92–99 (2018).
69. Clarke, N. G. & Dawson, R. M. C. Alkaline O→N-transacylation. A new method for the quantitative deacylation of phospholipids. *Biochemical Journal* vol. 195 301–306 Preprint at https://doi.org/10.1042/bj1950301 (1981).
70. Owen, S. C. *et al.* Colloidal Drug Formulations Can Explain “Bell-Shaped” Concentration–Response Curves. *ACS Chemical Biology* vol. 9 777–784 Preprint at https://doi.org/10.1021/cb4007584 (2014).
71. Thummel, K. E. *et al.* Use of midazolam as a human cytochrome P450 3A probe: I. In vitro-in vivo correlations in liver transplant patients. *J. Pharmacol. Exp. Ther.* **271**, (1994).
72. Michaelis, L., Menten, M. L., Johnson, K. A. & Goody, R. S. The original Michaelis constant: translation of the 1913 Michaelis-Menten paper. *Biochemistry* **50**, 8264–8269 (2011).
73. McClary, W. D., Sumida, J. P., Scian, M., Paço, L. & Atkins, W. M. Membrane Fluidity Modulates Thermal Stability and Ligand Binding of Cytochrome P4503A4 in Lipid Nanodiscs. *Biochemistry* **55**, 6258 (2016).
74. Bieberich, E. Sphingolipids and lipid rafts: Novel concepts and methods of analysis. *Chem. Phys. Lipids* **216**, 114 (2018).
75. Devi, B. G., Gupta, P. D. & Habeebullah, C. M. Changes in membrane fluidity during human liver development. *Biochem. Int.* **28**, 41–49 (1992).
76. Noutsi, P., Gratton, E. & Chaieb, S. Assessment of Membrane Fluidity Fluctuations during Cellular Development Reveals Time and Cell Type Specificity. *PLoS One* **11**, e0158313 (2016).

77. Hijazi, Y. & Boulieu, R. Contribution of CYP3A4, CYP2B6, and CYP2C9 isoforms to N-demethylation of ketamine in human liver microsomes. *Drug Metab. Dispos.* **30**, (2002).

78. Lavoie, D. S.-G., Pailleux, F., Vachon, P. & Beaudry, F. Characterization of xylazine metabolism in rat liver microsomes using liquid chromatography-hybrid triple quadrupole-linear ion trap-mass spectrometry. *Biomed. Chromatogr.* **27**, 882–888 (2013).

79. Chun, Y.-J., Lee, S., Yang, S. A., Park, S. & Kim, M. Y. Modulation of CYP3A4 expression by ceramide in human colon carcinoma HT-29 cells. *Biochem. Biophys. Res. Commun.* **298**, 687–692 (2002).

80. Turner, P. V., Brabb, T., Pekow, C. & Vasbinder, M. A. Administration of Substances to Laboratory Animals: Routes of Administration and Factors to Consider. *J. Am. Assoc. Lab. Anim. Sci.* **50**, 600 (2011).

81. Casares, D., Escribá, P. V. & Rosselló, C. A. Membrane Lipid Composition: Effect on Membrane and Organelle Structure, Function and Compartmentalization and Therapeutic Avenues. *Int. J. Mol. Sci.* **20**, (2019).

82. Eich, C. *et al.* Changes in membrane sphingolipid composition modulate dynamics and adhesion of integrin nanoclusters. *Sci. Rep.* **6**, 1–15 (2016).

83. Lipid Rafts: Elusive or Illusive? *Cell* **115**, 377–388 (2003).

84. Alberts, B. *Molecular Biology of the Cell*. (2004).

85. Ye, M. *et al.* Size- and time-dependent alteration in metabolic activities of human hepatic cytochrome P450 isozymes by gold nanoparticles via microsomal coincubations. *Nanoscale Res. Lett.* **9**, 642 (2014).

86. Lay, C. *et al.* Design and validation of 16S rRNA probes to enumerate members of the Clostridium leptum subgroup in human faecal microbiota. *Environ. Microbiol.* **7**, 933–946 (2005).

87. Smits, S. A. *et al.* Seasonal cycling in the gut microbiome of the Hadza hunter-gatherers of Tanzania. *Science* **357**, 802–806 (2017).

88. Taichi A. Suzuki, M. W. Geographical variation of human gut microbial composition. *Biol. Lett.* **10**, (2014).

89. Xu, J. *et al.* Evolution of Symbiotic Bacteria in the Distal Human Intestine. *PLoS Biol.* **5**, (2007).

90. Mariat, D. *et al.* The Firmicutes/Bacteroidetes ratio of the human microbiota changes with age. *BMC Microbiol.* **9**, 1–6 (2009).

91. Gupta, V. K., Paul, S. & Dutta, C. Geography, Ethnicity or Subsistence-Specific Variations in Human Microbiome Composition and Diversity. *Front. Microbiol.* **0**, (2017).

92. Thomas, F., Hehemann, J.-H., Rebuffet, E., Czjzek, M. & Michel, G. Environmental and Gut Bacteroidetes: The Food Connection. *Front. Microbiol.* **0**, (2011).

93. Comparative binding of bile acids to serum lipoproteins and albumin. *J. Lipid Res.* **34**, 1661–1674 (1993).

94. Perwaiz, S., Mignault, D., Tuchweber, B. & Yousef, I. M. Rapid and improved method for the determination of bile acids in human feces using MS. *Lipids* **37**, 1093–1100 (2002).

Supplementary materials

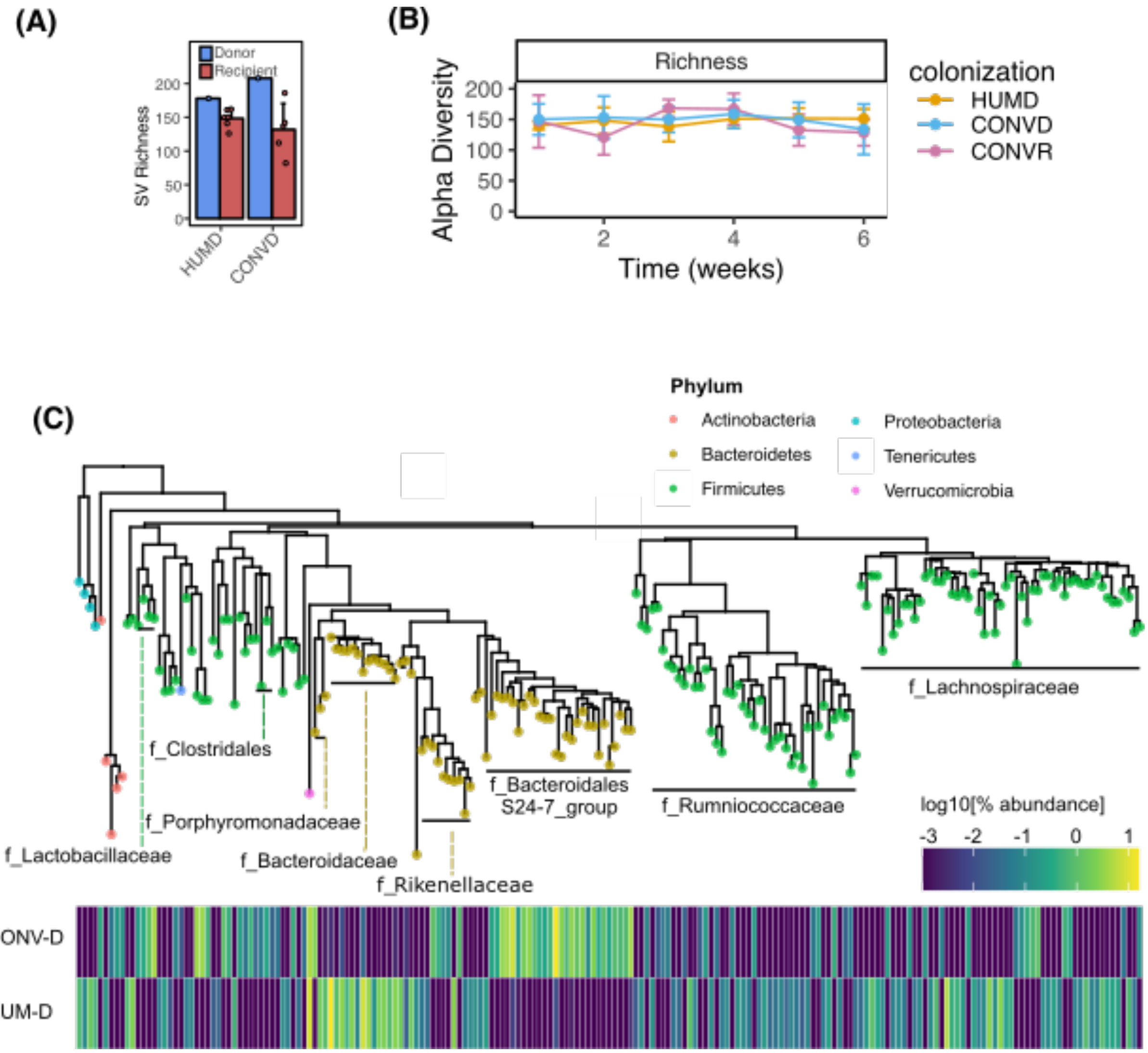

SFigure 3.1 16S characterization of complex microbiomes reveals stable engraftment and differences between microbiomes

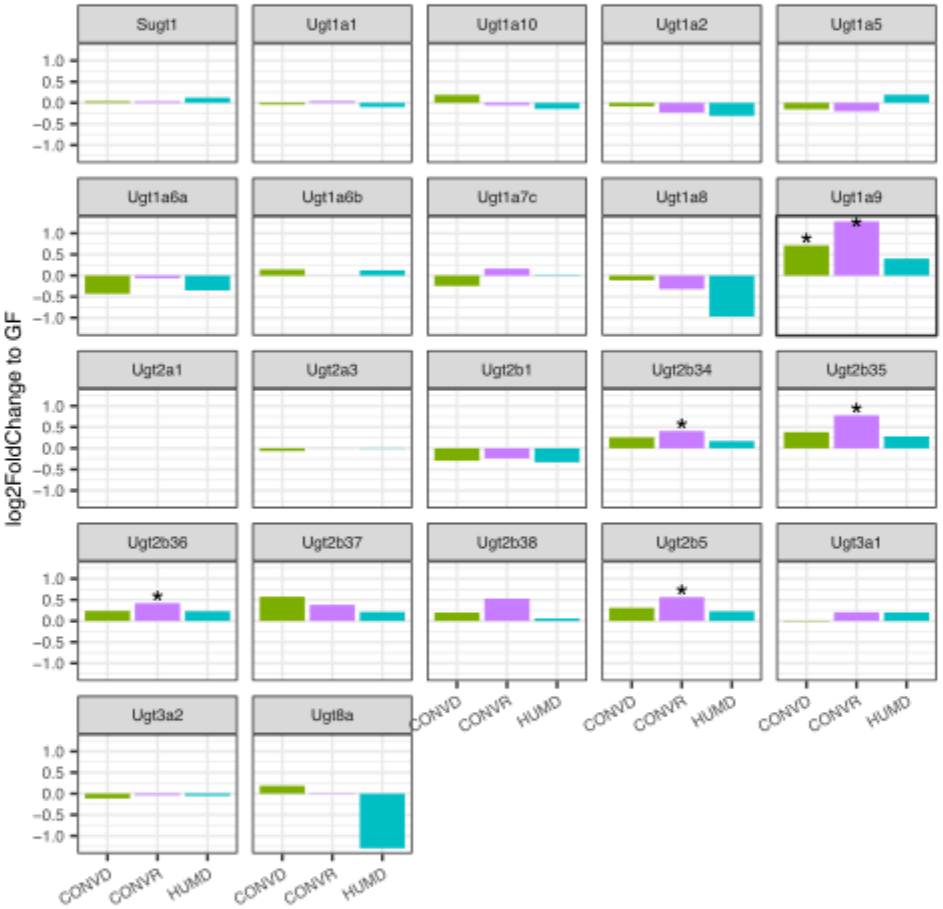

SFigure 3.2 Ugt expression in colonized mice did not decrease significantly compared to GF mice (criteria for significance was pval <0.1, absolute log2 Fold Change >1, DESeq2).

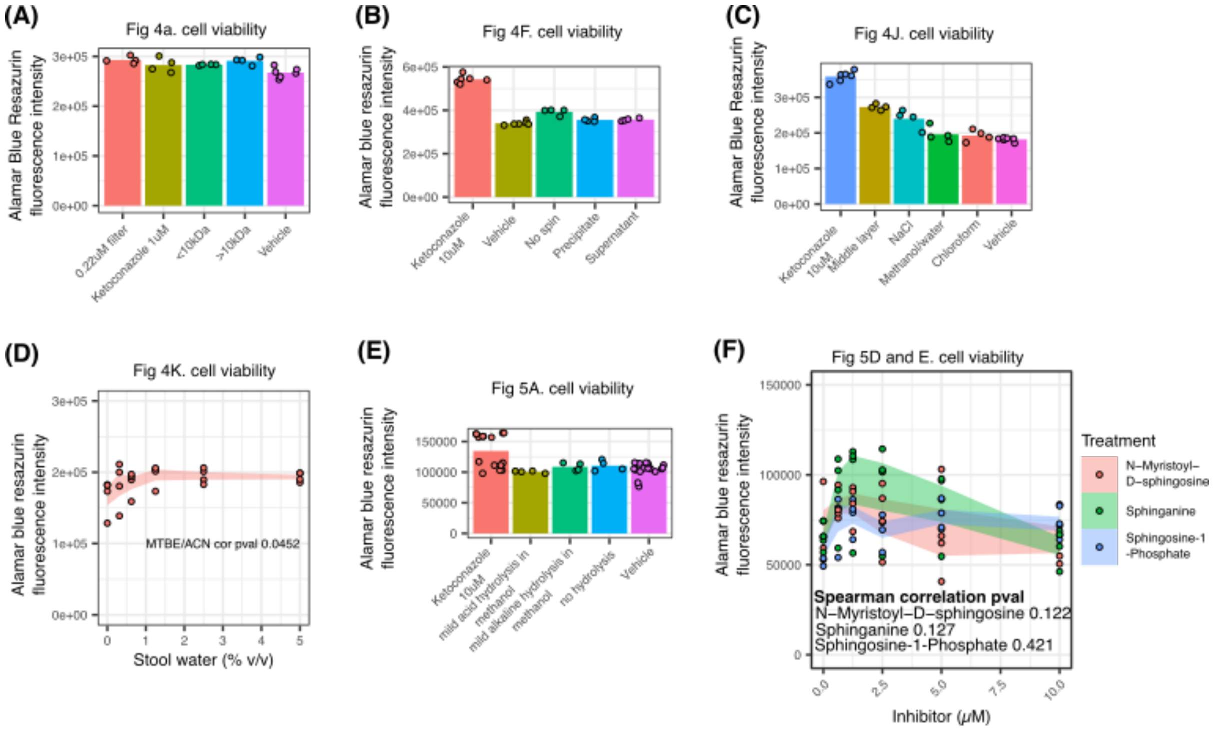

SFigure 3.3 Cell viability data from alamar blue cell viability assay. Each corresponding subpanel is labeled with its corresponding activity subpanel data.

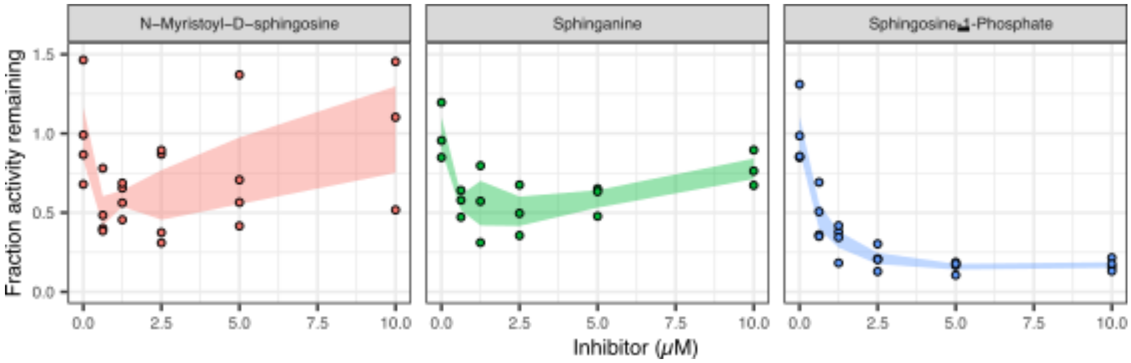

SFigure 3.4 Dose response curves of 3 selected sphingolipids.

N-Myristoyl-D-Sphingosine and Sphinganine exhibit bell-shaped dose responses, a phenomenon which reflects the concentration of bioactive, monomeric compound [70].

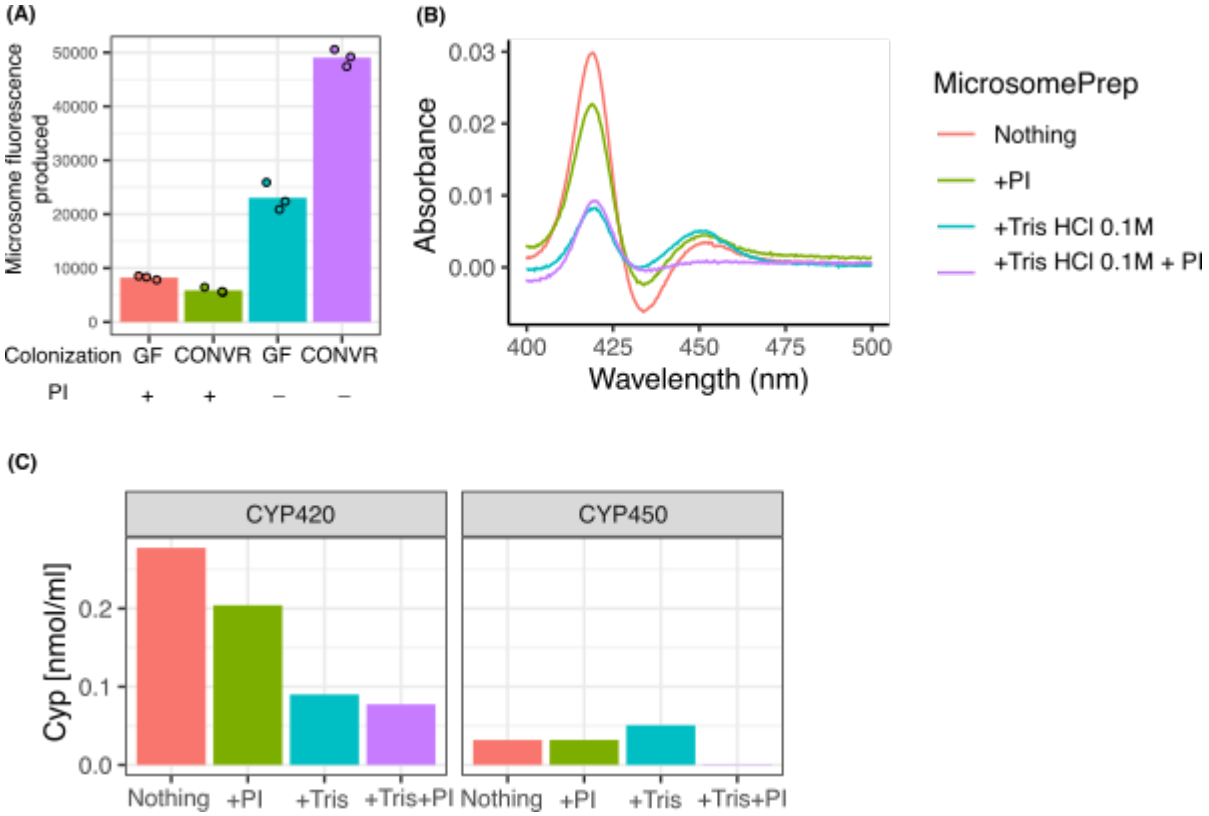

SFigure 3.5 The level of Cyp activity between GF and CONVR mice can be altered based on the preparation method.

While all preparation methods led to intact Cyps with P450 spectrums, their activity varied greatly suggesting other structural components such as membrane fluidity could be involved.

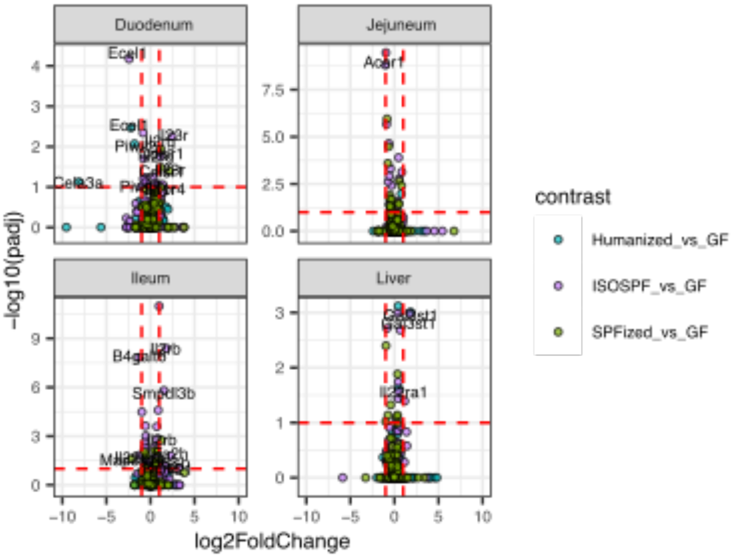

SFigure 3.6 Few sphingolipid genes were significantly changed between complex colonizations and GF mice.

Gene list was as referenced from Johnson et al.

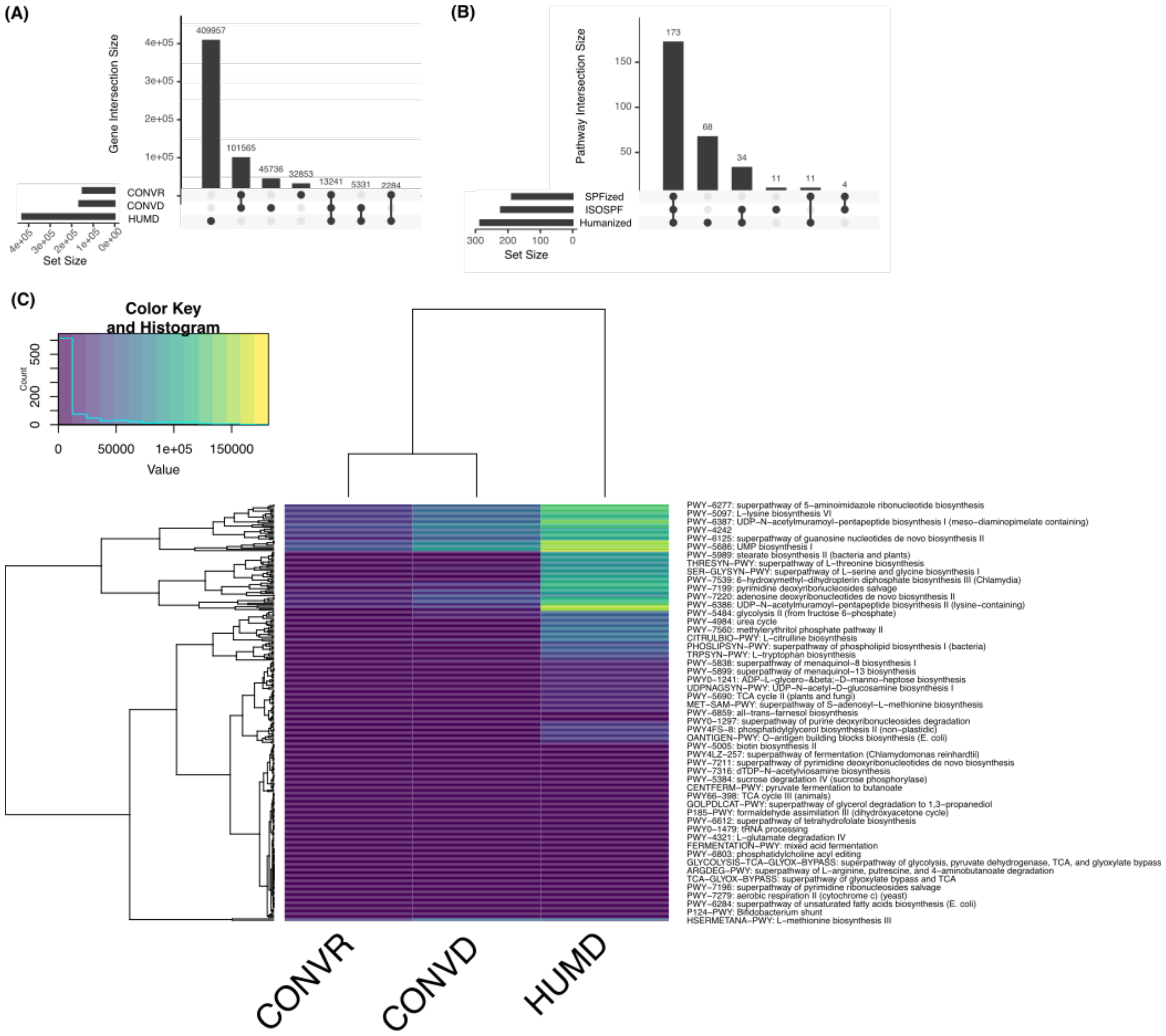

SFigure 3.7 Upset plot of metagenomic genes and pathways across colonization groups shows HUMD had the most characterized genes.

(A) Upset plot of all genes present in each complex gut microbial colonization shows HUMD had 4 times more genes characterized compared to both CONVR and CONVD. (B) Upset plot of all pathways enriched in each complex gut microbial colonization shows the majority of the pathways overlap across the colonization groups. (C) Common pathways in all complex colonizations did not include sphingolipid pathways, of which the key gene serine palmitoyltransferase was not identified in any sample, and no sphingolipid pathways were enriched in any sample.

Contributions

Professor Peter J. Turnbaugh supervised the entirety of this work. Dr. Peter Spangianipulous and Dr. Jordan Bisanz spearheaded the initial colonization experiments, 16S, and metagenomic sequencing in Fig 1. Dr. Cecilia Noecker and Dr. Benjamin Guthrie provided feedback on the experimental designs and analyses. LC/MS/MS methods were designed in collaboration with Dr. Moriah Sandy from UCSF QMAC. Mouse experiments were done with assistance from Dr. Jessie Turnbaugh, Kimberly Ly, and Jolie Ma from the UCSF Gnotobiotic core.

We would also like to thank Dr. Elizabeth L. Johnson for insights on sphingolipid characterization, Dr. Brian K. Shoichet and Dr. Molly S. Shoichet for tips on small molecule colloidal aggregation, the Shoichet lab for assistance with dynamic light scattering, and Dr. Eric CY Chan for feedback on the mechanism of inhibition assays.

Last but not least, thank you to my thesis committee, Prof Deanna Kroetz, Prof Leslie Benet, and Prof Katie Pollard for all the feedback and support for this project.

Final discussion

The work presented in this part 1 of this dissertation explores the curious trend of how we can utilize our understanding of pharmacokinetics and pharmacodynamics to help optimize dose and rank drug regimens against pathogenic microbe Mtb for testing in resource-intensive clinical trials. In part 2, we flip the narrative and explore how non pathogenic microbes that live as gut commensals can in turn shape host drug disposition too, possibly via sphingolipid production that can influence CYP3A4 enzyme activity. Both parts demonstrate how a good knowledge of PKPD is useful for both as a tool for knowledge integration to accelerate drug discovery, as well as a framework for asking mechanistic questions like how the gut microbiome can affect drug metabolism in the host.

Part 1 demonstrated the utility of using preclinical mouse studies (Chapter 1) to predict clinical short-term monotherapy outcomes, as well as long-term drug combination outcomes. Traditional drug development has been empiric and fraught with trial and error despite how resource and time-intensive it is. PK-PD models allow us to be able to better use preclinical in vivo data from mice to predict clinical outcomes such as short term monotherapy. The success in translatable clinical predictions from preclinical mouse studies was due mainly to being able to characterize the immune response in mice using a bacterial dynamics model allowing us to get the true exposure-response relationship in mice, making it translatable between mouse and human.

Chapter 2 further emphasizes the translatability of the system by demonstrating that in vitro exposure-response relationships can also be used to predict both preclinical mouse and clinical EBA in Phase IIa trials. Depending on the size of the initial infection, as well as how long the infected mouse was incubated for prior to treatment, the type of in vitro assay can vary. However, for all infection models, the use of RAW264.7 mouse macrophage cell line, as well as growth of Mtb in an acidic media were good predictors of in vivo exposure response. Across all 3 infection model types we tested, the top combinations consisting of 3 in vitro assays generally differed by 1 assay. The predicted exposure-response from the selected 3 in vitro assays can then be used to predict mouse CFU burden over time with drug treatment over a range of different drug doses.

However a drawback of in vitro assays was that we have yet to find a good in vitro predictor for pharmacodynamic drug-drug interactions that would be translatable to in vivo outcomes as drug combinations. Further work would need to be done to identify a framework for rational drug combination design and ranking based on in vitro assay data.

These preclinical tools to predict clinical outcomes will greatly help us to prioritize and better design clinical trials and accelerate drug development, a urgent and unmet need in the field of tuberculosis.

In part 2 we then explored how nonpathogenic microbes such as commensal gut microbes could impact host drug disposition (Chapter 4). We first observed that despite a higher expression of Cyp3a11 in CONVR mice compared to GF mice, the elimination of midazolam was higher in GF compared to CONVR mice, suggesting an inhibitor was also being produced by the microbiome. Afterward, we also characterized Cyp3a11 kinetics using mouse microsomes derived from CONVR and GF mice and found that GF mice had a higher Vmax compared to CONVR mice, further suggesting that a possible structural change in the enzyme was present. Biochemical analysis and further cell based HepaRG assays showed that sphingolipids were possibly modulating Cyp3a11 activity in mice. We thus concluded that the microbiome could be modulating the effect of Cyp3a11 in mice via sphingolipid production.

This potential mechanism of microbiome modulating Cyp3a11 activity would not have been elucidated without the necessary knowledge in pharmacology, as well as drug metabolism and pharmacokinetics (DMPK). For example, in order to prevent confounding variables in absorption and first pass metabolism, all mouse PK experiments were done IV to measure the rate of elimination. Using microsome assays to characterize the kinetics of Cyp3a11 also allowed us to characterize the effect of gut microbial colonization on the structure, as well as the nature of the microbial Cyp3a11 inhibitor.

This work thus demonstrates how PK-PD concepts are useful in both helping to accelerate drug development through making translational tools to predict clinical outcomes, as well as developing rigorous methods to better investigate phenomena in basic science.

Publishing Agreement

It is the policy of the University to encourage open access and broad distribution of all theses, dissertations, and manuscripts. The Graduate Division will facilitate the distribution of UCSF theses, dissertations, and manuscripts to the UCSF Library for open access and distribution. UCSF will make such theses, dissertations, and manuscripts accessible to the public and will take reasonable steps to preserve these works in perpetuity.

I hereby grant the non-exclusive, perpetual right to The Regents of the University of California to reproduce, publicly display, distribute, preserve, and publish copies of my thesis, dissertation, or manuscript in any form or media, now existing or later derived, including access online for teaching, research, and public service purposes.

DocuSigned by:
Janice Goh
9E6596E75A7E43E...
Author Signature

5/23/2023
Date